ION-BEAM MIXING
AND
THE FORMATION OF AMORPHOUS ALLOYS

Thesis by

Yang-Tse Cheng

In Partial Fulfillment of the Requirements
for the Degree of
Doctor of Philosophy

California Institute of Technology
Pasadena, California

1987

(Submitted October 28, 1986)

To my parents

ACKNOWLEDGEMENTS

First and foremost, I wish to thank Professor William L. Johnson and Professor Marc-A. Nicolet. Their support, encouragement, inspiration, and guidance have made my graduate study at Caltech a very rewarding experience.

I would like to thank Drs. M. Van Rossum and B. X. Liu, who provided much guidance when I had just begun my research in ion-solid interactions. I would also like to thank members of Professor Johnson's and Professor Nicolet's group, especially to T. Workman, Z.-A. Zhao, Dr. T. Banwell, Dr. K. Affolter, Dr. H. Ibe, W. J. Meng, S. M. Anlage, Dr. X. L. Yeh, Dr. E. J. Cotts, Dr. K. Unruh, F. So, and S.-J. Kim, who have contributed, through either collaborations or casual conversations, to the completion of this thesis.

Particular acknowledgements are due to Dr. R. Johnson, P. Askenazy, A. Mutz, Dr. D. Jamieson, and N. Baird, who carefully read the manuscript and provided valuable suggestions.

I am specially indebted to D. Groseth, A. Ghaffari, R. Gorris, and C. Geremia for their technical assistance, to A. Collinwood, J. Ferrante, M. Parks, and A. Bressan for their friendship and valuable assistance.

Financial support for this work has been provided by the Department of Energy, project agreement No. DE-AT03-81ER10870 under contract DE-AM03-76F00767, the Office of Naval Research under contract No. N00014-84-K-0275, the National Science Foundation grant No. DMR-8421119, and the Department of Energy under contract No. DE-AA03-76SF00767.

PREFACE

Ion beam interactions with solids have been of significant interest to both academic and industrial researchers for more than half a century. Looking back into the history of its development, one finds prominent names such as Bohr, Fermi, and Bethe, closely associated with the early development of this area of scientific research. Their efforts in understanding the interatomic potential of ions and atoms have led to the knowledge of ion penetration depth and energy loss in solids. It was also one of the early successful applications of the newly born quantum mechanics.

The subsequent development of the range theory by Lindhard, Scharff, and Schioff in the early sixties (LSS theory) enables one to calculate the ion penetration depth in elemental solids to even greater accuracy and provides the basis for the realization of ion implantation technology.

Swelling of reactor materials, caused by ion irradiation, was first observed in austenitic steel in 1967 by a group of British scientists. Such radiation damage drew unprecedented attention of people from both academia and industry to the problem of ion-solid interactions. Irradiation-induced structural and phase changes in materials have since become a major part of the active research in ion beam interactions with solids.

Ion implantation, which originated in the early 1960s, revolutionized the microelectronics industry. Because of the development of the range theory, ion implantation offered precise control over the number and depth of dopant atoms in semiconductor materials, making possible the miniaturization of electronic devices. Meanwhile, various ion beam analysis techniques, such as RBS (Rutherford Backscattering Spectrometry), developed rapidly and were applied to study problems ranging from Moon rocks to electronic devices.

Around 1972, while studying ion implantation in Si through an Al overlayer, D. H. Lee, O. J. Marsh, and R. R. Hart of the Hughes Research Laboratories observed coloration of the surface layer. Using RBS and optical reflectance measurements, they determined that the coloration was due to the migration of Si to the surface of the sample under the influence of ion bombardment. In another case, they observed Pt_2Si formation due to mixing of the Si and the Pt overlayer caused by ion implantation. Soon it was found that metastable phases as well as equilibrium phases could be obtained by this type of ion beam-induced mixing phenomena, more commonly called ion mixing processes.

Today, ion implantation has found further applications in areas such as corrosion resistance, reduction of wear and friction, and improvement of adhesion. Ion mixing has been viewed as a powerful extension of the traditional ion implantation technology. It provides new challenges to fundamental research in ion-solid interactions and offers new promises to further industrial applications.

Two issues are considered of fundamental importance and are treated in this thesis.

I. Mechanisms of ion-beam-induced mixing in solids.

II. The formation of amorphous alloys.

In Part I, several aspects of the mixing mechanisms, such as the influence of chemical driving force, the influence of cohesive energy, a newly developed phenomenological model of ion mixing, and a correlation between the cohesive energy

and the onset of radiation-enhanced diffusion will be discussed. Also in this part, the evolution of collisional cascades will be studied by using a fractal geometry approach. In Part II, mechanisms of amorphous alloy formation are discussed. Comparisons between amorphous alloy formation by ion mixing and by solid-state reaction illustrate various aspects of glass formation.

CONTENTS

PART I. ION-BEAM MIXING

PART II. THE FORMATION OF AMORPHOUS ALLOYS

LIST OF TABLES

LIST OF FIGURES

PART I. ION-BEAM MIXING

Chapter 1

INTRODUCTION TO ION-SOLID INTERACTIONS

The slowing down of an energetic ion in a solid and the evolution of its disturbances are transient processes. Relevant physical parameters such as the kinetic and potential energies of a particle are all time-dependent. In order to provide a frame of reference, the various mechanisms can be divided into two regimes.[1] The *prompt regime*, lasting about 10^{-11} seconds, refers to the time period from initial ion impact up to the time required to establish a uniform ambient temperature throughout the solid. Subsequent processes at the ambient temperature, such as the thermally activated motion of defects generated during the prompt regime, may occur in the *delayed regime.*

1.1 Prompt Regime – Recoil and Cascade Mixing

During the prompt regime, two limiting kinds of events contribute to the mixing.[2] As the energetic ion penetrates a solid, it transfers part of its kinetic energy by colliding with target atoms (primary collisions). These atoms recoil and collide with other atoms (secondary collisions), giving rise to higher generations of collisions. The later-generation collisions produce many low energy recoils, which induce small displacements in random directions. This process is often called *cascade mixing.* A small fraction of the atoms are mixed by high energy anisotropic events; these produce large displacements in the forward direction of the primary collision, giving rise to recoil implantation. The resulting atomic relocation is therefore called *recoil mixing.*

A simple order of magnitude calculation for the probability of recoil mixing events shows[3] that its collisional cross section is less than $10^{-16}/\mathrm{cm}^2$, whereas the typical dose used in ion mixing experiments conducted for the present work is about 10^{15} to $10^{16}/\mathrm{cm}^2$. In comparison to cascade mixing, the amount of recoil mixing is only a negligible contribution to the overall mixing. Therefore, recoil mixing is not treated further in this thesis. Reviews of this subject can be found in the references.[1-5]

Several authors have previously given models for cascade mixing based on an integral equation formulation of the transport theory,[2,5,6] a phenomenological Brownian motion approach,[7,8] or a standard chemical reaction formulation.[9] The outcome of these various approaches can be described by the following formula[10]

$$\Omega^2 = \frac{1}{3}\Gamma_\circ \frac{\epsilon}{N}\xi_{21}\frac{R_c^2}{E_d}\phi, \tag{1.1}$$

where Ω is the spreading of a thin marker layer in marker experiments or the spreading of the interface in bilayer ion mixing experiments, $\Gamma_\circ$ a dimensionless parameter with value of about 0.6, ϵ the energy deposited per unit length due to nuclear collisions, N the atomic density , and $\xi_{21} = [4m_1m_2/(m_1+m_2)^2]^{1/2}$, where m_1 and m_2 are the masses of the particles involved in collisions. E_d is a threshold displacement energy, R_c^2 the mean-square range associated with E_d, and ϕ the ion dose (ions-per-unit area). The random walk nature of cascade mixing can be seen from the dependence $\Omega^2 \propto \phi$, and from knowing that $\phi \propto t$, the time.[1,7]

One of the major assumptions behind this formula is the binary collision approximation, in which only two-body collisions are considered. Furthermore, the physical parameters included, such as the atomic mass and density, are "ballistic" in nature. Thus, this type of model is frequently called the "ballistic" or the "linear cascade" model of ion mixing.

The linear dependence of Ω^2 on ϕ has been confirmed experimentally.[3,11] However, it has been demonstrated that Eq. (1.1) does not provide quantitative agreement with experiment; order of magnitude deviations have been reported prior to the present work.[10,12,13] No physical explanation was given for this unsatisfactory situation other than speculation concerning the possible existence of "chemical driving forces" in ion mixing.

The origin and mechanism of such chemical driving forces have been identified recently. A description of these results will form the subject of the next four chapters. In Chapter 2, the correlation between the heat of mixing of two solids and ion mixing efficiency in binary metallic systems is established. From this correlation, an effective temperature of ion mixing is estimated. This work leads naturally to the question of when thermodynamic ideas can be applied to describe ion mixing phenomena. In Chapter 3, the effect of the cohesive energy of the solids being mixed is discussed. We shall argue that a thermal-spike picture[14,15] is in better accord with experimental observation than binary collision models. These observations and ideas are blended together in Chapter 4, where a phenomenological model of ion mixing is proposed. In Chapter 5, this new model is further tested by comparison with additional experimental results. Extensions and limitations of this model are also discussed in Chapter 5. In Chapter 6, we attempt to address the question of how a cascade evolves, in particular, how it develops into a spike. A collisional cascade is simply modeled as a tree branching process and the idea of fractals[16] is implemented to study the proposed problem.

1.2 Delayed Regime – Radiation-Enhanced Diffusion

At the end of the prompt regime, there will generally be a nonequilibrium number of defects in the irradiation-influenced zone.[17] If the ambient temperature is sufficiently high, these defects can become mobile, causing more diffusion and mixing. In contrast to cascade mixing, which is independent of the ambient temperature, radiation-enhanced diffusion is temperature-dependent.[18-22] The enhanced-diffusion coefficient D^* for self-diffusion is given by

$$D^* = C_v D_v + C_i D_i, \tag{1.2}$$

where C_v and C_i are the concentrations of vacancies and interstitials, respectively; D_v and D_i are the corresponding diffusion constants. The concentrations C_v and C_i are calculated by solving a set of coupled differential equations, which include production and trapping terms of vacancies and interstitials. The enhanced-diffusion constant D^* has three regions of different temperature behavior.[18,19] First, at very high temperature, D^* becomes the normal thermal vacancy diffusion constant, and $D^* = C_v D_v$. Second, at intermediate temperature when the diffusion is enhanced and point defects annihilate mostly at fixed sinks, and one obtains

$$D^* = 2\alpha P l^2, \tag{1.3}$$

where P, derived from the Kinchin-Pease expression,[17] is the number of displacements per target atom per unit time, α is the fraction of point defects that escape the cascade to migrate freely through the lattice, and l is a characteristic diffusion length to fixed annihilation sites, which may be grain boundaries or dislocation loops. In this case, D^* is independent of temperature. Third, at somewhat lower temperatures where annihilation by recombination becomes important,

$$D^* = \left(\frac{\alpha P D_v}{\pi N R_{iv}}\right)^{1/2}, \tag{1.4}$$

where N is the atomic density of the material and R_{iv} is the maximum vacancy-interstitial separation at which spontaneous recombination occurs. The enhanced-diffusion constant now has an Arrhenius-type temperature dependence with an activation energy equal to one-half of the vacancy migration energy. At still lower temperatures, diffusions in the delayed regime becomes negligible, and one observes only the effects of cascade mixing in the prompt regime. It has been shown experimentally[23] that radiation-enhanced diffusion becomes the dominant mixing mechanism when the ambient temperature is above some critical value T_c (see Fig. 1.1). In Chapter 7, we shall demonstrate a correlation between T_c and the cohesive energy of the solid in question. This correlation enables one to predict the onset of radiation-enhanced diffusion for systems that have not yet been investigated. The theoretical bases for understanding this correlation and its implications are also discussed in Chapter 7.

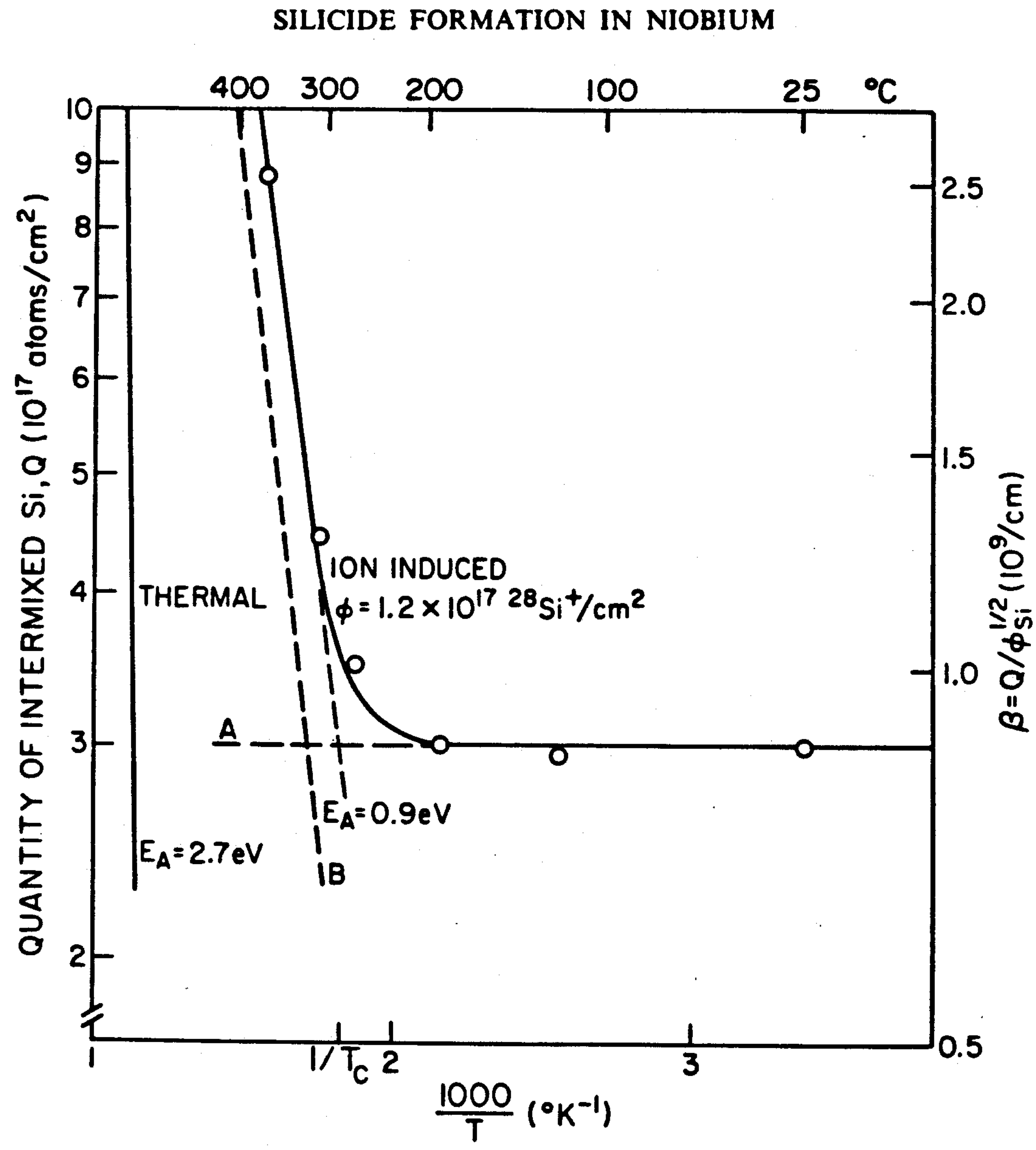

Fig. 1.1 Logarithm of the quantity of intermixed silicon versus reciprocal temperature for a dose of 1.2×10^{17} $^{28}Si^{+}/cm^{2}$ (Ref. 23).

1.3 References

1. S. Matteson and M-A. Nicolet, in *Metastable Materials Formation by Ion Implantation*, edited by S. T. Picraux and W. J. Choyke (North-Holland, Amsterdam, 1982), p. 3.
2. P. Sigmund and A. Gras-Marti, Nucl. Instrum. Methods **182/183**, 25 (1981).
3. B. M. Paine and R. S. Averback, Nucl. Instrum. Methods **B 7/8**, 666 (1985).
4. T. Banwell, Ph. D. Thesis, 1986 (Caltech).
5. U. Littmark and W. O. Hofer, Nucl. Instrum. Methods **168**, 329 (1980).
6. H. H. Anderson, Appl. Phys. **18**, 131 (1979).
7. P. K. Haff and Z. E. Switkowski, J. Appl. Phys. **48**, 3383 (1977).
8. S. Matteson, Appl. Phys. Lett. **39**, 288 (1981).
9. R. Collins and G. Carter, Rad. Effects **54**, 235 (1981).
10. F. Besenbacher, J. Bottiger, S. K. Nielsen, and H. J. Whitlow, Appl. Phys. **A 29**, 141 (1982).
11. J. W. Mayer, B. Y. Tsaur, S. S. Lau, and L-S. Hung, Nucl. Instrum. Methods **182/183**, 1 (1981).
12. T. Banwell, B. X. Liu, I. Golecki, and M-A. Nicolet, Nucl. Instrum. Methods **209/210**, 125 (1983).
13. Z. L. Wang, J. F. M. Westendorp, and F. W. Saris, Nucl. Instrum. Methods **209/210**, 115 (1983).
14. F. Seitz and J. S. Koehler, *Progress in Solid State Physics*, **2**, 305 (1956).
15. D. A. Thompson, Rad. Effects **56**, 105 (1981).
16. B. B. Mandelbrot, *The Fractal Geometry of Nature* (W. H. Freeman and Company, New York, 1983).
17. M. W. Thompson, *Defects and Radiation Damage in Metals* (Cambridge University Press, London, New York, 1969).
18. G. J. Dienes and A. C. Damask, J. Appl. Phys. **29**, 1713 (1958).

19. S. M. Myers, Nucl. Instrum. Methods **168**, 265 (1980).

20. J. C. Bourgoin and J. W. Corbett, Rad. Effects, **36**, 157 (1978).

21. R. A. Johnson, in *Materials Science Forum*, Vol. 1, edited by G. E. Murch (Trans Tech, Aedermannsdorf, 1984), p. 223.

22. N. Q. Lam and G. K. Leaf, J. Matt. Res. **1**, 251 (1986).

23. S. Matteson, J. Roth, and M-A. Nicolet, Rad. Effects, **42**, 217 (1979).

Chapter 2

INFLUENCE OF CHEMICAL DRIVING FORCES ON ION MIXING OF METALLIC BILAYERS

2.1 Introduction

As discussed in the last chapter, ion mixing phenomena have been traditionally described by ballistic models in which cascade mixing was supposed to arise from collisional processes only.[1–4] However, recent investigations have suggested that thermochemical effects are important in some cases. Large variations in mixing between systems that have similar collisional characteristics emphasize the need to take into account the chemical nature of the mixing species.[5–8]

In searching for the principal chemical driving force, we have been guided by our intuition in the following path. The main effect of energetic ion bombardment of a solid is to stir things up. While acid and water mix violently even without much disturbance, oil and water are almost impossible to mix by agitation. This is because the mixed state of acid and water, in contrast to oil and water, has a lower free energy than the unmixed state.[9,10] A similar situation can occur in alloying two metals; if mixing results in releasing energy, such systems are said to have a negative heat of mixing.[9,10] Other systems tend to separate due to a positive heat of mixing. In ion mixing, one would therefore expect that systems with a negative heat of mixing mix more efficiently than systems with positive heat of mixing. The heat of mixing parameters, ΔH_m, of binary alloys have been tabulated by Miedema and his co-workers[11,12] based on a phenomenological model of alloying developed by Miedema.[11] These parameters have been successfully used in the description of binary alloy formation.[11] Recently, the same parameters have been used to classify the possible location of heavy ions implanted in Be,[13] indicating that Miedema's approach may be relevant to ion implantation processes as well.

2.2 Ion Mixing of $5d - 3d$ Metallic Bilayers

The systems selected for our study consist of metallic bilayers of Pt or Au on top of a $3d$ metal (Ti, V, Cr, Mn, Co, Ni). Due to the similarity of their atomic numbers and masses of the top or bottom layers, these bilayers are expected to behave similarly according to the "ballistic" model of ion mixing (Eq. (1.1)), while covering a wide range of ΔH_m values.[11,12] Additionally, the large mass difference between the top layer and the bottom layer of each couple facilitates a study of the intermixing process by backscattering spectrometry.[14] The bilayer configuration is also better than that of markers for studying the chemical effect since it involves large concentrations of both elements. Effects of heat of mixing are small in dilute solutions, and they are far more important in concentrated alloys.

Thin bilayer films were prepared by electron-gun evaporation in an oil-free vacuum system at initial pressures below 10^{-7} Torr. All bilayers consisted of approximately 500 Å of Pt or Au on top of a 3000 Å thick $3d$-metal layer on a SiO_2 substrate. The top layer thickness was about the projected range of 600 keV Xe^{++} ions. Ion irradiation was performed at liquid nitrogen temperature (77 K) in order to reduce possible effects from radiation-enhanced diffusion; the vacuum during irradiation was maintained below 5×10^{-7} Torr. Irradiation doses were 10^{15}, 3×10^{15}, and 5×10^{15} Xe^{++} ion/cm^2 at a flux of about 200 nA/cm^2. Different samples were irradiated simultaneously to a specific dose in order to limit possible dose and dose rate variations. An upper-limit to the implanted dose was set by sputtering losses, which were moderate for targets with Pt on the top layer but exceeded 30 % of the

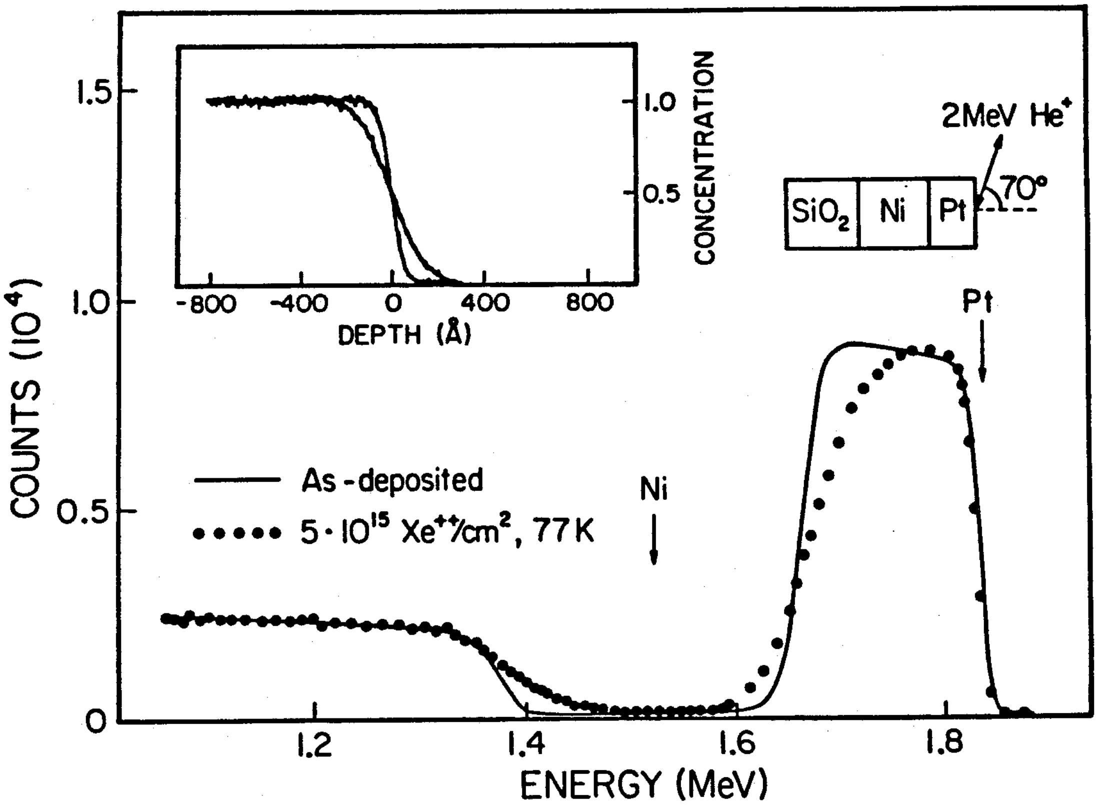

Fig. 2.1 Backscattering spectra of a Pt-Ni bilayer before and after ion mixing at 77 K. The insert shows the corresponding Ni signal transformed to a concentration versus depth profile.

initial thickness at the highest irradiation dose for targets with Au on the top.

Backscattering analysis[14] was performed with 2 MeV He^+ ions and with the target tilted at 70° to enhance depth resolution. The observed diffusion profiles were smooth and showed no steps that would indicate the presence of a compound in the mixed region. X-ray studies of mixed couples performed with a Read camera also showed no evidence of additional crystalline compound formation. The mixed regions are presumably either amorphous alloys or solid solutions of the two metals. The formation of amorphous and crystalline phases by ion mixing will be further discussed later (see Chapter 9).

2.3 The Heat of Mixing Effect

The high-energy backscattering edge of each bottom layer was numerically transformed to concentration versus depth profiles, assuming lateral uniformity over the mixed interface (see Appendix 1 for details). The transformed profiles were fitted, using a least-squares method, to the complementary error function (see Fig. 2.1),

$$C(x) = a(3) erfc\left[\frac{(x - a(1))}{a(2)}\right] + a(4), \tag{2.1}$$

where $C(x)$ is the atomic concentration at depth x and $a(1)$ through $a(4)$ are fitting variables. $[a(2)]^2 = 4Dt$, analogues to diffusion, characterizes the amount of mixing at the interface. Concentration profiles which depart significantly from the complementary error function were observed for only a few bilayers (e.g., Pt-Ti, Au-Ti) at the highest irradiation doses. In these cases, $4Dt$ was determined at the 1:1 concentration by a numerical Boltzmann-Matano analysis of the diffusion profile.[15] A linear relationship between $4Dt$ and the dose ϕ is observed (see Fig. 2.2); the slope of each line $d(4Dt)/d\phi$ is obtained by linear regression analysis. $d(4Dt)/d\phi$ characterizes the mixing rate of each bilayer. In Fig. 2.3, $d(4Dt)/d\phi$ is plotted against the

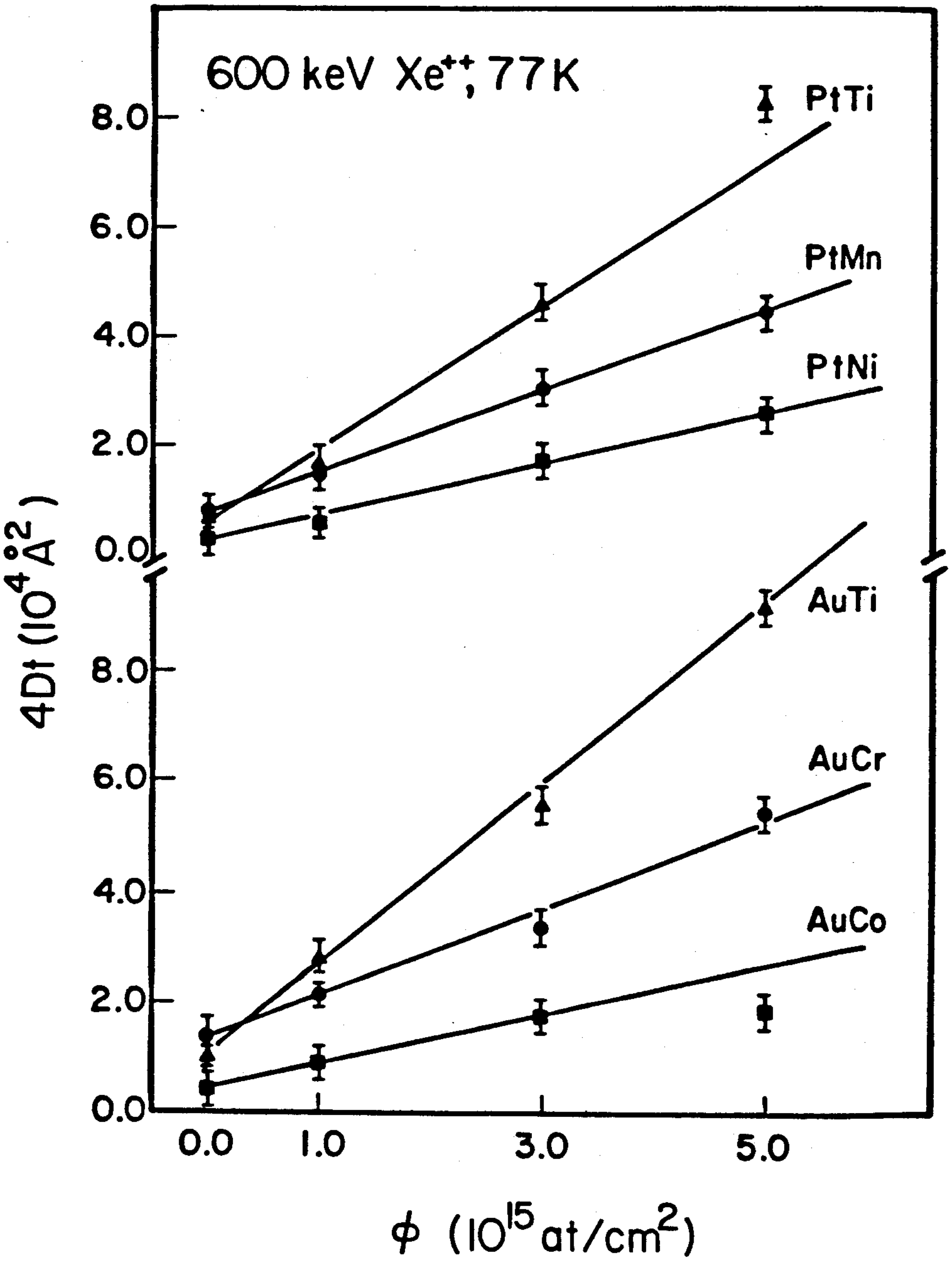

Fig. 2.2 The square of the amount of mixing $4Dt$ versus dose ϕ for $5d-3d$ bilayers irradiated with 600 keV Xe^{++} at 77 K.

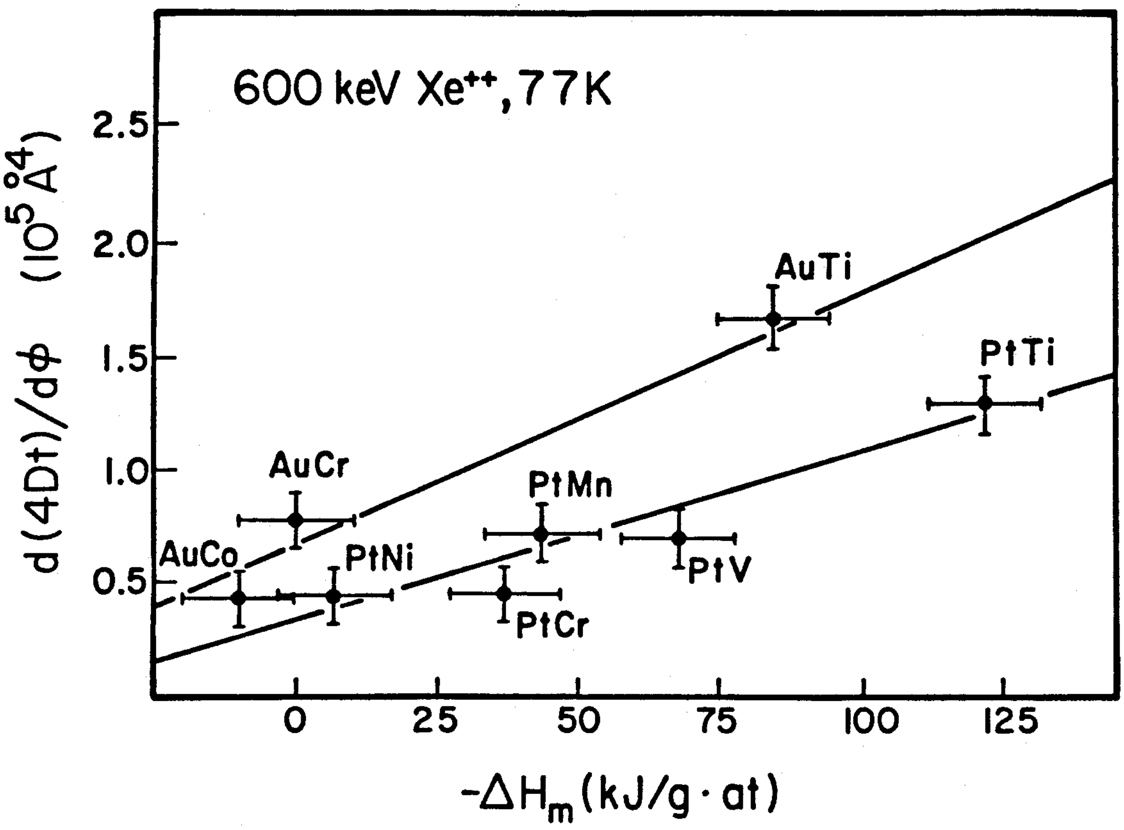

Fig. 2.3 Correlation between the mixing rate $d(4Dt)/d\phi$ and Miedema's heat of mixing ΔH_m for bilayers irradiated with 600 keV Xe^{++} at 77 K.

corresponding heat of mixing value, ΔH_m, taken from Miedema[11]. There exists a striking correlation between these two parameters. The value of ΔH_m is taken to be the heat of formation of intermetalllic compound at a one-to-one composition. In effect, ΔH_m is the solid-state heat of mixing. According to Ref. 12, the liquid heat of mixing ΔH_m^l at the same composition simply relates to ΔH_m by an approximation, $\Delta H_m^l = 0.659 \times \Delta H_m - 0.233$ (in unit of kJ/mole). Either set of heat of mixing parameters is thus adequate for demonstrating the chemical effect.

The contribution of collisional cascade mixing to $d(4Dt)/d\phi$ can be roughly estimated by calculating the effective interdiffusion coefficient due to pure collisional random walk processes (see Eq. (1.1)). Considering the similar displacement energies in the $3d$ elements of interest,[4] it can be verified that collisional processes cannot account for more than a 20% variation in the observed D, whereas the actual values vary by a factor of four for the systems under investigation. Roughening of the film surface due to sputtering could also result in the broadening of the backscattering signal from an interface, but this effect can be excluded, since it is not expected to depend on the nature of the bottom layer element.

To explain the observed differences in mixing rate, we propose a new model for ion mixing. This model combines Darken's analysis of chemical interdiffusion[15,16] with the regular solution approximation of binary systems.[9,10] Taking ΔH_m as the origin of the chemical driving force for diffusion, we can express the effective diffusion coefficient as (see Sections 4.2 and 4.3 for detailed discussions):

$$D = D_o\left(1 - 2\frac{\Delta H_m}{RT}\right), \tag{2.2}$$

where R is the Gas constant and T is the temperature.

The application of Darken's analysis to our ion mixing results is based on the assumption that a majority of mixing takes place in local regions where a quasithermal equilibrium is established and a temperature can be introduced. Furthermore, the characteristic kinetic energy of particles, or equivalently, the temperature, must not be too high as compared to the characteristic chemical biasing energy. If these conditions were not satisfied, the chemical biasing energy ΔH_{mix}, which is on the order of 1 eV/particle, would have been obscured owing to the much larger particle kinetic energies. This implies that the energy contained in the primary cascade has to be distributed over a large number of particles before chemical forces can come into play. Therefore, the chemical effect must prevail in the late stage of a fully developed cascade. Within this picture, we identify D with the effective interdiffusion coefficient near the one-to-one composition and identify D_o with the diffusion coefficient of pure random walk mixing. $E = \frac{3}{2}kT$ is, according the law of equipartition, the average kinetic energy per particle involved in the mixing process. A linear relationship between mixing rate $d(4Dt)/d\phi$ and ΔH_m is then predicted. From the slopes of the lines in Fig. 2.3, we estimate that E is about 1 eV. Since the initial kinetic energy of Xe^{++} is 600 keV, and assuming that the energy of the initial moving particle is equally shared by two particles after each binary collision, roughly 1.2×10^6 binary collisions have occurred when the average kinetic energy of each of the moving particles reaches 1 eV. Thus, a thermodynamic description of ion mixing in the late stages of collisional cascades, as suggested here, is plausible. The establishment of a near thermal equilibrium state in the energy range of about 1eV/particle is supported by a recent computer simulation in which the equipartition of kinetic and potential energy of the moving particles is observed to occur at around 1 eV/particle, indicating the approach to thermal equilibrium within the cascade.[17]

In the above analysis, we have assumed that the heat of mixing parameters defined by Miedema remain meaningful in the highly energetic cascade volume. This is probably true since the material density inside the cascade volume is likely to be bounded by that of the corresponding liquid and solid state. If our interpretation is correct, these results provide an experimental estimate of the average kinetic energy of atoms involved in the mixing process.

Applied strictly, Darken's diffusion analysis predicts a concentration profile that differs from the complementary error function profile assumed in our analysis, because the effective diffusion coefficient is now concentration-dependent (Eq. (2.2)). The treatment sketched here thus addresses only the basic features of the model. Note that marked deviations from a linear Dt versus ϕ behavior occur at the highest doses for systems with the largest negative (Pt-Ti) and positive (Au-Co) heat of mixing (see Fig. 2.2). This kind of behavior points toward either (i) a concentration dependence of D, or (ii) a role played by the heat, which must be released or absorbed during mixing. The additional amount of heat should influence the degree of mixing. Finally, our results show a systematic difference in the amount of mixing of couples with Au and those with Pt. This difference could be due to the influence of cohesive energy on ion mixing. The effect of cohesive energy will be discussed in Chapter 3.

Several groups have investigated the heat of mixing effect since our initial investigation. Their ion mixing results for metallic bilayers are in close agreement with those of this study.[18-22]

2.4 Summary

A relationship between $d(Dt)/d\phi$ and Miedema's heat of mixing parameter ΔH_m for binary metallic systems has been observed. A thermochemical model of ion mixing based on a chemically biased random walk process is proposed to explain this relationship. The experimental results of the present work suggest that chemical driving forces, characterized by ΔH_m, play an important role when the average kinetic energy per particle involved in the mixing process becomes comparable to the heat of mixing per atom. Since the latter is typically of the order of 1eV, this situation must prevail in the late stages of the prompt regime of the mixing process. Note also that according to the present model, binary systems with a sufficiently large and positive heat of mixing are predicted to exhibit uphill diffusion, i.e., phase separation (see Eq. (2.2)). This explains why systems with a misicibility gap in their equilibrium phase diagram are difficult to mix even by ion mixing.[8] From this investigation, it can be inferred that certain thermodynamic ideas are applicable in a description of the late stages of the prompt regime.

2.5 References

1. P. Sigmund and A. Gras-Marti, Nucl. Instrum. Methods **182/183**, 25 (1981).
2. S. Matteson, Appl. Phys. Lett. **39**, 288 (1981).
3. P. K. Haff and Z. E. Switkowski, J. Appl. Phys. **48**, 3383 (1977).
4. H. H. Andersen, Appl. Phys. **18**, 131 (1979).
5. A. J. Barcz, B. M. Paine, and M-A. Nicolet, Appl. Phys. Lett. **44**, 47 (1984).
6. T. Banwell, B. X. Liu, I. Golecki, and M-A. Nicolet, Nucl. Instrum. Methods **209/210**, 125 (1983).
7. F. Besenbacher, J. Bottiger, S. K. Nielsen, and H. J. Whitlow, Appl. Phys. **A 29**, 141 (1982).
8. Z. L. Wang, J. F. M. Westendorp, and F. W. Saris, Nucl. Instrum. Methods **209/210**, 115 (1983).
9. P. Haasen, *Physical Metallurgy* (Cambridge University Press, London, 1978).
10. R. A. Swalin, *Thermodynamics of Solids* (Wiley, New York, 1972).
11. A. R. Miedema, Philips Tech. Rev. **36**, 217 (1976).
12. A. K. Niessen, F. R. de Boer, R. Boom, P. F. de Chatel, W. C. M. Mattens, and A. R. Miedema, *CALPHAD*, **7**, 51 (1983).
13. R. Vianden, E. N. Kaufmann, and J. W. Rodgers, Phys. Rev. **B 22**, 63 (1980).
14. W. K. Chu, J. W. Mayer, and M-A. Nicolet, *Backscattering Spectrometry* (Academic Press, New York, San Francisco, London, 1978).
15. P. G. Shewmon, *Diffusion in Solids* (McGraw-Hill, New York, 1963), p. 126.
16. M. Hillert, in *Lectures on the Theory of Phase Transformation*, edited by H. I. Aaronson (AIMMPE, New York, 1975).
17. W. E. King and R. Benedek, J. Nucl. Materials **117**, 26 (1983).
18. F. d'Heurle, J. E. E. Baglin, and G. J. Clark, J. Appl. Phys. **57**, 1426 (1985).
19. R. S. Bhattacharya and A. K. Rai, J. Appl. Phys. **58**, 248 (1985).
20. A. K. Rai, R. S. Bhattacharya, M. H. Rashid, and A. W. McCormick, Mat.

Res. Soc. Symp. Proc. **54**, 231 (1986).

21. E. Rimini, M. Nastasi, J. Liu, J. C. Barbour, J-P. Hirvonen, and J. W. Mayer, Appl. Phys. Lett. **48**, 303 (1986).
22. J. F. M. Westendorp, Ph.D. Thesis (1986).

Chapter 3

INFLUENCE OF COHESIVE ENERGY ON ION MIXING OF METALLIC BILAYERS

3.1 Introduction

It was speculated at the end of Chapter 2 that the systematic differences in the amount of mixing of couples with Au and Pt might be due to their differences in cohesive energy. An intuitive argument suggests a possible influence of cohesive energy on ion mixing.

The cohesive energy of an element ΔH_{coh}, as defined in the well-known text book *Introduction to Solid State Physics* by Kittel,[1] is "the difference (free atom energy)-(crystal energy)." The higher the cohesive energy, the stronger atoms are bound together in a solid. Therefore, under identical ion irradiation conditions, there should be more disturbance created in low cohesive energy materials than in high cohesive energy ones. Furthermore, the activation energy of ordinary thermal diffusion scales with cohesive energy,[2,3] signaling the importance of cohesive energy in atomic transport phenomena.

In the usual theoretical description of cascade mixing, as seen in Chapter 1, the mixing rate is assumed to be inversely proportional to an effective displacement energy E_d inside the cascade volume.[4] E_d, around 30 eV for most metals,[5,6] is the energy required to produce a stable vacancy-interstitial pair and may be obtained experimentally. The dependence of the mixing rate on E_d in such ballistic models originates from the Kinchin-Pease binary collision model for cascades.[7]

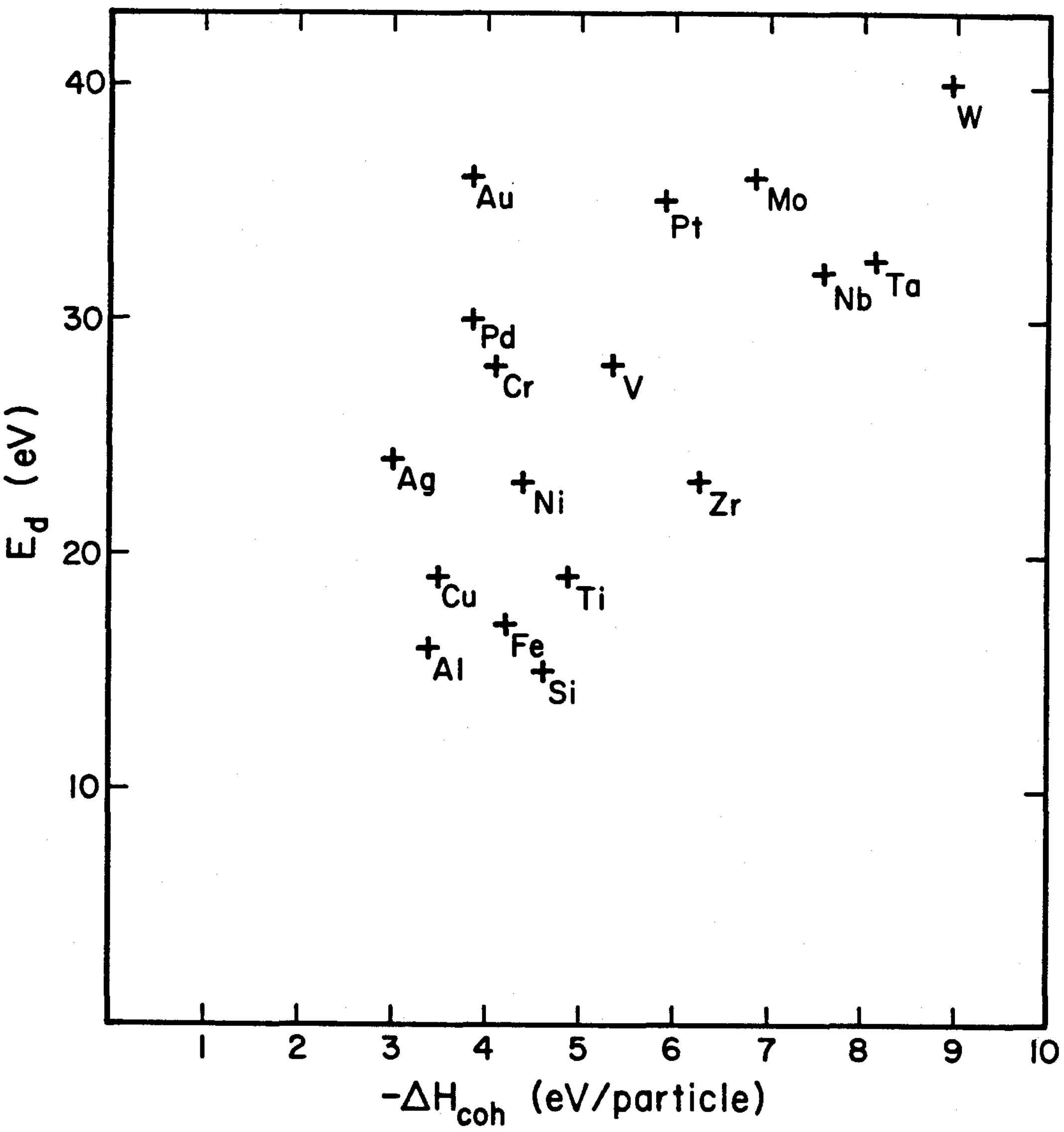

Fig. 3.1 Comparison between displacement energy[5] E_d and cohesive energy[1] ΔH_{coh} of elements.

There is at most a very poor correlation between cohesive energy and E_d, as demonstrated in Fig. 3.1. The values of ΔH_{coh} and E_d are from Refs. 1 and 5, respectively. A study of the dependence of the mixing rate on cohesive energy or E_d should enable us to differentiate between mechanisms for ion mixing. Furthermore, by eliminating the now known chemical effects[8] discussed in Chapter 2 (i.e., by choosing systems with $\Delta H_m = 0$), we can now separately investigate the role of E_d or ΔH_{coh}.

3.2 Ion Mixing of Metallic Bilayers with Near-Zero Heat of Mixing

The systems chosen to study are metallic $5d - 4d$ bilayers of Au-Ag, Pt-Pd, Hf-Zr, W-Mo, and Ta-Nb. Due to their isoelectronic atomic structure, similar Goldschmidt radii, density, ideal solution behavior, and corresponding near zero heat of mixing,[9] these binary systems are well suited for studying those effects that are not related to the chemical effects examined earlier. Furthermore, within each set of $5d$ and $4d$ elements, atoms have nearly the same atomic number and mass, while the mass difference between the top ($5d$) and bottom ($4d$) layer of each couple is sufficiently large so that mixing profiles can be studied by backscattering spectrometry. Finally, the set of elements selected covers a wide range of cohesive energy values.[10]

Thin bilayer films were prepared by electron-gun evaporation in an oil-free vacuum system with a base pressure below 10^{-7} Torr. All bilayers consisted of a layer of the $5d$ metal on top of a 2000-Å-thick layer of the $4d$ metal sequentially evaporated on a SiO_2 substrate. The top layer thickness was adjusted to the projected range of 600 keV Xe^{++} ions. To reduce sputtering effects, a thin layer of Si (100 Å) was evaporated on top of the samples. Ion mixing was performed at liquid nitrogen temperature in order to minimize radiation-enhanced diffusion. The vacuum during

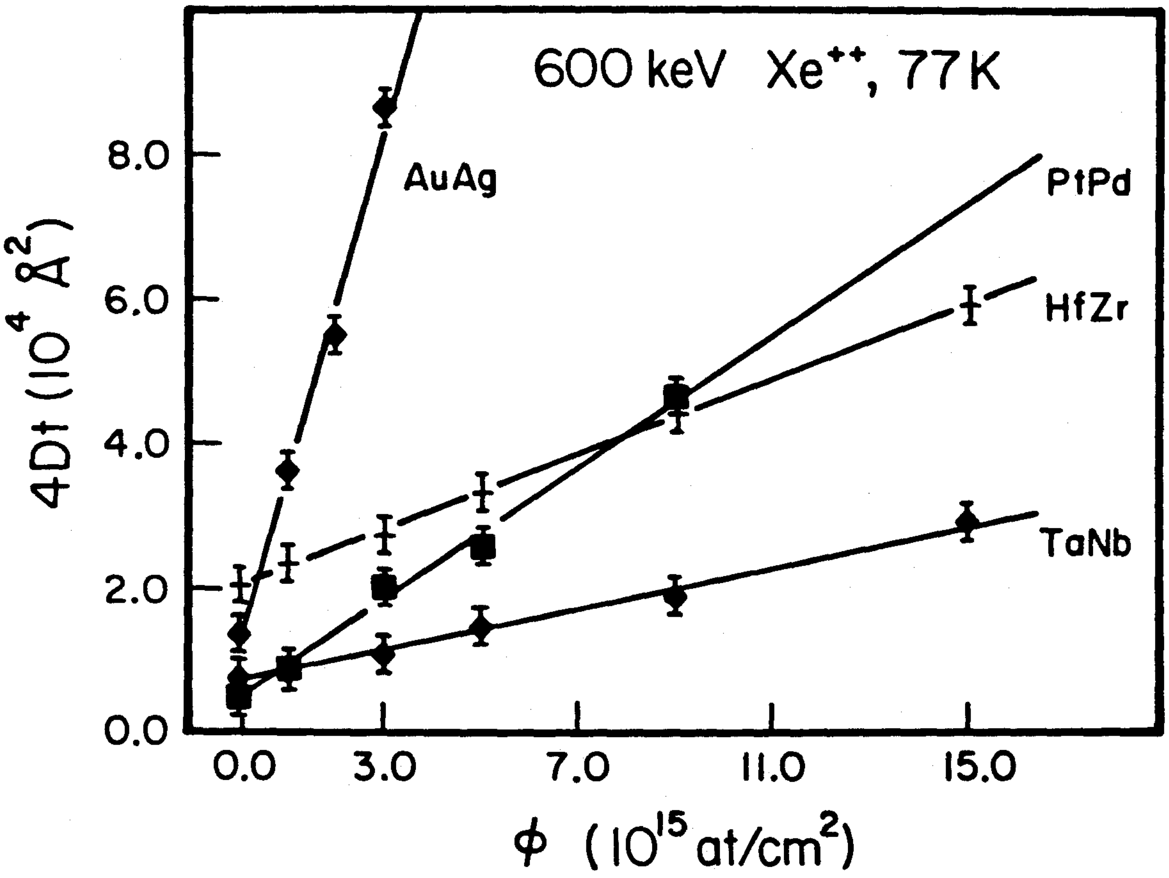

Fig. 3.2 The square of the amount of mixing $4Dt$ versus dose ϕ for $5d-3d$ bilayers irradiated with 600 keV Xe^{++} at 77 K.

the irradiation was maintained below 5×10^{-7} Torr. Implanted doses ranged from 10^{15} to 1.5×10^{16} Xe^{++}/cm^2 at a flux of about 200 nA/cm^2. Different samples were irradiated simultaneously to a specific dose in order to avoid dose and dose rate variations. Backscattering analysis was performed with 3 MeV He^{++} ions and a target tilted at 60°. The observed diffusion profiles were smooth and showed no steps that would indicate the presence of a compound in the mixed region. In the present case, the mixed regions are probably simple solid solutions as will be discussed later (see Chapter 9).

3.3 The Cohesive Energy Effect and Thermal Spike

The high-energy backscattering edge of each bottom layer was numerically transformed to concentration versus depth profiles, assuming lateral uniformity over the mixed interface. The transformed profiles were least squares fitted to complementary error functions (see Eq. (2.1)). A linear relationship between the square of the interface spreading, $4Dt = [a(2)]^2$, and the dose, ϕ, is observed in all cases and is shown in Fig. 3.2. The straight lines in Fig. 3.2 are fits obtained by a linear regression analysis. The slope of each line $d(4Dt)/d\phi$ characterizes the mixing rate of the corresponding bilayer. The nonzero value of $4Dt$ at $\phi = 0$ is due to the finite extension of the interface of the as-deposited samples and to the limited instrumental resolution. An estimate of the mixing rate, according to cascade mixing models, can be obtained using Eq. (1.1). Little difference in the mixing rate would be expected for the various bilayers involved (Table 3.1), but the experimental values vary by an order of magnitude and are substantially larger than the cascade mixing model predictions (Table 3.1).

In an effort to understand the origin of this discrepancy, we have plotted $[d(4Dt)/d\phi]^{-1}$ versus the average cohesive energy of each bilayer (Fig. 3.3). The

Table 3.1 Comparison between the mixing rate $d(4Dt)/d\phi_{bal}$ predicted by the ballistic model and the experimentally observed mixing rate $d(4Dt)/d\phi_{exp}$.

System (A-B)	$-\Delta H_{coh}$ (eV/particle)	E_d (eV)	$d(4Dt)/d\phi_{bal}$ (10^4 Å^4)	$d(4Dt)/d\phi_{exp}$ (10^4 Å^4)
Au-Ag	3.38	30.2	1.05	23.7
Pt-Pd	4.86	32.8	0.97	4.5
Hf-Zr	6.35	22.5	1.38	2.6
W-Mo	7.86	40.0	0.78	1.6
Ta-Nb	7.84	32.3	0.95	1.4

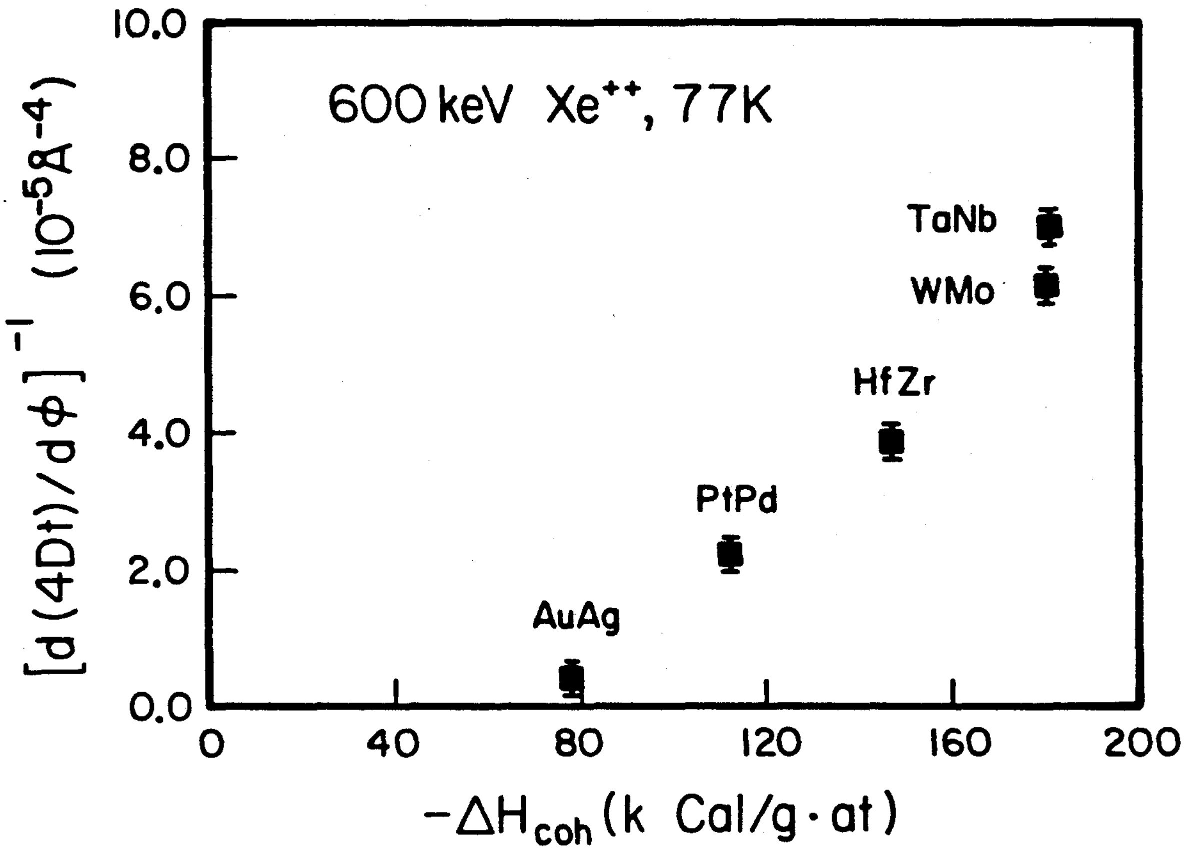

Fig. 3.3 Correlation between the mixing rate $d(4Dt)/d\phi$ and the average cohesive energy ΔH_{coh}.

latter is the arithmetic average of the heat of sublimation of the pure elements.[10] There exists a striking correlation between the mixing rate and the cohesive energy, but there is no correlation with E_d. From Table 3.1 and Fig. 3.3, we conclude that the dependence on E_d, predicted by the ballistic mixing models (Eq. (1.1)), is inappropriate for the present ion mixing experiment. To understand the cohesive energy effect, a closer examination of the displacement energy E_d is needed. E_d may be considered to consist of two major contributions. The first is the minimum energy required to remove an atom from its site and is, therefore, about equal to the formation energy of a vacancy ($\sim$ few eV); the second contribution is the extra energy needed to move the atom some distance away from the vacancy in order to avoid spontaneous recombination. In a low-density cascade with only one type of atom present, such as in electron or proton bombardment of pure elements, E_d is normally derived from the resulting concentration of stable radiation-produced vacancy-interstitial pairs.[6] It was found that the minimum separation between vacancies and interstitials was on the order of 10 Å. To move an atom this distance, an energy of some tens of eV is needed. Therefore, E_d in low-density cascades is dominated by the second part of the contribution to the displacement energy and the defect production is well described by a Kinchin-Pease-type model.[7] In ion mixing with heavy projectiles the situation can be different. Because of the dense collisional cascade, simultaneous and correlated motions of neighboring atoms are possible so that the medium may become rather liquidlike. In this case, the second contribution to E_d may be reduced. Furthermore, an atom ejected from its site and displaced by one or more atomic distances can contribute to ion mixing, whereas in a one-component system, the same atom must be sufficiently displaced even more to make a stable vacancy-interstitial pair. Therefore, it is not surprising that previous cascade models underestimate the actual amount of mixing (see Table 3.1).

In Chapter 2, it was shown that most of the mixing takes place when the kinetic energy per particle is in the 1eV range.[8] Such an energy is achieved in the thermalizing regime of a cascade, as described by various authors.[11,12] Assuming that the particle energy distribution has reached a state of local quasi-equilibrium in which most of the atoms in the cascade volume are in motion, we then adopt a thermal spike picture as proposed, for example, by Vineyard.[13] In this model, ion mixing is a thermally activated diffusion process with a jump rate $R = Aexp(-Q/T)$, where A is the frequency factor and Q is the activation energy. For a cylindrical spike, Vineyard obtains η, the total number of jumps per unit distance induced by one spike (see Section 4.4),

$$\eta = \frac{A\epsilon^2}{8\pi\kappa C Q^2}, \tag{3.1}$$

where ϵ is the energy deposited per unit path-length due to nuclear collisions, while κ and C are the temperature-independent thermal conductivity and specific heat of the lattice. It is a well-known fact that the thermal diffusion activation energy scales with the cohesive energy of the matrix, since the latter is a measure of the interatomic binding forces.[2,3] Let us assume that a similar scaling relationship exists in ion mixing, i.e., $Q = s\Delta H_{coh}$, where s is a constant. Since $Dt \propto \eta\phi$ (i.e., $Dt \propto$ the total number of jumps), we then obtain

$$d(Dt)/d\phi \propto (\Delta H_{coh})^{-2}. \tag{3.2}$$

In arriving at Eq. (3.2), we have taken A, κ, and C as constants for the metal pairs in our bilayer experiments. The results reported in Fig. 3.3 are in good accord with such a dependence. A quantitative comparison is not pursued until the next chapter, where the model is further refined and compared with additional experimental results.

Subsequent to the present work, the dependence of the ion mixing efficiency to cohesive energy has also been confirmed in a series of marker experiments by Kim *et al.*[14]

3.4 Summary

A direct correlation between the mixing rate of metallic bilayers and the cohesive energy of the corresponding elements has been established. The experiments were designed to isolate this effect from the chemical effect established earlier. We have offered an explanation for this correlation based on Vineyard's thermal spike model. These studies further illustrate the inadequacies of the binary cascade mixing models for the present experiments and demonstrate the usefulness of a thermodynamic description of ion mixing phenomena.

3.5 References

1. C. Kittel, *Introduction to Solid State Physics* (Wiley, New York, 1976), p. 73.
2. M. Doyama and J. S. Koehler, Acta Metall. **24**, 871 (1976).
3. G. P. Tiwari, in *Materials Science Forum*, Vol. 1, edited by G. E. Murch (Trans Tech, Aedermannsdorf, 1984), p. 171.
4. P. Sigmund and A. Gras-Marti, Nucl. Instr. Meth. **182-183**, 25 (1981).
5. H. H. Andersen, Appl. Phys. **18**, 131 (1979).
6. M. W. Thompson, *Defects and Radiation Damage in Metals* (Cambridge University Press, Cambridge 1969) p. 263.
7. G. H. Kinchin and R. S. Pease, Rep. Prog. Phys. **18**, 1 (1955).
8. Y.-T. Cheng, M. Van Rossum, M-A. Nicolet and W. L. Johnson, Appl. Phys. Lett. **45**, 185 (1984).
9. A. R. Miedema, Philips Tech. Rev. **36**, 105 (1981).
10. *Selected Values of the Thermodynamical Properties of the Elements*, edited by R. Hultgren, P.D. Desai, D.T. Hawkins, M. Gleiser, and K. K. Kelley (ASMT, Metal Parks, Ohio, 1973).
11. M. W. Guinan and J. H. Kinney, J. Nucl. Mat. **103-104**, 1319 (1981).
12. R. A. Weller, Nucl. Instr. Meth. **194**, 573 (1982).
13. G. H. Vineyard, Rad. Eff. **29**, 245 (1976).
14. S. J. Kim, B. M. Paine, M-A. Nicolet, R. S. Averbach, and D. Peak, to be published.

Chapter 4

FROM BASIC THERMODYNAMICS TO A PHENOMENOLOGICAL MODEL OF ION MIXING

4.1 Introduction

In the previous chapters, we have demonstrated the importance of thermodynamics in the description of ion mixing phenomena. In this chapter, we shall examine some of the underlying principles of thermodynamics and kinetics and construct a phenomenological model of ion mixing. We shall discuss the statistical thermodynamics of ideal and regular binary solutions in Section 4.2, a generalization of Fick's diffusion equation in Section 4.3, thermal spike models in Section 4.4, and finally the phenomenological model in Section 4.5.

4.2. Thermodynamics of Binary Alloys[1-3]

The state of a macroscopic system at thermal equilibrium can be specified completely in terms of *state variables.* Several commonly encountered state variable pairs, extensive and intensive, are N (number of particles) and μ (the chemical potential per particle), V (volume) and P (pressure), and T (temperature) and S (entropy). Other state variables used to describe the thermodynamic behavior of a system include various *thermodynamic potentials*, such as the internal energy U; enthalpy H; Helmholtz free energy F; Gibbs free energy G; and the grand potential Ω.

Not all of the state variables are independent. They are related to each other according to the laws of thermodynamics. For example,

$$dU \leq TdS - PdV + \sum_j \mu_j dN_j. \tag{4.1}$$

The equality holds for reversible changes and the inequality holds for spontaneous changes. Equation (4.1) states that *an equilibrium state at fixed S, V, and $\{N_i\}$ is the state of minimum internal energy.* From Eq. (4.1), we see that

$$T = (\frac{\partial U}{\partial S})_{V,N}, \tag{4.2a}$$

$$P = -(\frac{\partial U}{\partial V})_{S,N}, \tag{4.2b}$$

$$\mu_i = (\frac{\partial U}{\partial N_i})_{S,V,\{N_{j \neq i}\}}. \tag{4.2c}$$

T, P, and μ_i can be calculated if $U(S, V, N_i)$ is known.

Similar equations for other thermodynamic potentials may be obtained by *Legendre transformations.* For later use, we consider that the Gibbs free energy G. G can be obtained from the internal energy U by adding terms due to the thermal and mechanical couplings,

$$G = U - TS + PV = H - TS. \tag{4.3}$$

In this way the independent variables (S, V, N_i) are changed to variables (T, P, N_i). If we add the differentials of Eqs. (4.1) and (4.3), we obtain

$$dG \leq -SdT + VdP + \sum_j \mu_j dN_j; \tag{4.4}$$

thus

$$S = -(\frac{\partial G}{\partial T})_{P,N}, \tag{4.5a}$$

$$V = (\frac{\partial G}{\partial P})_{T,N}, \tag{4.5b}$$

$$\mu_i = (\frac{\partial G}{\partial N_i})_{T,P,\{N_{j \neq i}\}}. \tag{4.5c}$$

Eq. (4.4) states that *an equilibrium state of fixed T, P, N_i is the state of minimum Gibbs free energy.*

The usefulness of thermodynamic potentials is evident; they determine the direction of spontaneous changes of any macroscopic system. This allowed direction is designated by the inequality in equations such as Eqs. (4.1) and (4.4).

Thermodynamic potentials are also used to specify the condition for thermal equilibrium. For example, in a binary system consisting of A and B atoms with phases α and β in equilibrium at constant T and P, each change in G can be described as the sum of changes in both phases. Thus, in equilibrium,

$$\sum_{i=A,B} \mu_i^\alpha dN_i^\alpha + \sum_{i=A,B} \mu_i^\beta dN_i^\beta = 0, \tag{4.6}$$

with $dN_i^\alpha = -dN_i^\beta$; i.e.,

$$(\mu_A^\alpha - \mu_A^\beta)dN_A + (\mu_B^\alpha - \mu_B^\beta)dN_B = 0. \tag{4.7}$$

In accordance with our assumptions that α and β should remain in equilibrium for an interchange not only of A-atoms but also of B-atoms, the equilibrium conditions become

$$\mu_A^\alpha = \mu_A^\beta \quad \text{and} \quad \mu_B^\alpha = \mu_B^\beta; \tag{4.8}$$

i.e., $\mu_A =$ constant and $\mu_B =$ constant. As shall been seen in the next section, this condition is the starting point for a generalization of Fick's law of diffusion.

In practice, thermodynamic potentials may be obtained experimentally by meas-uring various state variables and performing a numerical integration according to equations such as Eqs. (4.2) and (4.3). They may also be obtained from first-principle theoretical calculations. But more often one starts off from simplified models of actual macroscopic systems, as in the study of binary alloys.

In calculating thermodynamic quantities of binary alloys, one useful model approach is to assume that the interaction between ions may be treated by a pairwise model. That is, the properties of a system may be represented by the sum of interactions between neighboring pairs of ions, and any complications due to three-body interactions, for example, may be ignored.

In order to calculate the Gibbs free energy of an alloy using the pair-potential models, let us suppose that there are N_A atoms of type A and N_B atoms of type B. Let P_{AA}, P_{BB}, and P_{AB} denote the numbers of the respective pair types and let H_{AA}, H_{AB}, and H_{BB} denote the corresponding pair enthalpy. The enthalpy of the solution is given by

$$H = P_{AA}H_{AA} + P_{AB}H_{AB} + P_{BB}H_{BB}. \tag{4.9}$$

After a simple counting of the number of pairs and the number of each element,[2] we obtain

$$H = \frac{1}{2}ZN_AH_{AA} + \frac{1}{2}ZN_BH_{BB} + P_{AB}\left[H_{AB} - \frac{1}{2}(H_{AA} + H_{BB})\right], \tag{4.10}$$

where Z is the coordination number. The last term on the right-hand side is called the heat of mixing and is denoted by ΔH_m.

The Ideal Solution Model

Here the enthalpy is assumed to be independent of the arrangement of N_A atoms of type A and N_B atoms of type B. This is equivalent to assuming that $\Delta H_m = 0$. The number of distinguishable arrangements ω of the atoms on the $N = N_A + N_B$ lattice sites is given by

$$\omega = \frac{N!}{(N_A)!(N_B)!} = \frac{N!}{(c_AN)!(c_BN)!}, \tag{4.11}$$

where $c_{A,B} = N_{A,B}/N$ is the concentration of A or B. Using Stirling's formula, we see that the ***entropy of mixing*** is

$$S = k \ln \omega = -Nk(c_A \ln c_A + c_B \ln c_B). \tag{4.12}$$

The Gibbs free energy of the ideal solution is

$$G = H - TS = c_A H_A^\circ + c_B H_B^\circ + NkT(c_A \ln c_A + c_B \ln c_B), \tag{4.13a}$$

where $H_{A,B}^\circ = \frac{1}{2} Z N H_{AA,BB}$ is the enthalpy of the pure element A or B. G and $H_{A,B}^\circ$ are quantities in units of energy/mole if N is equal to Avogadro's number. If other entropy terms of the pure elements, such as the vibrational entropy, are included, the Gibbs free energy of the ideal solution becomes

$$G = c_A G_A^\circ + c_B G_B^\circ + NkT(c_A \ln c_A + c_B \ln c_B), \tag{4.13b}$$

where $G_{A,B}^\circ$ is the Gibbs free energy of the pure element A or B. The chemical potential of the component B in the alloy can be obtained from Eqs. (4.13b) and (4.5c)[2,3]

$$\mu_B^{id} = \mu_B^\circ + kT \ln c_B, \tag{4.14}$$

where μ_B° does not depend on c_B.

The Regular Solution Model

The regular solution model assumes that at relatively high temperatures the nearest-neighbor interaction is so weak, $\varepsilon \equiv H_{AB} - \frac{1}{2}(H_{AA} + H_{BB}) < kT/4$, that it does not influence the random distribution of A and B atoms; thus, the ideal entropy of mixing (Eq. (4.12)) can be used and $P_{AB} = c_A c_B Z N$.[2] The heat of mixing is then given by

$$\Delta H_m = c_A c_B N \delta, \tag{4.15}$$

where $\delta = Z\varepsilon$ is independent of composition and ΔH_m is a parabolic function of composition.

If there is an attractive interaction between unlike ions, the enthalpy of the A-B pair will be more negative than the enthalpy of the A-A or the B-B pair. Hence, δ will be negative in sign and will yield a negative value of the heat of mixing. Conversely, if there is a repulsive interaction between unlike atoms, δ will be positive and ΔH_m will also be positive.

The Gibbs free energy of the regular solution model thus equals

$$G = c_A G_A^{\circ} + c_B G_B^{\circ} + NkT(c_A \ln c_A + c_B \ln c_B) + c_A c_B N\delta. \tag{4.16}$$

The chemical potential, for example, of the B component, can be obtained from Eqs. (4.16) and (4.5c)[2,3],

$$\mu_B^{reg} = \mu_B^{\circ} + \delta c_A^2 + kT \ln c_B. \tag{4.17}$$

Though the heat of mixing ΔH_m may be obtained experimentally, in the following discussions we shall use primarily the values derived from Miedema's phenomenological model.[4,5] Some justification for the validity of the Miedema approach has been obtained from first-principle calculations on binary alloys.[6-9]

One of the important applications of the regular solution model has been in the study of order-disorder transitions in alloys.[1,2] The elegance of the regular solution model is so attractive that it has remained in most textbooks on the thermodynamics of solids. In the following, we shall demonstrate a novel application of this model to ion beam mixing. In this case, the condition $\varepsilon < kT/4$ is most likely satisfied because ion mixing occurs at some very high effective temperature (see Chapter 2).

4.3 Diffusion With and Without Chemical Driving Forces[1,10,11]

Random Walk without Biasing

The analogy between heat transfer and mass transfer was recognized by Fick in the 1850s. He first put forward the mathematical theory of diffusion by reformulating the equations for heat conduction derived some years earlier by Fourier. The basic assumption in his theory, Fick's first law of diffusion, states that the rate of transfer of the diffusing substance through a unit cross-sectional area is proportional to the concentration gradient in the direction normal to the section. In one dimension this becomes

$$j = -D\frac{\partial c}{\partial x}, \tag{4.18}$$

where j is the rate of transfer per unit area of cross section, or flux, c the concentration of diffusing substance, x the space coordinate, and D is called the diffusion coefficient. Fick's first law is in accord with the observation that flux goes to zero as a system becomes homogeneous.

By simply applying the law of conservation of matter to Fick's first law, one obtains the diffusion equation. In the one-dimensional case with constant D the diffusion equation is given by

$$\frac{\partial c}{\partial t} = D\frac{\partial^2 c}{\partial x^2}. \tag{4.19}$$

Equations (4.18) and (4.19) should be viewed as phenomenological descriptions of the diffusion process, because they are not concerned with the underlying mechanisms of diffusion. But the importance of these equations should not be overlooked. Numerous problems have been studied by using Eqs. (4.18) and (4.19).[10] Nevertheless, an understanding of diffusion phenomena at the atomic level would be fruitful. To begin, let us consider the problem of a random walk in one dimension. We will assume that a particle moves along the x- axis with a step size l and that the time between steps is τ. The probability $P_1(n_2l, s\tau)$ that the particle is at $x = n_2l$ and $t = s\tau$ can be written as

$$P_1(n_2l, s\tau) = \sum_{n_1} P_1(n_1l, (s-1)\tau) P_{1|1}(n_1l, (s-1)\tau \mid n_2l, s\tau), \tag{4.20}$$

where $n_{1,2} = 0, \pm 1, \pm 2, ...$ indicates the position of the particle and s indicates the time step. The quantity $P_{1|1}(n_1l, (s-1)\tau \mid n_2l, s\tau)$ is the conditional probability that, in one time step, the particle will go from n_1 to n_2. Equation (4.20) is the discrete version of the more familiar formula $P_1(x_2, t_2) = \int P_1(x_1, t_1) P_{1|1}(x_1, t_1 \mid x_2, t_2) dx_1$, which relates the probability density at different times.[1] If there is an *equal* probability of taking a step to the left or to the right,

$$P_{1|1}(n_1l, (s-1)\tau \mid n_2l, s\tau) = \frac{1}{2}\delta_{n_2, n_1+1} + \frac{1}{2}\delta_{n_2, n_1-1}, \tag{4.21}$$

and Eq. (4.20) becomes

$$P_1(nl, s\tau) = \frac{1}{2}P_1((n-1)l, (s-1)\tau) + \frac{1}{2}P_1((n+1)l, (s-1)\tau). \tag{4.22}$$

Using this equation we obtain a finite difference equation for the probability distribution in the form

$$\frac{P_1(nl, s\tau) - P_1(nl, (s-1)\tau)}{\tau}$$
$$= \frac{l^2}{2\tau}\left[\frac{P_1((n+1)l, (s-1)\tau) + P_1((n-1)l, (s-1)\tau) - 2P_1(nl, (s-1)\tau)}{l^2}\right]. \tag{4.23}$$

Taking $l \to 0$ and $\tau \to 0$ and keeping $D = l^2/\tau$ constant, we see that Eq. (4.23) is exactly the discrete form of the diffusion equation

$$\frac{\partial P_1(x,t)}{\partial t} = D\frac{\partial^2 P_1(x,t)}{\partial x^2}. \tag{4.24}$$

The equivalence between the Fick's formulation and the random walk approach is established if we treat Eq. (4.19) as an "ensemble" of many particles undergoing a random walk under "equivalent" physical conditions, rather than considering the motion of a single particle over a length of time.

Furthermore, the random walk approach reveals the meaning of the diffusion coefficient D, which is given explicitly by $D = l^2/2\tau$. It thus provides a method for obtaining the diffusion coefficient in practice.

The random walk approach is based on the assumptions that there is an equal probability for a particle to jump in either a forward or backward direction and that this probability is independent of location and time. From these two assumptions, the usual diffusion equation is obtained. We shall demonstrate that these assumptions are valid in the ideal solution approximation, but that in general, for example, in the regular solution approximation, the diffusion equation has to be modified.

Biased Random Walk

In Section 4.2 we concluded that the equilibrium condition for a binary alloy at constant temperature and pressure is a constant chemical potential everywhere for each species. If now the system is perturbed slightly from equilibrium, it seems most reasonable to assume that the rate of return to equilibrium is proportional to the deviation from equilibrium. More specifically, the flux j_i is expected to be proportional to the gradients in chemical potential μ_i. Thus, in general, we write

$$j_B = -M_{BB}\frac{\partial \mu_B}{\partial x} - M_{BA}\frac{\partial \mu_A}{\partial x} - M_{B\varphi}\frac{\partial \varphi}{\partial x}, \qquad (4.25)$$

where φ is any relevant scalar potential.

In the following analysis we shall restrict our attention to the case in which the "cross coupling" terms $M_{i\neq j}$ are negligible in comparison to the "direct coupling" terms M_{ii}. This is a plausible assumption because one would expect that the main consequence of a disturbance in μ_A should be the movement of A atoms rather than B atoms. Pictorially, let us disturb an equilibrium binary two-phase system by moving an A atom from an α-phase to a β-phase. To restore equilibrium it is sufficient to move only an A atom back into the α-phase. Thus, we write

$$j_B = -M_{BB}\frac{\partial \mu_B}{\partial x}. \tag{4.26}$$

Effects due to the cross coupling terms $M_{i \neq j}$, however, are known to exist.[12]

The physical meaning of M_{BB} becomes clear as follows. In general, we can write $j_B = c_B v$, where v is the mean velocity of B atoms when acted upon by a driving force F. Furthermore, $v = \mathcal{M}_B F$, where $\mathcal{M}_B$ is the mobility of B atoms. In this case, the driving force is given by the gradient of the chemical potential,

$$j_B = c_B v = c_B \mathcal{M}_B F = -c_B \mathcal{M}_B \frac{\partial \mu_B}{\partial x}. \tag{4.27}$$

Therefore, $M_{BB} = c_B \mathcal{M}_B$.

Now let us substitute the expression for the chemical potential of the ideal solution, Eq. (4.14), into Eq. (4.27). We obtain

$$j_B = \frac{-M_{BB}kT}{c_B}\frac{\partial c_B}{\partial x} = -\mathcal{M}_B kT \frac{\partial c_B}{\partial x} = -D_B \frac{\partial c_B}{\partial x}. \tag{4.28}$$

In the last step we have used the Einstein relation $D = kT\mathcal{M}$. Equation (4.28) is identical to Fick's first law of diffusion (see Eq. (4.18)).

Similarly, if we combine the expression for the chemical potential in the regular solution model, Eq. (4.17), and Eq. (4.27), we find

$$\begin{aligned} j_B &= -\frac{M_{BB}kT}{c_B}\left(1 - \frac{2\delta c_A c_B}{kT}\right)\frac{\partial c_B}{\partial x} \\ &= -D_B\left(1 - \frac{2\delta c_A c_B}{kT}\right)\frac{\partial c_B}{\partial x} \\ &= -D_B\left(1 - 2\frac{\Delta H_m}{RT}\right)\frac{\partial c_B}{\partial x}, \end{aligned} \tag{4.29}$$

where R is the Gas constant. In the last step above we have used Eq. (4.15). To preserve the functional form of Fick's first law of diffusion, we identify the effective diffusion coefficient with

$$D_B^* = D_B\big(1 - 2\frac{\Delta H_m}{RT}\big). \tag{4.30}$$

The diffusion coefficient now is no longer composition-independent and it can be either ***positive*** or ***negative*** depending on the sign of ΔH_m and the ratio of $2\Delta H_m/RT$. For systems with a negative heat of mixing, the diffusion coefficient is increased as a result of the interactions between the two different species of atoms. For positive heat of mixing systems, it is the competition between the entropy term, which favors mixing, and the heat of mixing term, which opposes mixing that determines the sign of the diffusion coefficient.

Equation (4.30) is a special case of the more general Darken's equation for chemical diffusion; in the latter, the thermodynamic factor is given by $\big(1+\frac{\partial \log \gamma_B}{\partial \log c_B}\big)$, where γ_B is the activity coefficient for B atom in an A-B solution.[2,3,11] This factor reduces to $\big(1-2\frac{\Delta H_m}{RT}\big)$ in the regular solution approximation. The variation of diffusion coefficient with respect to concentration and temperature due to Darken's thermodynamic factor has been reported on several occasions for thermal diffusions.[13,14] It is only very recently, however, that this thermodynamic factor has been shown to be relevant to ion mixing (see Chapter 2).

4.4 Thermal Spike Concepts

The *thermal spike* idea has been around now for over 30 years. A spike or a high-density cascade can be described as a local volume in which essentially all the atoms are simultaneously in motion.[15] A *thermal spike* is a spike in which the velocity distribution of moving particles resembles the Maxwell-Boltzmann distribution.[16]

Thus, the concept of a local temperature can be introduced through the use of the law of equipartition of energy. Desired physical parameters can be obtained for a system experiencing a thermal spike if their behavior as a function of temperature is known. The temperature can be calculated simply by solving the thermal diffusion equation under specified boundary conditions. During the last 15 years a significant amount of experimental evidence on spike effects has been obtained from sputtering and ion implantation studies.[16]

The heat of mixing effect and the cohesive energy effect described in Chapters 2 and 3 emphasize the need for a thermodynamic approach to problems in ion mixing. Therefore, it is only natural to incorporate the thermal spike idea into our phenomenological description of ion mixing.

We shall follow very closely Vineyard's approach[17] to cylindrical thermal spikes because his solution entails a simple analytic form, which can be easily extended to include the heat of mixing effect.

The Cylindrical Spike

The equation of heat conduction in an isotropic, uniform medium with thermal conductivity κ and specific heat C is

$$\nabla \cdot \kappa \nabla T = C \frac{\partial T}{\partial t}. \tag{4.31}$$

Assume now that κ and C are temperature-dependent with the form[17]

$$\kappa = \kappa_o T^{n-1}, \tag{4.32a}$$

$$C = C_o T^{n-1}, \tag{4.32b}$$

where κ_o and C_o are constants and n is any positive number.

In the cylindrical spike, energy is suddenly introduced at $t = 0$ along an infinite straight line at constant density ϵ per unit length. Denoting the distance perpendicular to the line by s, the initial distribution of added internal energy per unit volume is $\epsilon\delta^2(s)$, where $\delta^2(s)$ is the two-dimensional delta function. The initial condition of the temperature distribution is given by

$$\int C dT = \frac{C_o}{n} T(s,0) = \epsilon\delta^2(s). \tag{4.33}$$

Solving Eq. (4.31) subject to the initial condition Eq. (4.33), we obtain the temperature distribution. In the case of zero initial ambient temperature, the result is

$$T(s,t) = \left[\frac{n\epsilon}{4\pi\kappa_o t}\right]^{1/n} e^{-C_o s^2/4n\kappa_o t}. \tag{4.34}$$

The Total Number of Jumps

Let us suppose that there is a thermally activated rate process such as the jumping of atoms of the material from one site to another. It is desirable to calculate a quantity η defined as the total number of jumps induced in one spike per unit length of the spike. Assume that the rate of jumping (the number of jumps per unit volume per unit time) in the material when it is at temperature T is given by $Ae^{-Q/T}$, where A and Q are independent of temperature. Then,

$$\eta = \int_0^\infty 2\pi s ds \int_0^\infty A e^{-Q/T(s,t)} dt. \tag{4.35}$$

Changing variables from t and s to τ and σ, where

$$t = \frac{n\epsilon}{4\pi\kappa_o}\left(\frac{\tau}{Q}\right)^n, \tag{4.36a}$$

and

$$s = 2\left[n\frac{\kappa_o}{C_o} t \ln\sigma\right]^{1/2}, \tag{4.36b}$$

the expression for η becomes

$$\eta = \frac{n^4 A\epsilon^2}{4\pi C_o \kappa_o Q^{2n}} \int_1^\infty \frac{d\sigma}{\sigma} \int_0^\infty \tau^{2n-1} e^{-\tau\sigma} d\tau. \tag{4.37}$$

The integrals are elementary and one finds

$$\eta = \frac{n^3 \Gamma(2n) A\epsilon^2}{8\pi\kappa_o C_o Q^{2n}}. \tag{4.38}$$

where $\Gamma(2n)$ is the gamma function of argument $2n$. If the thermal conductivity and the specific heat are constant of temperature, then $n = 1$ and Eq. (4.38) becomes

$$\eta = \frac{A\epsilon^2}{8\pi\kappa C Q^2}. \tag{4.39}$$

The power law dependence on a fundamental energy scale, such as the activation energy Q in Eq. (4.39), distinguishes spike models from linear cascade models and offers a means of determining the correct model experimentally.

Equation (4.39) was used in Chapter 3, in conjunction with a scaling relationship between activation energy and cohesive energy, to provide a rationale for the observed correlation between the mixing rate and the cohesive energy.

In spite of the successes of thermal spike models in explaining problems in sputtering and ion mixing, the understanding of how a cascade develops into a spike has been extremely poor. In Chapter 6, we shall study this problem using the concept of fractals. For now, let us continue our development of a phenomenological model of ion mixing.

4.5 A Phenomenological Model of Ion Mixing

We can extend Vineyard's thermal spike model to include the heat of mixing effect as follows. We have shown in Section 4.3 that in the regular solution approximation, the effective diffusion coefficient for chemically biased diffusion is given by

$D = D_o(1-2\Delta H_m/T)$ (Eq. (4.30)). Thus, for a binary system with $\Delta H_m \neq 0$, the effective rate of jumping (the number of jumps per unit volume per unit time) at temperature T is given by $Ae^{-Q/T}(1-2\frac{\Delta H_m}{T})$, instead of by $Ae^{-Q/T}$ as in Section 4.4. We can similarly define a quantity η_c as the total number of jumps induced by one spike per unit length of the spike; it is given by

$$\eta_c = \int_0^\infty 2\pi s ds \int_0^\infty Ae^{-Q/T(s,t)}\left[1-2\frac{\Delta H_m}{T(s,t)}\right]dt. \tag{4.40}$$

After performing the same variable changes as in Section 4.4, we find that the expression for η_c becomes

$$\begin{aligned}\eta_c = \frac{n^4 A\epsilon^2}{4\pi C_o \kappa_o Q^{2n}}\bigg(&\int_1^\infty \frac{d\sigma}{\sigma}\int_0^\infty \tau^{2n-1}e^{-\tau\sigma}d\tau \\ &-2\frac{\Delta H_m}{Q}\int_1^\infty d\sigma \int_0^\infty \tau^{2n}e^{-\tau\sigma}d\tau\bigg)\end{aligned}\quad. \tag{4.41}$$

The integrals are all elementary and we find

$$\eta_c = \frac{n^3\Gamma(2n)A\epsilon^2}{8\pi\kappa_o C_o Q^{2n}}\left[1-4n\frac{\Delta H_m}{Q}\right]. \tag{4.42}$$

When thermal conductivity and specific heat are constants, $n = 1$, we have

$$\eta_c = \frac{A\epsilon^2}{8\pi\kappa C Q^2}\left(1-4\frac{\Delta H_m}{Q}\right). \tag{4.43}$$

After a dose ϕ (ions/cm^2) of irradiation, the total number of jumps in the material is proportional to $\eta_c\phi/\rho$, where ρ is the atomic density (in units of cm^{-3}). Therefore, the square of the spreading of the interface $4Dt$ is proportional to $\eta_c\phi r_c^2/\rho$, where r_c is the characteristic jumping distance. We may assume that r_c scales with the inter-atomic distance, i.e., $r_c = s_1\rho^{-1/3}$, where s_1 is a constant. Furthermore, let us extend to ion mixing the scaling relationship between the activation energy of diffusion and the cohesive energy of the matrix, i.e., $Q = -s_2\Delta H_{coh}$, where s_2 is a positive constant. We obtain the following equation,

$$\frac{d(4Dt)}{d\phi} = \frac{K_1\epsilon^2}{\rho^{5/3}(\Delta H_{coh})^2}\left(1+K_2\frac{\Delta H_m}{\Delta H_{coh}}\right), \tag{4.44}$$

where K_1 depends on κ, C, and A while $K_2 = 4/s_2$ is a constant. We have analyzed our ion mixing data, presented in Chapters 2 and 3, by taking both K_1 and K_2 as constants. The values $K_1 = 0.037\text{Å}$ and $K_2 = 27$ are obtained from a least-squares fit. These results are summarized in Table (4.1), together with the mixing rate calculated from Eq. (4.44), using the above values of K_1 and K_2. A comparison of the experimental values for the mixing rate with those obtained from the proposed expression indicates a high degree of correlation. Additional experimental results agree well with the predictions of this equation as will be seen in the next chapter.

Table 4.1 Comparison between the mixing rate calculated using Eq. (4.44) $d(4Dt)/d\phi_{cal}$ and the experimentally observed mixing rate $d(4Dt)/d\phi_{exp}$.

System (A-B)	$-\Delta H_m$[a] (kJ/g at)	$-\Delta H_{coh}$[b] (eV/particle)	ϵ[c] (10^2 eV/Å)	ρ[d] (10^{-2}Å^{-3})	$d(4Dt)/d\phi_{exp}$[e] (10^5 Å^4)	$d(4Dt)/d\phi_{cal}$[f] (10^5 Å^4)
Pt-Ti	122	6.60	4.45	6.14	1.28	1.07
Pt-V	68	6.27	4.91	6.92	0.69	0.78
Pt-Mn	43	4.82	5.31	7.40	0.73	1.19
Pt-Cr	36	5.34	5.30	7.47	0.45	0.78
Pt-Ni	7	5.21	5.82	7.88	0.45	0.44
Au-Ti	84	5.20	4.14	5.78	1.63	1.48
Au-Cr	0	3.96	4.98	7.12	0.78	0.48
Au-Co	-11	3.99	5.39	7.43	0.45	0.12
Pt-Pd	0	4.86	5.54	6.71	0.45	0.43
Hf-Zr	0	6.34	3.55	4.40	0.26	0.22
W-Mo	0	7.86	5.19	6.63	0.16	0.16
Ta-Nb	0	7.84	4.45	5.56	0.14	0.15
Au-Ag[g]	0	3.38	4.80	5.88	2.37	0.84

[a] Heat of mixing for $A_{50}B_{50}$, A. R. Miedema, Philips Tech. Rev. **36**, 217 (1976).

[b] Cohesive energy for $A_{50}B_{50}$ calculated from $\Delta H_{coh} = \frac{1}{2}(\Delta H_A^\circ + \Delta H_B^\circ) + \Delta H_m$,[2] where ΔH_A° and ΔH_B° are the cohesive energies of the corresponding solids A and B. ΔH_A° and ΔH_B° are obtained from C. Kittel, *Introduction to Solid State*

Physics, 5th ed. (Wiley, NY, 1976), and from *Selected Values of the Thermodynamical Properties of the Elements*, edited by R. Hultgren, P. D. Desai, D. T. Hawkins, M. Gleiser, and K. K. K. Kelley (ASMT, Metal Parks, Ohio, 1973).

[c] Average energy deposited per unit length due to nuclear collision at the interface of A and B, J. P. Biersach and J. F. Ziegler, in *Ion Implantation Techniques*, edited by H. Ryssel and H. Glawisching (Springer-Verlag, Berlin, 1982).

[d] Average atomic density for $A_{50}B_{50}$ obtained from averaging the atomic densities of the pure elements A and B.

[e] Experimentally observed mixing rate $d(4Dt)/d\phi$ as described in Chapters 2 and 3.

[f] Calculated mixing rate $d(4Dt)/d\phi$ using Eq. (4.44) with the least-squares fitted values, $K_1 = 0.037$ Å and $K_2 = 27$.

[g] This system is not considered in the determination of K_1 and K_2 values because it would contribute to a poor quality least-squares fit.

4.6 References

1. L. E. Reichi, *A Morden Course in Statistical Physics* (University of Texas Press, Austin, 1980).
2. R. A. Swalin, *Thermodynamics of Solids*, 2nd edition (Wiley, New York, 1972).
3. P. Haasen, *Physical Metallurgy* (Cambridge University Press, London, 1978).
4. A. R. Miedema, Philips Tech. Rev. **36**, 217 (1976).
5. A. K. Niessen, F. R. de Boer, R. Boom, P. F. de Chatel, W. C. M. Mattens, and A. R. Miedema, *CALPHAD* **7**, 51 (1983).
6. J. R. Chelikowsky and J. C. Phillips, Phys. Rev. Lett. **39**, 1687 (1977).
7. D. G. Pettifor, Phys. Rev. Lett. **42**, 846 (1978).
8. A. R. Williams, C. D. Gelatt, Jr., and V. L. Moruzzi, Phys. Rev. Lett. **44**, 429 (1980).
9. D. G. Pettifor, J. Less - Common Metals **114**, 7 (1985).
10. J. Crank, *The Mathematics of Diffusion*, 2nd edition (Oxford University Press, London, 1975).
11. P. G. Shewmon, *Diffusion in Solids* (McGraw-Hill, New York, 1963).
12. J. R. Manning, *Diffusion Kinetics for Atoms in Crystals* (Van Nostand, Princeton, 1968).
13. J. E. Reynolds, B. L. Averbach, and M. Cohen, Acta. Metall. **5**, 29 (1957).
14. J. Võlkl and G. Alefeld, in *Hydrogen in Metals*, Vol.1, edited by G. Alefeld and J. Võlkl (Springer-Verlag, Berlin, 1978), p. 321.
15. P. Sigmund, Appl. Phys. Lett. **25**, 169 (1974).
16. D. A. Thompson, Rad. Effects **56**, 105 (1981).
17. G. H. Vineyard, Rad. Effects **29**, 245 (1976).

Chapter 5

MORE ON THE PHENOMENOLOGICAL MODEL OF ION MIXING

5.1 Introduction

Additional experimental studies have been carried out to test the phenomenological model of ion mixing developed in the previous chapters. From this model, the effective activation energy is estimated for diffusion in the late stages of a dense collisonal cascade.

5.2 Ion Mixing of $5d-4d$ Metallic Bilayers*

Experiments performed to test the phenomenological equation (Eq. (4.44)) of ion mixing consisted of ion mixing of $5d-4d$ metallic bilayers using 600 keV Xe^{++} ions. The bilayers are made up of the $5d$ metals Hf and Pt as the top layers and with a series of $4d$ metals as the bottom layers. The Hf series includes the pairs Hf-Zr, Hf-Ru, Hf-Pd, and Hf-Ag. The Pt series includes Pt-Zr, Pt-Nb, Pt-Mo, and Pt-Ru. The difference in atomic mass between the top and bottom layers is large enough so that their signals will not overlap in backscattering spectrometry. Pertinent parameters for these systems are listed in Table 5.1.[1–4]

The bilayer samples were prepared by electron-beam evaporation in an oil-free vacuum system. The base pressure was less than 5×10^{-8} Torr, and the pressure remained below 3×10^{-7} Torr during evaporation. Each bilayer consisted of a 600 Å Hf or 375 Å Pt layer on top of a 1500 Å layer of a $4d$ metal. The top layer thickness

---

* This section is based on the Senior Thesis by T. W. Workman, Caltech (1986).

Table 5.1 Comparison between the mixing rate calculated using Eq. (4.44) $d(4Dt)/d\phi_{cal}$ and the experimentally observed mixing rate $d(4Dt)/d\phi_{exp}$ for $5d - 4d$ metallic bilayers.

System (A-B)	$-\Delta H_m$[a] (kJ/g at)	$-\Delta H_{coh}$[b] (eV/particle)	ϵ[c] (10^2 eV/Å)	ρ[d] (10^{-2}Å^{-3})	$d(4Dt)/d\phi_{exp}$[e] (10^5 Å^4)	$d(4Dt)/d\phi_{cal}$[f] (10^5 Å^4)
Pt-Zr	151	7.61	4.80	5.46	1.21	1.13
Hf-Pd	122	6.43	4.40	5.66	1.17	1.20
Pt-Nb	104	7.78	5.15	6.09	0.79	0.75
Hf-Ru	77	7.39	4.50	5.94	0.50	0.55
Pt-Mo	42	6.77	5.40	6.52	0.37	0.56
Hf-Ag	31	5.02	4.15	5.19	0.41	0.88
Pt-Ru	2	6.31	5.70	6.99	0.27	0.25
Hf-Zr	0	6.35	3.55	4.41	0.23	0.19

[a] Heat of mixing for $A_{50}B_{50}$, A.R. Miedema, Philips Tech. Rev. **36**, No. 8, 217 (1976).

[b] Cohesive energy for $A_{50}B_{50}$ calculated from $\Delta H_{coh} = \frac{1}{2}(\Delta H_A^o + \Delta H_B^o) + \Delta H_m$,[2] where ΔH_A^o and ΔH_B^o are the cohesive energies of the corresponding solids A and B, obtained from C. Kittel, *Introduction to Solid State Physics*, 5th ed. (Wiley, NY, 1976), and from *Selected Values of the Thermodynamical Properties of the Elements*, edited by R. Hultgren, P. D. Desai, D. T. Hawkins, M. Gleiser, and K. K. K. Kelley (ASMT, Metal Parks, Ohio, 1973).

[c] Average energy deposited per unit length due to nuclear collision at the interface of A and B, J. P. Biersach and J. F. Ziegler, in *Ion Implantation Techniques*, edited by H. Ryssel and H. Glawisching (Springer-Verlag, Berlin, 1982).

[d] Average atomic density for $A_{50}B_{50}$ obtained from averaging the atomic densities of the pure elements A and B.

[e] Experimentally observed mixing rate $d(4Dt)/d\phi$.

[f] Calculated mixing rate $d(4Dt)/d\phi$ using Eq. (4.44) with the least-squares fitted values $K_1 = 0.034$ Å and $K_2 = 27$.

was designed to be 90% of the projected range of 600 keV Xe^{++} ions. A 30 Å layer of Ti was deposited on the SiO_2 substrate before deposition of the bottom layer to improve adhesion.

Ion mixing was performed with the samples at liquid nitrogen temperature in order to minimize the possible effects of radiation-enhanced diffusion. The pressure during irradiation was maintained below 5×10^{-7} Torr. The samples were irradiated with 600 keV Xe^{++} ions to doses of 10^{15}, 3×10^{15}, 5×10^{15}, and 7×10^{15} ions/cm^2, at a flux of about 200 nA/cm^2. At each dose, samples of all bilayers were irradiated simultaneously to remove possible variations in dose and dose rate.

After ion mixing, the samples were analyzed by means of 2 MeV He^+ backscattering with sample normals tilted 50° away from the incident beam direction. Two series of samples, Hf-Pd and Pt-Zr, exhibited enough mixing so that analysis with 3 MeV He^{++} ions and a target tilt of 50° was necessary in order to resolve top and bottom layer signals. The high-energy edge of the bottom layer signal of each spectrum was numerically transformed from counts versus energy to concentration versus depth (see Chapter 2 and Appendix 1). The transformed profiles were least-squares fitted to complementary error functions with four adjustable parameters (see Eq. (2.1)). The spreading of the mixed interface $(4Dt)^{1/2}$ was obtained from this procedure. A linear relationship between $4Dt$ and ion dose ϕ, similar to those in Fig. 2.2, is again observed. The slope of each line $d(4Dt)/d\phi$, deduced from a linear least-squares fit, characterizes the rate of ion mixing for the corresponding bilayer.

The observed variation in mixing rates $d(4Dt)/d\phi$ between systems cannot be explained by differences in collisional properties. A purely ballistic model, such as that given by Sigmund (Eq. (1.1)), predicts a variation in mixing rates of less than

35% over the entire range of systems, while the actual values vary by more than a factor of 5. However, there is a good correlation between the mixing rate and the heat of mixing as seen in Table 5.1. Furthermore, there is close agreement between the experimentally observed mixing rates $[d(4Dt)/d\phi]_{exp}$ and the phenomenological model predicted ones $[d(4Dt)/d\phi]_{calc}$ (see Table 5.1). The values for $[d(4Dt)/d\phi]_{calc}$ in Table 5.1 are calculated from Eq. (4.44) with the newly determined values $K_1 = 0.034$Å and $K_2 = 27$. This set of K_1 and K_2 is obtained from a least-squares fit to all the $5d - 4d$ bilayers listed in Table 5.1. This new set of parameters is very close to the previously determined K_1 and K_2 (see Chapter 4), suggesting that the phenomenological model of ion mixing developed in the earlier chapters is valid for the present case. Details of this set of experiments can be found in Ref. 5.

5.3 Summary of Results of Ion Mixing of Metallic Bilayers

In order to further compare the experimental results with the model, Eq. (4.44) is transformed to the form

$$\frac{d(4Dt)}{d\phi}\frac{\rho^{5/3}(\Delta H_{coh})^2}{\epsilon^2} = K_1 + K_1 K_2 \left(\frac{\Delta H_m}{\Delta H_{coh}}\right). \tag{5.1}$$

In Fig. 5.1, the left-hand side of Eq. (5.1) is plotted versus $\Delta H_m/\Delta H_{coh}$. All twenty-one observations of ion mixing of metallic bilayers using 600 keV Xe^{++}, described in this chapter and in the previous chapters, are included in Fig. 5.1. The values $K_1 = .035$ Å and $K_2 = 27.4$ are obtained from a least-squares fitting procedure applied to all the data in Fig. 5.1 except to those of Au-Ag and Hf-Ag which show marked deviations from the line in Fig. 5.1. Nevertheless, the degree to which so many ion mixing results can be approximately fitted by a single two-parameter function (Eq. (4.44)) is remarkable.

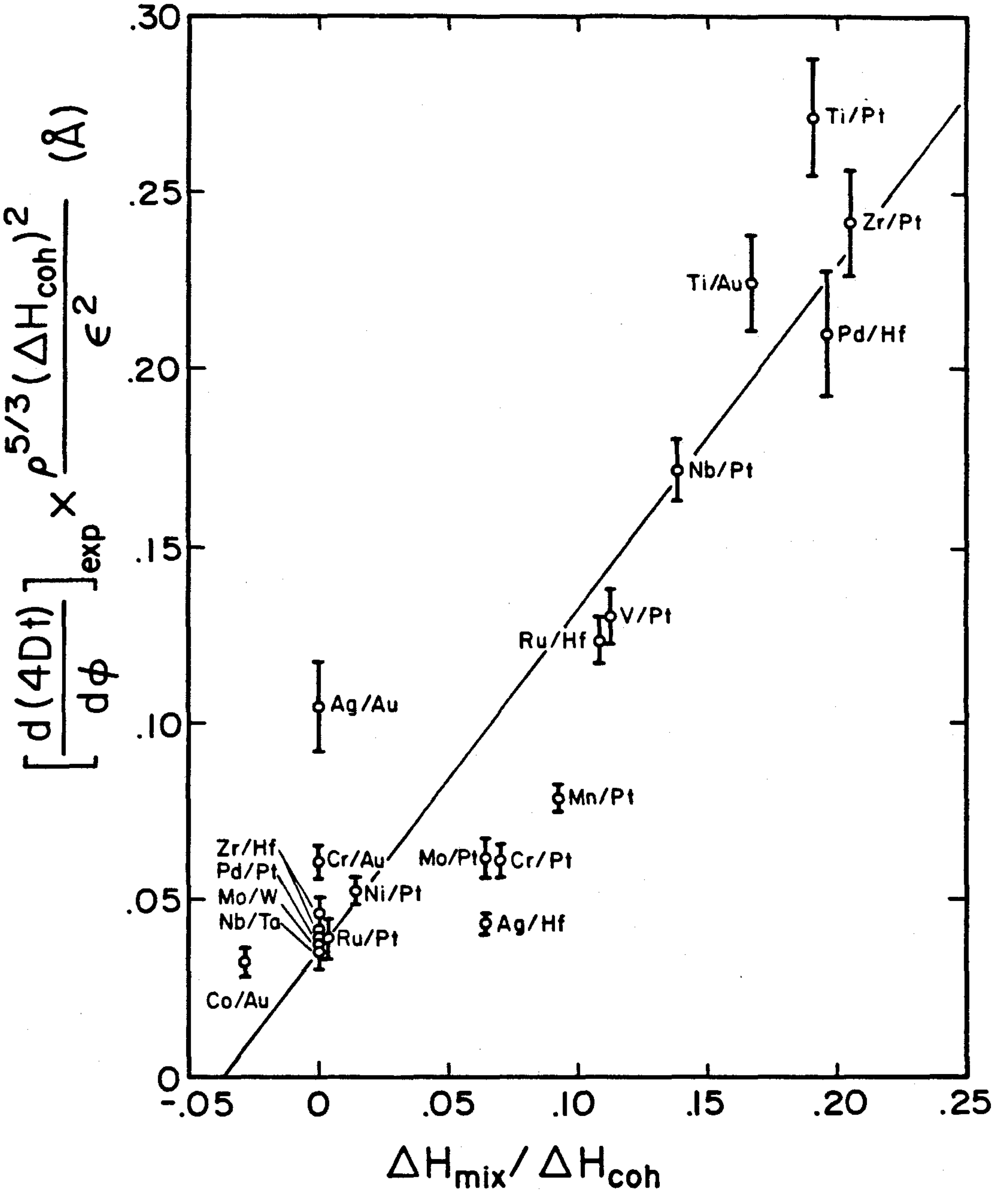

Fig. 5.1 Summary of results of ion mixing of metallic bilayers.

5.4 The Activation Energy of Diffusion in the Late Stages of Dense Collisional Cascades

In the derivation of Eq. (4.44), it was shown that $K_2 = 4/s_2$, where s_2 is a constant in the scaling relation $Q = -s_2 \Delta H_{coh}$ of the apparent activation energy of diffusion Q with the cohesive energy of the matrix ΔH_{coh}. Using the newly determined value $K_2 = 27.4$, we obtain the value $s_2 = 0.14$; i.e.,

$$Q = -0.14 \Delta H_{coh}. \tag{5.2}$$

This scaling relationship between the cohesive energy and the apparent activation energy for diffusion in collisional cascades is compared with a similar relationship for vacancy thermal diffusion in the following paragraph.

It has been known for a long time that simple scaling relationships exit between various energy scales for vacancy thermal diffusion in metals.[6,7,8] Seitz[6] suggested that the formation energy of a vacancy E_v^f is about one-half of the activation energy for self diffusion Q_v. Simmons and Balluffi[7] showed that

$$E_v^f \approx 0.55 Q_v. \tag{5.3}$$

Doyama and Koehler[8] demonstrated that Eq. (5.3) holds for seventeen different metals for which experimentally determined values of E_v^f and Q_v were available. In addition, they have shown that E_v^f scales with ΔH_{coh}, the cohesive energy of the matrix. According to Ref. 8,

$$E_v^f = -0.29 \Delta H_{coh}. \tag{5.4}$$

Eqs. (5.3) and (5.4) lead to

$$Q_v = -0.53 \Delta H_{coh}. \tag{5.5}$$

Table 5.2 Comparison between the activation energies obtained from scaling laws for thermal vacancy diffusion and for diffusion in dense collisional cascades.

System	Au	Ni	Ti	Hf	Nb	W
-ΔH_{coh} (eV)	3.81	4.44	4.85	6.44	7.57	8.90
Q (eV)	0.53	0.62	0.67	0.90	1.06	1.24
Q_v (eV)	2.02	2.35	2.57	3.41	4.01	4.72

Thus, the activation energy of vacancy thermal diffusion scales with the cohesive energy of the corresponding solid. Eq. (5.5) has the same form as Eq. (5.2), except that the constant of proportionality between the activation energy and the cohesive energy is smaller for dense collisional cascades (Eq. (5.2)) than for vacancy thermal diffusion (Eq. (5.5)). Q and Q_v, calculated using Eqs. (5.2) and (5.5), are listed in Table 5.2 for several representative systems. Q is between 0.6 to 1.3 eV and is 26.6% of Q_v. The smaller activation energy Q must relate to the nature of the atomic jumps in a dense collisional cascade. The phenomenological model, based on general principles from thermodynamics, is not expected to explain the details of atomic jumps. It does, however, indicate a change in the mechanism for diffusion in a high temperature and, possibly, high pressure medium such as in a dense collisional cascade.

5.5 Beyond the Phenomenological Model

So far, experiments have strongly supported the phenomenological model of ion mixing (Eq. (4.44)) as seen in the previous discussions. Thus, we have shown that the chemical driving forces such as the heat of mixing of binary alloys and the thermal spike effect both play important roles in energetic-heavy-ion induced atomic transport in solids consisting of heavy elements. However, the limitations of this model remain to be established. For example, it is known that there is no spike effect in the case of light-ion (e.g., electron and alpha particle) irradiation. The criteria for when the chemical effect and/or the spike effect become important are still unclear. Even in those cases where the spike effect is important, the understanding of how an initial cascade evolves into a spike is still poor. In the next chapter, we attempt to address this question using a fractal geometry approach.

The indication of a decreased activation energy of diffusion during the late stage of dense collisional cascades (see Section 5.4) offers new challenges for an understanding of the fundamental aspects of ion-solid interactions. This phenomenon is most likely related to the behavior of materials under extremely high temperatures and pressures. Computer simulations will be an invaluable tool in studying such problems. The change of the activation energy for diffusion should also provide a warning against the practice of extrapolating physical parameters from their normal usage to the spike regime. In contrast, the use of scaling arguments offers some advantage.

The study of ion mixing of systems with extremely large positive or negative heats of mixing is also important. In the large, negative heat of mixing case, the heat released upon mixing may be so large as to induce significant additional local heating and mixing. In the large, positive heat of mixing case, the sign change of the effective diffusion coefficient with temperature and composition may cause a complicated interplay of mixing and demixing.

It is the present author's sincere belief that studies of the problems mentioned above will be even more exciting and will further enhance our understanding of ion-solid interactions.

5.6 References

1. A. R. Miedema, Philips Tech. Rev. **36**, 217 (1976).
2. C. Kittel, *Introduction to Solid State Physics*, 5th edition (Wiley, New York, 1976).
3. H. H. Anderson, Appl. Phys. **18**, 131 (1979).
4. J. P. Biersach and J. F. Ziegler, in *Ion Implantation Techniques*, edited by H. Ryssel and H. Glawisching (Springer-Verlag, Berlin, 1982), p. 122.
5. T. W. Workman, Y.-T. Cheng, W. L. Johnson, and M-A. Nicolet, submitted to Appl. Phys. Lett.
6. F. Seitz, Adv. Phys. **1**, 42 (1952).
7. R. O. Simmons and R. W. Balluffi, Phys. Rev. **129**, 1533 (1963).
8. M. Doyama and J. S. Koehler, Acta Metall. **24**, 871 (1976).

Chapter 6

FROM CASCADE to SPIKE - A FRACTAL GEOMETRY APPROACH

6.1 Introduction

In the previous chapters, we have seen convincing evidence that thermodynamics plays an important role in ion mixing: the thermal spike idea and the mechanism of chemically biased diffusion comprise the backbone of our phenomenological description of high-energy, heavy-ion-induced atomic mixing in metals. The good agreement between the model and the experimental observations further emphasizes the need for a better understanding of what a spike is, especially, how a cascade evolves into a spike.

In the following, we shall show that the notion of *fractal* dimensionality, introduced by Mandelbrot,[1] provides a natural framework for studying the problem at hand. The idea of fractal dimensions has had an impact on a series of problems ranging from coastline geometry to disordered materials, to galaxy formation.[1-4] In Section 6.2 we discuss two well-known examples of fractals, the Koch curve and the tree branching problem. In Section 6.3 we examine the fractal nature of collisional cascades. We shall assume elastic scattering with an inverse-power potential,[5,6] $V(r) \propto r^{-1/m}$, where r is the internuclear distance and $0 \leq m < 1$. The "Hard-sphere" collision approximation[7] will be used to construct an idealized collisional cascade in order to obtain analytical results and to incorporate the concept of fractals. As shall be seen, fractal dimensionality leads to a precise definition of spikes. Furthermore, it offers a means to trace the evolution from cascade to spike. Implications of this study will be discussed in Section 6.4.

6.2 Examples of Fractals

Before going into the definition of fractals, let us first examine Richardson's coastline problem. Richardson discovered that the length of a coastline L, measured by a yardstick of length ϵ, tends to diverge as ϵ decreases according to the relationship

$$L(\epsilon) \sim F\epsilon^{1-D}, \tag{6.1}$$

where F and $D > 1$ are constants for each coastline. The Richardson effect, contrary to what one might expect – that $L(\epsilon)$ approaches a finite "true" value as ϵ approaches zero – is due to the fact that as ϵ decreases, more and more of the details can be measured and each adds to the measured coastline length.

Mandelbrot has shown that D, though not an integer, can be identified as a dimension, the *fractal* dimension. For systems with self-similarity, the fractal dimension is identical to the similarity dimension[1] (defined next).

A variety of shapes, whether creations of Nature or of the imagination, contains a self-similarity. Examples include intervals in the line, rectangles in the plane, and the like. In each case, the "whole" may be "paved" by N "parts" and each part is identical to the whole when all the length scales of the whole are reduced by a factor γ. This ratio γ is called the similarity ratio. If a line segment is taken as a whole, it can be paved by N smaller line segments, each of which is obtained from the whole line segment by a similarity ratio $\gamma(N) = 1/N^1$, because the Euclidean dimension of a straight line is 1. Likewise, since the Euclidean dimension of a plane is 2, the "whole" rectangle $0 \leq x < X$; $0 \leq y < Y$ can be "paved" exactly by $N = b^2$ parts. These parts are rectangles defined by $(k-1)X/b \leq x < kX/b$ and $(h-1)Y/b \leq y < hY/b$, where k and h go from 1 to b. Here, each part can now be deduced from the whole by a similarity ratio $\gamma(N) = 1/N^{1/2}$.

In general, for spaces with Euclidean dimension E, a "whole" polyhedron of dimension $D \leq E$ may be "paved" by N "parts." Each part is obtained by a similarity ratio

$$\gamma(N) = 1/N^{1/D}, \tag{6.2}$$

or equivalently,

$$D = -\ln N / \ln \gamma(N). \tag{6.3}$$

The exponent D in Eqs. (6.2) and (6.3) is the self-similarity dimension of the corresponding self-similar geometric object. D is not restricted to integers. In order for the self-similarity dimension to be meaningful, the only requirement is that the shape be self-similar, i.e., that the whole may be split up into N parts and that each part is obtainable from the whole by a similarity of ratio γ (followed by displacement or by symmetry). To illustrate this, let us consider a triadic Koch curve (see Fig. 6.1). We assume that initially we have a straight line of length 1, to be called the *initiator*. We divide it into 3 pieces each of which is 1/3 of the original length, and we replace the middle third by an equilateral triangle. The resulting curve is a line formed of four intervals of equal lengths, to be called the *generator*. We can further replace each of the generator's four intervals by a generator whose size is reduced by a factor of one-third; the resulting curve is shown in Fig. 6.1. Proceeding in this fashion, we see that each straight line can be decomposed into reduced-size pieces. We have $N = 4$ and $\gamma = 1/3$, resulting in an increasingly broken curve of a self-similarity dimension, $D = \ln N / \ln(1/\gamma) \sim 1.2618$.

The next example, taken from Mandelbrot's book, *The Fractal Geometry of Nature*,[1] concerns trees, or in general, branching processes (Fig. 6.2). The trees in

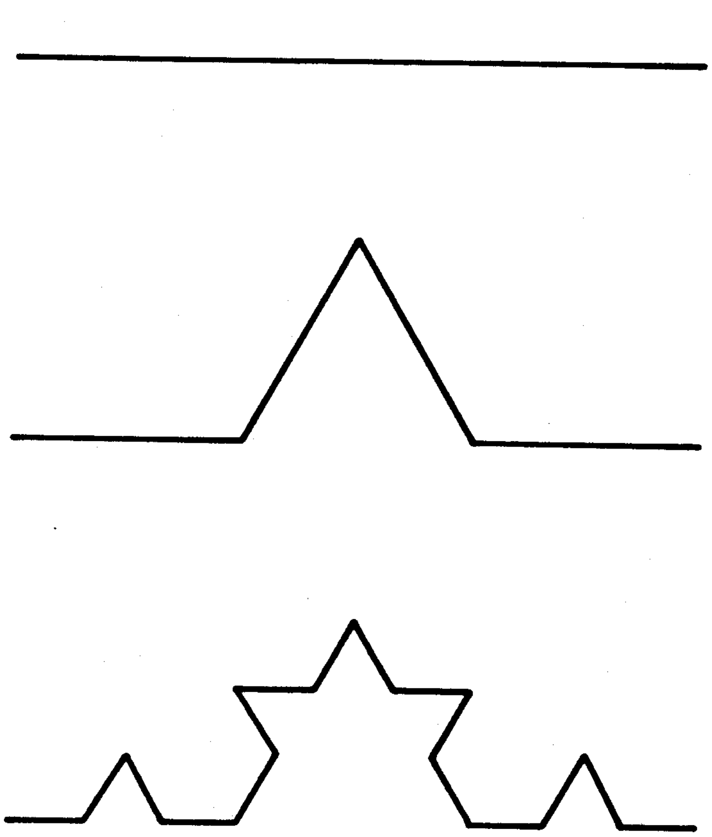

Fig. 6.1 The first three steps in constructing the triadic Koch curve ($D = \ln 4/\ln 3 \cong 1.26$).

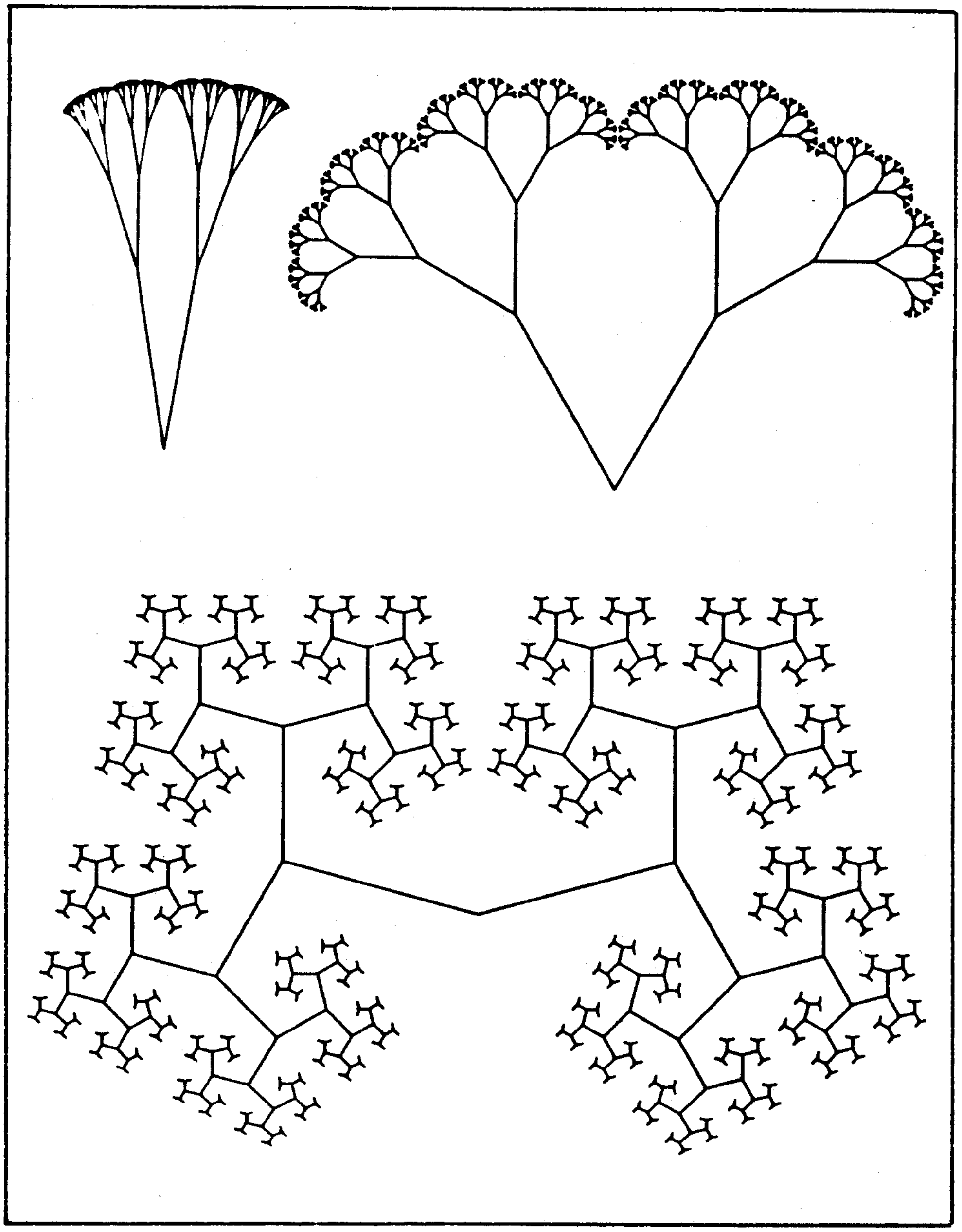

Fig. 6.2 Examples of trees from Mandelbrot's book, *The Fractal Geometry of Nature.* [1] The fractal dimensionality, measured by the present author, is about 1.06, 1.17, and 1.63, respectively, in the clockwise direction beginning from the upper left corner.

Fig. 6.2 have infinitely thin stems and the same angle θ between the branches at every branching point. Each of the trees is a self-similar geometric object because it is constructed in such a way that the length ratio $0 < \gamma < 1$ between the successive branches is fixed throughout. Since $N = 2$, the fractal dimension D is equal to $\ln 2/\ln(1/\gamma)$, according to Eq. (6.3). In Fig. 6.2, D has values between 1 and 2. Mandelbrot described these trees in Fig. 6.2 as follows,[1] "For D barely larger than 1 (top left), the result is whisk-like, then broom-like. As D increases, the branches open up, and the outline or 'canopy' extends into folds hidden from the sunshine...." For larger D (bottom), " A Frenchman is reminded of the fortifications by Vauban. The values $D = 2$ and $\theta = \pi$ yields a plane-filling tree...." This kind of "plane-filling" or "space-filling" property is common for fractals if the fractal dimension reaches the Euclidean dimension of the space in which they are embedded.[1]

6.3 Collisional Cascades and Fractals

A natural connection between a tree and a collisional cascade is established if each branching point of a tree is taken to represent a binary collision event, and each branch corresponds to a mean free path between collisions.

Real collisional cascades, as well as computer generated ones[8] (see Fig. 6.3), are less regular than the trees in Fig. 6.2. The tree has a single branching angle, and the length of every branch is determined by its generation; in a collisional cascade, the scattering angle and the distance traveled between collisions may be considered stochastic. Useful information about cascades can be obtained from statistical averages, whether taken over actual collisional cascades or over computer-simulated ones. It is, therefore, instructive to construct a cascade in which the scattering angle and the distance traveled between collisions at each generation

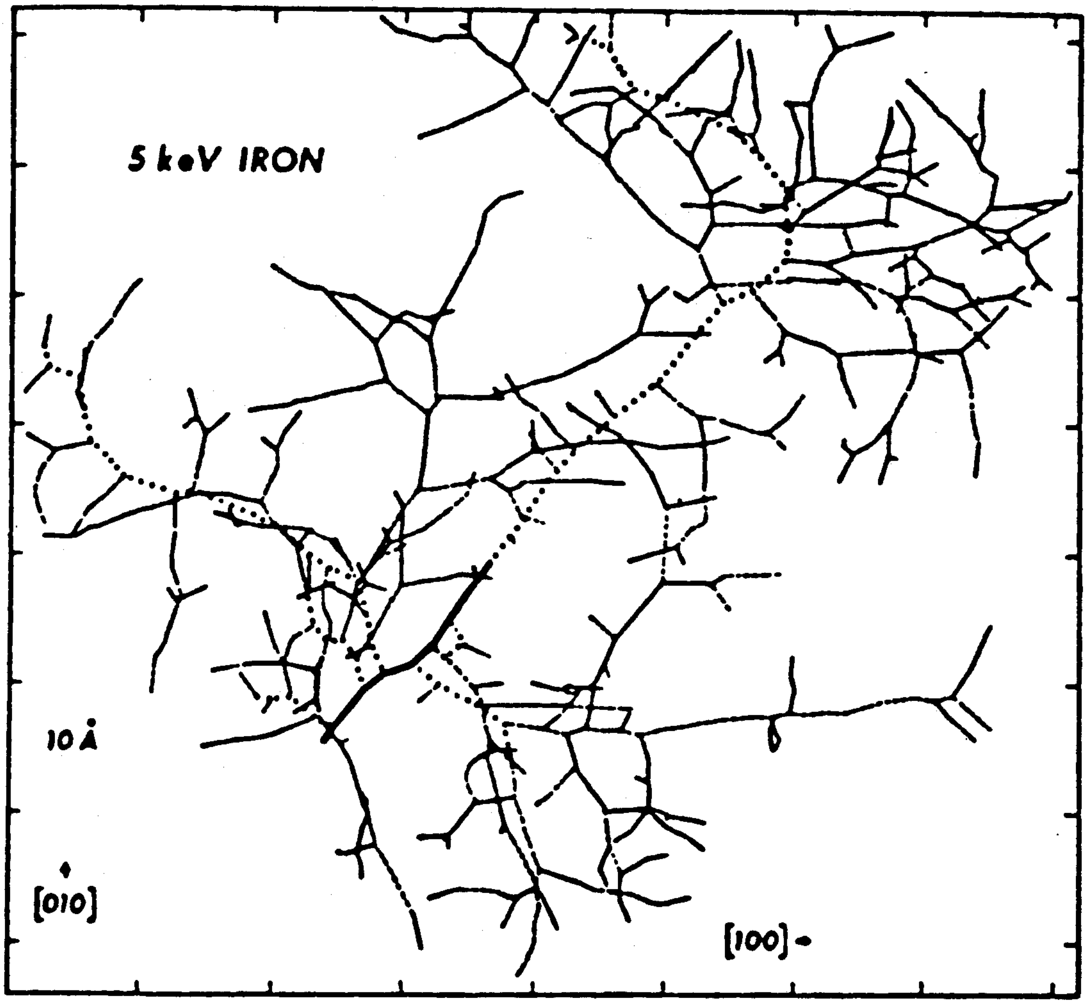

Fig. 6.3 Computer simulation of trajectories in a collisional cascade in α-iron. The cascade was initiated by a 5-keV primary knock-on atom ejected from the lower end of the heavy, solid trajectory (Ref. 8)

take their average values. This model of an idealized collisional cascade, though lacking randomness, contains essential features of a real collisional cascade and lends itself readily to analysis in terms of fractals. The idealization of cascades is in the same spirit as Mandelbrot's treatment of the coastline problem in which an irregular coastline is first approximated by a Koch curve.[1]

In collisions with large scattering angle and large momentum and energy transfer, which are considered to be most effective in inducing the transition from cascade to thermal-spike behavior, the hard-sphere collision approximation is often applicable.[7] Consider a system made of identical particles. At each energy considered, the radius of the particles is defined as half the distance of closest possible approach ρ_o, when the impact parameter for binary collisions is 0 and the scattering angle ϕ in the Center of Mass System (C) is π. For that case, the potential energy at ρ_o is given by[7]

$$V(\rho_o) = \frac{1}{2}E_0, \tag{6.4}$$

where E_0 is the incident particle kinetic energy in the Laboratory Coordinate System (L). Eq. (6.4) defines ρ_o. Following the derivation in Ref. (7), the differential and total cross-sections are given by

$$d\sigma = \pi\rho_o^2 dE_1/E_0, \tag{6.5a}$$

and

$$\sigma = \pi\rho_o^2, \tag{6.5b}$$

where E_1 is the kinetic energy of the recoil particle in L-coordinates. The mean recoil energy $\overline{E_1}$ is given by $\overline{E_1} = \frac{1}{2}\overline{E_0}$. We can generalize this result to the nth generation of collisions; i.e.

$$\overline{E_n} = \frac{1}{2}\overline{E_{n-1}}. \tag{6.6}$$

From Eq. (6.6), we obtain the average scattering angle in C-coordinates, $\overline{\phi} = \frac{\pi}{2}$. In L-coordinates, the average scattering angle becomes $\theta_1 = \theta_2 = \frac{\pi}{4}$ (see Fig. 6.4).

While the length ratio of the stems in every tree in Fig. 6.2 is chosen for aesthetic reasons, the ideal collisional cascades, to be constructed next, have definite mean free path ratios. The mean free path of the n^{th} generation is given by $\lambda_n = 1/N\sigma_n$, where N is the atomic density. For inverse-power potentials, $V(r) = Gr^{-1/m}$, with G a constant which depends on m, and $0 \leq m < 1$, the total cross-section σ_n equals $\pi(2G/\overline{E_n})^{2m}$, according to Eqs. (6.4) and (6.5b). We obtain

$$\begin{aligned}\lambda_n &= \frac{1}{N\pi}\Big(\frac{\overline{E_n}}{2G}\Big)^{2m} \\ &= \Big(\frac{1}{2}\Big)^{2m}\frac{1}{N\pi}\Big(\frac{\overline{E_{n-1}}}{2G}\Big)^{2m} \\ &= \Big(\frac{1}{2}\Big)^{2m}\lambda_{n-1},\end{aligned} \tag{6.7}$$

where we have used Eq. (6.6). The mean free path ratio, $\gamma = \lambda_n/\lambda_{n-1} = 2^{-2m}$, is independent of n, the generation of the cascade. The collisional cascade, generated by $\gamma = 2^{-2m}$ and the mean scattering angle $\theta = \frac{\pi}{4}$, is therefore self-similar and has a fractal dimension

$$D = \frac{\ln 2}{\ln 1/\gamma} = \frac{1}{2m}. \tag{6.8}$$

Thus, the fractal dimension of a cascade depends *explicitly* on the type of interatomic potential encountered. For the inverse-square potential, $m = 1/2$, we have a cascade of dimension 1. For inverse-power potentials with $m = 1/6$, we have a cascade of fractal dimension 3, which equals the physical dimension of the space in which an actual collisional cascade is embedded. For $1/2 < m \leq 1$, $1 > D \geq 1/2$ from Eq. (6.8). This is the case of "subfractal trees"[1] and D is then necessarily 1 which is the topological dimension of a branching tree (see Ref. 1, pp. 152-153).

In particular, $D = 1$ for Rutherford scattering ($m = 1$). As examples, idealized collisional cascades for $V(r) \propto r^{-2}$ and $V(r) \propto r^{-4}$ are those trees shown in Fig. 6.4.

As an actual collisional cascade evolves in time, the characteristic kinetic energy of atoms or ions changes from the primary incident ion energy, which is typically on the order of several hundred keV in most ion mixing or ion implantation experiments, to the eV energy range. The inverse-power potentials $V(r) \propto r^{-1/m}$, with $0 \leq m < 1$, have been frequently utilized.[5-7] For example, it has been argued that over a major portion of the keV range and for medium to heavy-mass ions and atoms, the inverse-square potential (i.e., $m = 1/2$) is a fair approximation, while in the lower-keV and the upper-eV region, $m = 1/3$ should be adequate.[5,6] In the eV region, m may be taken close to zero.[5,6] To describe an actual collisional cascade from beginning to end by the inverse-power potential, decreasing values of $0 \leq m < 1/2$ must be used. The actual cascade is, therefore, not a fractal in the sense that has been given so far, but is a *nonuniform* fractal[1] with a variable dimensionality that increases from its initial dimensionality 1 (i.e., $m = 1/2$).

Conclusion 1: In a collisional cascade, the fractal dimensionality increases as the cascade evolves due to the change of the interaction potential.

6.4 Fractals and Spikes

The "spike" is, as has been frequently stated, "a *limited volume* with the *majority* of atoms temporarily in motion."[9] This spike condition is far from quantitative because the terms "limited volume" and "majority" cannot be uniquely defined (see Fig. 6.3). Thus, the density of moving particles cannot be defined without further assumptions. To circumvent these difficulties, we propose an alternative approach to

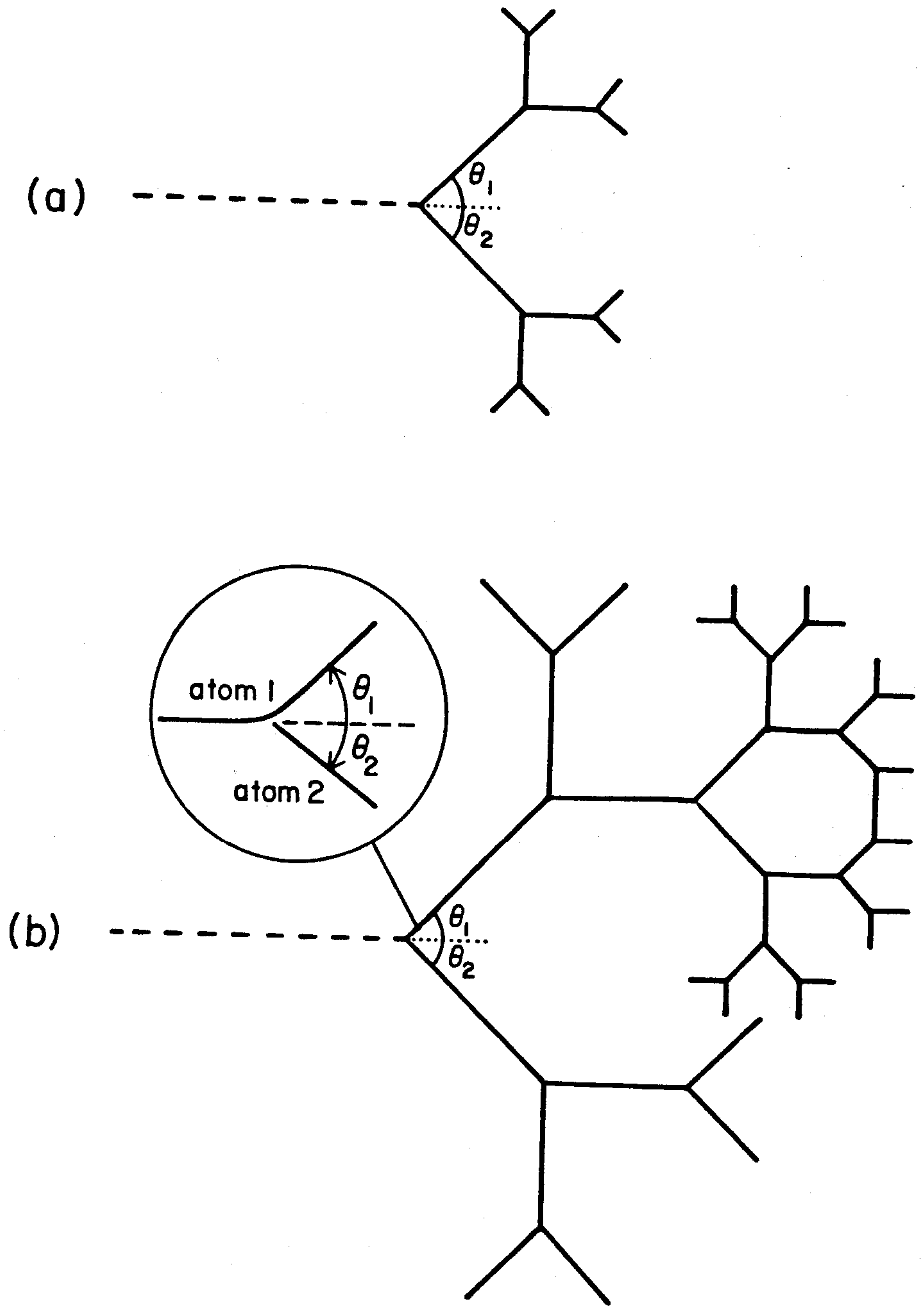

Fig. 6.4 Idealized cascades, as discussed in the text, for (a) $V(r) \propto r^{-2}$ with $D = 1$, and (b) $V(r) \propto r^{-4}$ with $D = 2$. The cascades must be terminated in the two cases when the mean free path approaches the same predetermined shortest length scale. In $D = 2$ case (b), only one section of the "plane-filling" cascade is shown.

the spike condition by applying a well-defined concept of "space-filling" fractals:[1] A fractal is "space-filling" when its fractal dimension D equals the physical dimension E of the space in which it is embedded.

This "space-filling" condition is illustrated in the following for the case of idealized collisional cascades. We first identify the shortest length scale to be the shortest mean free path λ_g and equate this to the interatomic spacing a; i.e., $\lambda_g = a$. Likewise, we take the longest length scale to be the longest mean free path λ_o. Within the framework of the idealized collisional cascades, λ_o can take any value greater than λ_g. For an idealized collisional cascade of dimension $D = \ln 2/(\ln 1/\gamma)$, the total number of generations of cascades required to reduce the mean free path from λ_o to λ_g is given by

$$g = \frac{\ln(\lambda_g/\lambda_o)}{\ln\gamma}, \tag{6.9}$$

and the total number of displaced atoms N_c is given by

$$N_c = 2^g = \left(\frac{\lambda_o}{\lambda_g}\right)^D . \tag{6.10}$$

An *upper-bound* for the linear dimension of the cascade L can be obtained by summing up the series $\sum_{i=0}^{g} \lambda_i \leq \sum_{i=0}^{\infty} \lambda_i = \lambda_o/(1-\gamma)$; thus, $L = \lambda_o/(1-\gamma)$. Let us suppose that the cascade is embedded in a physical space of dimension E, then the total number of lattice points N_a included in the "cascade-influenced volume" defined by an E-dimensional sphere of radius L can be calculated. We find

$$N_a = \left(\frac{L}{\lambda_g}\right)^E = \left(\frac{\lambda_o}{\lambda_g}\right)^E \left[\frac{1}{1-\gamma}\right]^E . \tag{6.11}$$

The ratio $\eta = N_c/N_a$ between the total number of the displaced atoms and the total number lattice atoms in the "cascade-influenced volume" can be calculated using Eqs. (6.10) and (6.11). In the limit of $\lambda_o \to \infty$, this ratio becomes

$$\eta = \lim_{\lambda_o \to \infty} \left(\frac{\lambda_o}{\lambda_g}\right)^{D-E} \left[1 - 2^{-1/D}\right]^E = \begin{cases} \infty, & \text{if } D \geq E; \\ 0, & \text{if } D < E. \end{cases} \tag{6.12}$$

Thus, $D = E$ is a critical dimension for "space-filling".

For cascades in 3-dimensional space, it is therefore appropriate to postulate that a transition from cascade to spike occurs when the fractal dimension of a collisional cascade D equals 3. The condition $D = 3$ implies that $m = 1/6$ (see Eq. (6.8)). This corresponds to a potential $V(r) \propto r^{-6}$, which is, according to previous discussions, applicable to particles of a characteristic kinetic energy in the "upper-eV" to eV range.[5,6]

Conclusion 2: If a spike occurs, the characteristic kinetic energy of the moving particles must be on the order of a few eV.

The postulate that $D = 3$ specifies when a spike will occur, but that situation may not necessarily arise in reality. Two possible scenarios may prevent $D = 3$ from occurring. In real systems, if the minimum energy to displace an atom is much more than a few eV, then the cascades may stop prematurely before reaching $D = 3$. Alternatively, if the situation is such that for a mean free path on the order of one atomic spacing the potential is still with an inverse power $m > 1/6$, then a spike will also not occur. The physical conditions under which the fractal dimension D of a cascade will reach the critical value of 3 offers a new and promising field for further theoretical and experimental investigations.

Recently, there have been reports that spikes indeed occur at an energy level of an eV per particle.[10-12] In ion mixing experiments,[10] described in Chapter 2, it was shown that thermal spike effects, such as the chemically biased diffusion due to the heat of mixing of a binary alloy, occur at a characteristic kinetic energy level of about an eV per particle. From another experiment where the temperature evolution of a copper bar during high-energy Xe^+ bombardment was recorded, a temperature of 8.6×10^4 K was deduced for the initial spike region.[11] This temperature corresponds to a kinetic energy of about 11 eV/particle if atoms involved in a spike are modeled as ideal gas and the equipartition theorem takes the form $E = 3/2kT$, where k is the Boltzmann constant. In a computer simulation it was observed that equipartition of kinetic and potential energy of moving particles occurs in about the eV per particle range, thus indicating the approach to thermal equilibrium within the cascade at this characteristic energy.[12] These findings are consistent with the above conclusion 2.

6.5 Summary

By considering idealized cascades for various inverse-power potentials, we conclude that in actual collisional cascades the fractal dimensionality of branching increases as the cascade evolves. This increase is due to the change of the interaction potential with energy. We also predict the order of magnitude of the kinetic energy of particles in an actual spike based on the assumption that a spike occurs when the fractal dimension of the cascade equals the physical dimension of the solid. The ideas contained in this chapter also apply to other scattering problems for which inverse-power potentials are applicable.

Added Notes: The present author observed that the fractal nature of collisional cascades is *inherent* in the traditional theory of collisional cascade developed by Winterbon, Sigmund, and Sanders in the late 1960s. This new observation is presented in Appendix 2. It further supports the conclusions drawn in this chapter.

6.6 References

1. B. B. Mandelbrot, *The Fractal Geometry of Nature* (W. H. Freeman and Company, New York, 1983).
2. *Kinetics of Aggregation and Gelation*, edited by F. Family and D. P. Landau (North-Holland, Amsterdam 1984).
3. S. H. Liu, Solid State Physics, Vol. 39, 207 (1986).
4. *On Growth and Form*, edited by H. E. Stanley and N. Ostrowsky (Martinus Nijhoff, Boston, 1986).
5. J. Lindhard, V. Nielsen, and M. Scharff, Kgl. Danske Videnskab. Selskab Mat.-Fys. Medd. **36**, 10 (1968).
6. P. Sigmund, Phys. Rev. **184**, 383 (1969).
7. M. W. Thompson, *Defects and Radiation Damage in Metals* (Cambridge University Press, London, New York, 1969).
8. J. R. Beeler, Jr., Phys. Rev. **150**, 470 (1966).
9. P. Sigmund, Appl. Phys. Lett. **25**, 169 (1974).
10. Y.-T. Cheng, M. Van Rossum, M-A. Nicolet, and W. L. Johnson, Appl. Phys. Lett. **45**, 185 (1984).
11. L. M. Gratton, A. Miotello, and C. Tosello, Appl. Phys. **A 36**, 139 (1985).
12. W. E. King and R. Benedek, J. Nucl. Materials **117**, 26 (1983).

Chapter 7

CORRELATION BETWEEN THE COHESIVE ENERGY AND THE ONSET OF RADIATION-ENHANCED DIFFUSION IN ION MIXING

7.1 Introduction

As stated in Chapter 1, there are two separate regimes, each having different mechanisms that are responsible for the observed ion mixing phenomena. In the early chapters, various effects operating in the prompt regime have been examined in detail. In this chapter, the transition from the "prompt" to the "delayed" regime is studied. This transition is, as was seen in Chapter 1, characterized by a critical ambient temperature T_c. Below T_c, cascade mixing[1] and thermal spike effects[2] dominate and the mixing rate is independent of the ambient temperature. Above T_c, radiation-enhanced diffusion plays a dominant role,[3] and the mixing rate has an Arrhenius-type temperature dependence. A narrow temperature range, separating the temperature-independent, or low-temperature, ion mixing region from the Arrhenius-type radiation-enhanced diffusion region, serves as a basis for defining the critical temperature T_c (see Fig. 1.1). In this chapter, we establish a correlation between T_c and the average cohesive energy of elemental solids which are mixed. This correlation thus enables one to predict the onset of radiation-enhanced diffusion (T_c) for systems that have not yet been investigated.

7.2 Experimental Evidence of the Correlation

The systems we have studied are W-Mo, Ta-Nb, and Pt-Pd bilayers. The metals used have relatively high cohesive energies,[4] but each binary couple has nearly zero heat of mixing.[5] Therefore, we are able to isolate the effect of cohesive energy from the possible influence of a chemical driving force on radiation-enhanced diffusion. Furthermore, all the $5d$ (and $4d$) elements have nearly the same atomic number and mass, while the mass difference between the top ($5d$) and bottom ($4d$) layer of each couple is sufficient to allow a large enough separation of their He^+ backscattering energy signals in order to study the intermixing process using backscattering spectrometry.[6]

Thin bilayer samples were prepared by electron-gun evaporation in an oil-free vacuum system at a pressure of less than 8×10^{-8} Torr during evaporation. All bilayers consisted of a layer of the $5d$ element on top of a $\sim$ 200-nm-thick layer of the $4d$ element sequentially deposited onto a SiO_2 substrate. The top layer thickness was adjusted to 90% of the projected range of 600-keV Xe^{++} ions. Ion mixing was performed to a dose of $5 \times 10^{15}/cm^2$, at substrate temperatures of 300, 520, 630, 720, and 800 K, the highest accessible temperature of our instrument. Samples of all three types were irradiated simultaneously at each specified temperature. Backscattering analysis was performed with 2-MeV He^+ ions incident at an angle of 30° against the sample normal.

The backscattering spectra were analyzed by a fitting routine described in Chapter 2 (and see Appendix 1).[7,8] Within the experimental resolution, there was no noticeable change in the amount of mixing for Ta-Nb and W-Mo bilayers, when the substrate temperature was varied from 300 to 800 K. This upper temperature thus represents the lower bound on T_c for the Ta-Nb and W-Mo systems. A substantial increase in the rate of mixing was detected in the Pt-Pd system as the temperature was varied from 520 to 630 K.

Additional data concerning the temperature dependence of ion mixing were obtained from the literature.[9-16] In Fig. 7.1 we plot T_c versus the average cohesive energy ΔH_{coh} for a variety of systems. ΔH_{coh} is the arithmetic average of the cohesive energies of the pure elements[4] in each binary system. T_c is defined by the intersection of the high- and low-temperature asymptotes or the temperature range, where a substantial increase in the rate of mixing was reported. The error bars in some cases were taken to be the temperature intervals of the experiment where radiation-enhanced diffusion was observed. The Ni-Si system exhibits a very wide transition from the low- to high-temperature region.[16] T_c is, therefore, not well defined and this system is not included in Fig. 7.1.

A correlation between T_c and ΔH_{coh}, as shown in Fig. 7.1, is apparent. The greater the average cohesive energy of the component layers ΔH_{coh}, the higher is the critical ambient temperature T_c where radiation-enhanced diffusion becomes dominant. Since data in Fig. 7.1 come from many sources and each ion mixing experiment was performed with different ion, energy, dose, and dose rate, we conclude that these parameters are of minor importance compared to the cohesive energy of the system irradiated. Furthermore, the relationship between T_c and ΔH_{coh} is roughly linear as shown in Fig. 7.1. All these features may be explained by the following argument.

7.3 Theoretical Understanding of the Correlation

Phenomenologically, we can describe the behavior of the amount of mixing versus $1/T$ by an effective diffusion coefficient of the form

$$D = D_c + D_r e^{-Q_r/kT}. \tag{7.1}$$

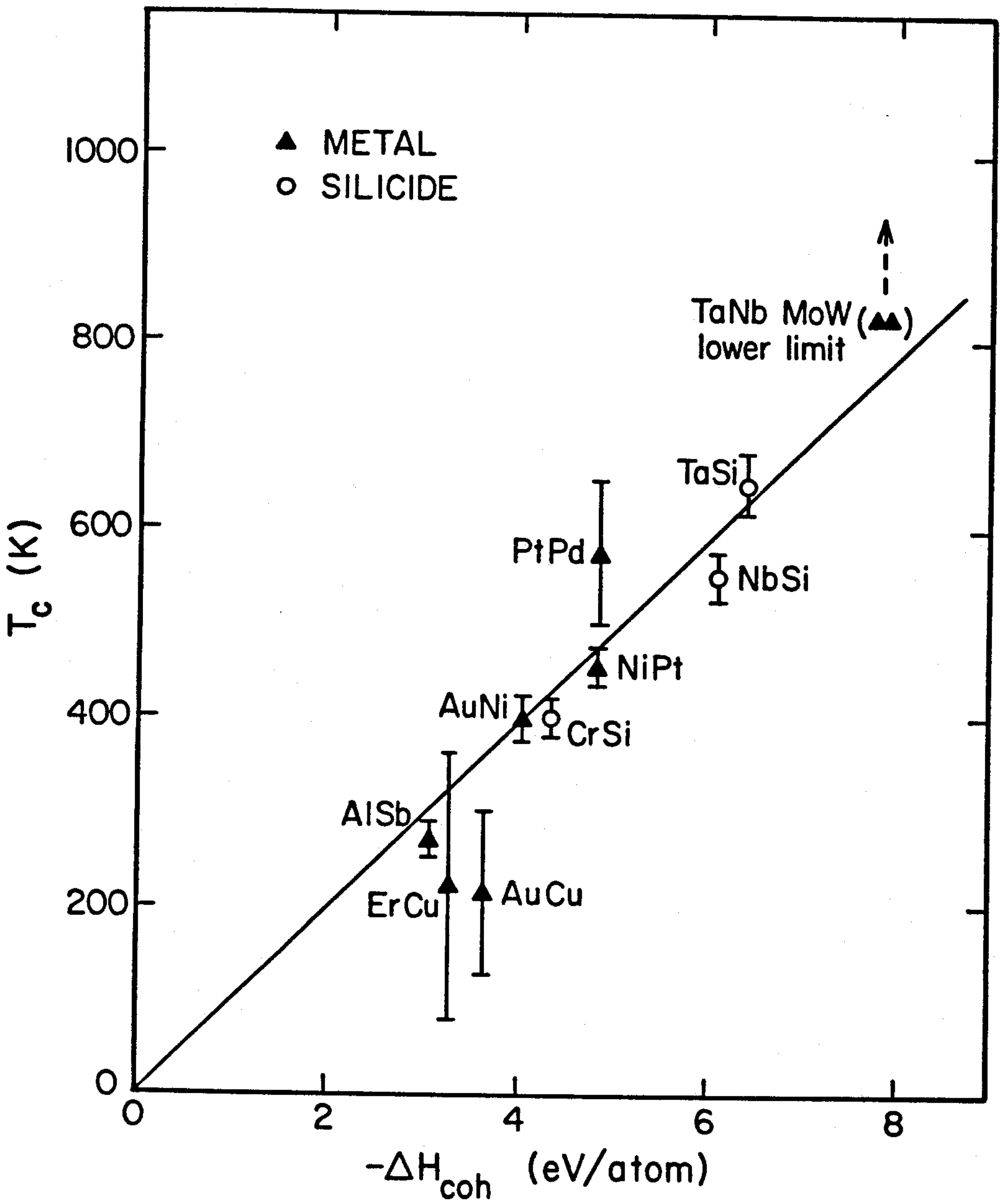

Fig. 7.1 Correlation between the average cohesive energy ΔH_{coh} and the critical temperature T_c at which radiation-enhanced diffusion becomes dominant. (TaSi;[9] NbSi;[10] NiPt;[11] AuNi;[11] CrSi;[12] AuCu;[13] AlSb;[14] ErCu.[15])

The first term on the right-hand side is temperature-independent and the second term has an Arrhenius-type temperature dependence, where Q_r is an apparent activation energy. The first term on the right derives from cascade mixing and dominates at low temperatures; the second term originates from radiation-enhanced diffusion and dominates at high temperatures.

At a temperature near T_c the two terms on the right of Eq. (7.1) contribute equally and

$$T_c = (1/k)\Big[\ln(D_r/D_c)\Big]^{-1} Q_r. \tag{7.2}$$

Now, let us assume that there is a scaling relationship between the apparent activation energy Q_r and the cohesive energy of the matrix ΔH_{coh}; i.e., $Q_r = -r\Delta H_{coh}$, where r is a positive constant. This type of scaling relationship is known to exist in vacancy thermal diffusion in elemental solids,[17,18] and we have seen that a similar scaling law holds in dense cascades (Chapters 4 and 5). We then have

$$T_c = (r/k)\Big[\ln(D_r/D_c)\Big]^{-1} \Delta H_{coh}. \tag{7.3}$$

In principle, D_c may be calculated using cascade mixing or thermal spike models,[2,3] and D_r can be obtained from radiation-enhanced diffusion models.[19,20] We estimated the logarithmic term $\ln(D_r/D_c)$ for several systems for which the necessary parameters were readily available. This estimation is summarized in Table 7.1 Despite the fact that the factor (D_r/D_c) varies by four orders of magnitude, the logarithmic term remains within 47% from its mean value $\big[\ln(D_r/D_c)\big]_{ave} = 11.6$. Therefore, an approximately linear relationship between T_c and ΔH_{coh} is established. The proportionality constant between T_c and ΔH_{coh} can be estimated from the data in Fig. 7.1; it is about $\sim$ 100 K/eV. We then obtain $r \sim 0.1$, or $Q_r \sim -0.1\Delta H_{coh}$, from Eq. (7.3).

Table 7.1 Numerical estimation of $\ln(D_r/D_c)$.

System	MoW	AlSb	AuCu	CrSi	NiPt	NiAu
$D_o(\mathrm{cm}^2/\mathrm{s})$ [a]	4×10^{-2} [b]	9×10^{-2} [c]	2.36×10^{-6} [d]	10^{-2} [e]	2.6×10^{-9} [f]	1.4×10^{-7} [f]
$E_d(\mathrm{eV})$ [g]	40	16.5(Al)	28	21	30	30
$(dE/dX)_n(\mathrm{eV/Å})$ [h]	$500(\mathrm{Xe}^{++})$	$35(\mathrm{Ar}^{+})$	$280(\mathrm{Kr}^{+})$	$350(\mathrm{Xe}^{+})$	$570(\mathrm{Xe}^{+})$	$550(\mathrm{Xe}^{+})$
D_r/D_c [i]	2.8×10^{6}	10^{7}	2.2×10^{4}	1.2×10^{6}	5.7×10^{2}	4.3×10^{3}
$\ln(D_r/D_c)$	15	16	10	14	6.3	8.4

[a] Frequency factor D_o of thermal-diffusion coefficient.

[b] *Diffusion Data*, Vol. 6, edited by F. H. Wöhlbier (Trans Tech S.A., Aadermannsdorf, Switzerland, 1972), p. 206.

[c] A. D. LeClair, J. Nucl. Materials **69/70**, 71 (1978).

[d] *Diffusion Data*, Vol. 12, edited by F. H. Wöhlbier (Trans Tech S.A., Aadermannsdorf, Switzerland, 1976), p. 233.

[e] *Diffusion Data*, Vol. 4, edited by F. H. Wöhlbier (Trans Tech S.A., Aadermannsdorf, Switzerland, 1970), p. 415.

[f] *Diffusion Data*, Vol. 35, edited by F. H. Wöhlbier (Trans Tech S.A., Aadermannsdorf, Switzerland, 1984), p. 165.

[g] Average displacement energy $E_d = (E_A + E_B)/2$ for each $A - B$ system. E_A and E_B are obtained from H. H. Anderson, Appl. Phys. **18**, 131 (1979).

[h] Energy deposited per unit path length nuclear collision, estimated from J. P. Biersach and J. F. Ziegler, *Ion Implantation Techniques*, edited by H. Ryssel and H. Glawisching (Springer-Verlag, Berlin, 1982), p. 122.

[i] $\frac{D_r}{D_c} = \frac{5.35}{\lambda^2}\left(\frac{\alpha D_o E_d}{R_{iv}(dE/dX)_n \varphi}\right)^{1/2}$,
where $\lambda^2 \sim 100$ Å^2, $\alpha \sim 0.025$, $\varphi \sim 3 \times 10^{13}$ ion/cm^{2}s $= 3 \times 10^{-3}$ ion/Å^{2}s (see Ref. 20).

According to the existing models of radiation-enhanced diffusion[19,20], the activation energy for radiation-enhanced diffusion Q_{rad} is half of the vacancy migration energy E_v^m (see Eq. (1.4)). Using a known scaling relationship $E_v^m = -0.24\Delta H_{coh}$,[17] we thus obtain the activation energy for the radiation-enhanced diffusion $Q_{rad} = -0.12\Delta H_{coh}$. Comparing Q_{rad} with Q_r, we conclude that our experimental observation and theoretical interpretation are consistent with a picture of radiation-enhanced diffusion due to direct recombination of vacancies and interstitials together with migration of defects to fixed sinks.

A remarkable feature of this correlation is that it includes both metal-metal and metal-silicon systems. For both cases the mixed layer is metallic. Furthermore, the correlation is structure-independent. The mixed layers can be metallic solid solutions (e.g., Pt-Ni), metallic compounds (e.g., Co_2Si), or amorphous metallic alloys (e.g., Cu-Er). Such independence of long-range order is expected because various energies of diffusion are determined mainly by the local atomic environment and corresponding interaction potentials.

7.4 Summary

We have demonstrated a correlation between the cohesive energy of the system and the characteristic temperature range for the onset of radiation-enhanced diffusion. A simple argument based on current models for cascade mixing (or thermal spikes) and radiation-enhanced diffusion provides a basis for understanding this observed correlation. Further investigations of the influence of ion irradiation parameters (energy, dose, dose rate) and the structure of the matrix will be required for a more critical evaluation of the dependence of T_c on ΔH_{coh}.

7.5 References

1. P. Sigmund and Gras-Marti, Nucl. Instrum. Methods **182/183**, 25 (1981).
2. W. L. Johnson, Y.-T. Cheng, M. Van Rossum, and M-A. Nicolet, Nucl. Instrum. Methods B **7/8**, 657 (1985).
3. S. Matteson, J. Roth, and M-A. Nicolet, Radiat. Eff. **42**, 217 (1979).
4. C. Kittel, *Introduction to Solid State Physics* (Wiley, New York, 1976), p. 74.
5. A. R. Miedema, Philips Tech. Rev. **8**, 36 (1976).
6. W. K. Chu, J. W. Mayer, and M-A. Nicolet, *Backscattering Spectrometry* (Academic, New York, 1978).
7. Y.-T. Cheng, M. Van Rossum, M-A. Nicolet, and W. L. Johnson, Appl. Phys. Lett. **45**, 185 (1984).
8. M. Van Rossum, Y.-T. Cheng, M-A. Nicolet, and W. L. Johnson, Appl. Phys. Lett. **46**, 610 (1985).
9. F. So (private communication).
10. S. Matteson, J. Roth, and M-A. Nicolet, Radiat. Eff. **42**, 217 (1979).
11. J. Bottiger, S. K. Nielsen, and P. T. Thorsen, in *Amorphous Metals and Non-Equilibrium Processing*, edited by M. Von Allmen (Les Editions de Physique, Les Ulis Cedex, 1984), p. 111.
12. J. W. Mayer, B. Y. Tsaur, S. S. Lau, and L. S. Hung, Nucl. Instrum. Methods **182/183**, 1 (1981).
13. Z. L. Wang, J. F. M. Westendorp, S. Doorn, and F. W. Saris, in *Metastable Materials Formation by Ion Implantation*, edited by S. T. Picraux and W. J. Choyke (Elsevier, New York, 1982), p. 59.
14. B. Paine, M-A. Nicoclet, and T. Banwell, in *Metastable Materials Formation by Ion Implantation*, edited by S. T. Picraux and W. J. Choyke (Elsevier, New York, 1982), p. 79.

15. H. Hahn, R. S. Averback, T. de la Rubia, and P. R. Okamoto, in *Beam-Solid Interactions and Phase Transformations*, edited by H. Kurz, G. L. Olsen, and J. M. Poate (Materials Research Society, Pittsburgh, PA, 1986), p. 491.
16. L. S. Wielunski, B. M. Paine, B. X. Liu, C.-D. Lien, and M-A. Nicolet, Phys. Status Solidi **A 72**, 399 (1982).
17. M. Doyama, and J. S. Koehler, Acta Metall. **24**, 871 (1976).
18. G. P. Tiwari, in *Materials Science Forum*, Vol. 1, edited by G. E. Murch (Trans Tech, Aedermannsdorf, 1984), p.171.
19. G. J. Dienes and A. C. Damask, J. Appl. Phys. **29**, 1713 (1958).
20. S. M. Myers, Nucl. Instrum. Methods **168**, 265 (1980).

PART II. THE FORMATION OF AMORPHOUS ALLOYS

Chapter 8

A BRIEF HISTORY OF THE FORMATION OF AMORPHOUS MATERIALS

The word "amorphous" was derived from the Greek $\alpha\mu o\rho\phi - o\varsigma$, meaning "shapeless." ***Amorphous substances*** or ***glasses*** are often used to describe certain materials that are, most importantly, solids to those who see them, handle them, and make use of them. However, atoms and molecules in amorphous materials do not form long-range periodic arrays as do those in crystalline materials. X-ray and electron diffraction methods have often been used to differentiate amorphous from crystalline substances. But the two words "amorphous" and "crystalline" were used to distinguish solids of different physical structures long before the invention of x-ray diffraction* or any other probes with atomic scale resolution. In an article published in *Philosophical Transactions* in 1801, Bournon stated, "The matrix...is likewise siliceous; sometimes crystalline; and sometimes in an amorphous mass."[1]

The experience of man with glass, perhaps predating his first attempts with words, began when the use of a shiny, sharp, rock-like substance, now called ***obsidian***, was discovered. Obsidian is a natural glass fused in the bowels of the earth and heaved onto its surface by volcanic actions. Primitive people who were fortunate enough to live near supplies of this natural glass valued it highly; it could be cut, filed, and shaped for making arrowheads, knife blades, jewelry, ceremonial masks, and other decorative pieces, as well as tools. Some man-shaped obsidian is as old

---

* The x-ray diffraction technique for studying the atomic structure of solids was invented in 1912 by von Laue.

as 70,000 years.

Thousands of years passed before man finally discovered a method of making glass. The facts surrounding the discovery of glassmaking were told in a tale written by the historian Pliny in the first century A.D.[2] Around 5000 B.C., Pliny said, a group of Phoenician sailors beached their ship on the shore of a river in Syria. At mealtime they built a fire under a pot of food resting on blocks of soda from the ship's cargo. The meal was finished and, as the fire died down, the blocks of soda sank into the sand. From the center of the bed of coals an elastic rivulet of shiny, greenish-hued material flowed slowly down the sand. Soon it hardened; man had just fabricated glass for the first time. The earliest examples of manmade glass have been found among the remains of the ancient Middle Eastern civilizations of about 5000 years ago. Many years later, the Egyptians and Syrians discovered that by dropping copper, cobalt, and manganese into melts, glasses having blue, green, and purple colors could be made. It was not until 300 B.C. that a Phoenician artisan (name unknown) invented the *blowing iron* technique.[2,3] This revolutionary glassmaking technique has been used ever since. The invention of the blowing iron technique demonstrated man's awareness of the special viscosity-temperature behavior of glasses, though scientific studies of glasses have been undertaken only in the last hundred years.

It was long thought that substances other than silicate, the major component of natural glass obsidian, could not be made to solidify in the glass state but would invariably assume a crystalline form. The first report in which a range of amorphous metallic alloys were claimed to have been made was by Kramer in the 1930s.[4] His method was based on vapor deposition, a technique in which atoms were evaporated from a heated source to a cold substrate. Some time later Brenner *et al.*[5] claimed to have made amorphous metallic alloys by electrodepositing nickel-phosphorus alloys. In the 1950s, using an *in situ* electron diffraction technique, Buckel and Hilsch[6] investigated the structure of a series of amorphous layers obtained by vapor deposition of metals onto cryogenically cooled substrates. The first unequivocal demonstration that a metallic alloy could be quenched from a molten state to a glassy one was made in 1960 by Duwez and his co-workers at Caltech.[7] The principle underlying their method is that of rapid cooling. By doing so, crystallization may be suppressed and a frozen liquid, the amorphous state, can be obtained. The formation of several natural glasses, such as obsidian, involves precisely this sudden cooling of molten materials during volcanic activity, but at a much lower cooling rate.

The cooling rates of the technique developed by Duwez and other variations of this type of liquid-quenching method are on the order of 10^6 K/sec. The effective cooling rate induced by pulsed lasers on a surface region ($\sim$ 100 Å) of material can reach as high as 10^{12} K/sec. It was discovered in the late 1970s that even the amorphous state of silicon could be achieved by pulsed laser-induced ultra-fast cooling, or laser-quenching.[8] An ultrahigh cooling rate has also been argued as being responsible for amorphous alloy formation by energetic heavy ion irradiation. Here, a dense collisional cascade may cause a local melting of, perhaps, several thousand atoms. A cooling rate of 10^{14}K/sec might be achieved, because the surface-to-volume ratio is extremely large for the small "molten" region induced by collisional cascades.[9]

Quenching from the liquid state is not the only method by which glass can be made. Since the late 1970s, electron beam irradiation has also been observed to induce the crystalline to amorphous transformation.[10] Point defects produced by electron irradiation, such as vacancies, are believed responsible for destabilizing the crystalline phase. Both heavy and light particle irradiation can cause chemical disorder in a compound material, and a disordered crystalline phase may attain a higher free energy than a corresponding amorphous phase so that amorphization becomes energetically favorable.[11]

In the last several years, irradiation-induced formation of the amorphous phase has become an intensively pursued scientific research field. Many amorphous phases have been produced by such methods in laboratories all over the world. But, little known to those who use accelerators to produce energetic particles for bombarding solids is the fact that amorphous materials produced by energetic ion irradiation were known to exist as early as in the late 1890s. In an article in the first edition of *Salmonsens store illustrerede Konversationslexikon* published in Danish in 1893, mineralogist Broegger pointed out that certain originally crystalline minerals have assumed the properties of amorphous substances in the course of time.[12] While retaining their original crystalline appearance, they have become lighter in specific gravity, have assumed conchoidal fracture, have become optically isotropic, etc. He listed some of these materials: gadolinite, euxenite, fergusonite, thorite, zircon and others, many containing the rare earth elements and thorium (Th) or uranium (U). Broegger called these *metamict* materials[12] and the term metamict was derived from the Greek *μεταμιγνυμ*, meaning *mix otherwise*, implying the rearrangement of the originally crystalline structure to a new amorphous structure. He further stated that "The reason for the amorphous rearrangement of the molecules might perhaps be sought in the lesser stability which so complicated a crystal molecule as that of these minerals must have in the presence of outside influences."[12,13] The suggestion that the presence of the metamict materials might be caused by radioactive emanations was first made by Hamberg in 1914.[14] X-ray studies on metamict minerals were carried out first by Rinne[15] for gadolinite in 1915 and by Vegard[16] for thorite in 1916. They found that these metamict minerals are either amorphous, or at best have poor crystalline structures. Now, it is accepted that the metamict state results from radiation damage to the crystalline structure from bombardment by alpha particles arising from the decay of U and Th, usually contained by the mineral.[13]

During the past 2 to 3 years, a number of new methods of forming metallic amorphous alloys have been discovered. In 1983, Yeh *et al.*[17] made a rather surprising observation: The dissolution of hydrogen gas in certain crystalline alloys induces amorphization. Schwarz and Johnson[18] found that simple thermal diffusion of two elemental polycrystalline metals can result in the formation and growth of amorphous alloys. The formation and growth of an amorphous metallic alloy in the solid state, or solid state amorphization is ubiquitous. Yermakov *et al.*, Koch *et al.*, Schwarz *et al.*, and Politis *et al.* have separately reported that amorphous alloys are produced when elemental mixtures of metal powers are mechanically alloyed in a high-energy ball mill.[19] Atzmon *et al.* and Schultz *et al.* have succeeded in producing bulk amorphous alloys by mechanical deformation and alloying of layered binary metals.[20] Schwarz has reported that an initially homogeneous intermetallic compound can transform to the glassy state during ball-milling.[21]

While the excitement of discovering novel methods for producing amorphous materials continues, the present author recently came across, quite accidentally, the following article published in May of 1911 in *Engineering.*[22] This was a report on Dr. G. T. Beilby's lecture entitled "The Hard and Soft States of Metals." It was presented as the May lecture of the Institute of Mechanical Engineers.[23] The following is an excerpt of the report.[22] After defining "amorphous" and "vitreous" (a narrowed-down definition of amorphous according to Beilby), the article reads:

> "... Glass, nevertheless, was non-crystalline, yet it was one of the most stable of all bodies. Yet the physical chemistry would say that it was unstable from the physical standpoint, in spite of the fact that it did not commence to devitrify until heated nearly to its melting point. Sugar, again, in vitreous form, was stable at ordinary temperatures if kept dry, and pure silica itself also had a very stable vitreous form. When molten, these bodies were amorphous, and on freezing retained the condition. It was usual to attribute this retention to the viscosity of the fluid near the temperature of its freezing point. The molecules were thus very sluggish, and only capable of rearranging themselves over a very short-range of temperature. The retention of the non-crystalline form on solidification was fostered, if no crystalline nuclei were present to start with. Thus on heating up sugar crystals a point would be reached at which some of the original crystals became completely amorphous fluids, whilst others had still left a small crystalline nucleus. On cooling the sugar again, the clear cells would retain the amorphous form on solidification, whilst those with nuclei would crystallise.
>
> "Water, which in its usual solid form was preeminently crystalline, could also be obtained in the vitreous condition. Dr. Beilby stated that when staying in Switzerland, he had thrown drops of water on to glass plates, when the temperature was -17 deg. Cent. These instantly congealed and to the amorphous state, although this form was unstable at temperatures above -22 deg. Cent.
>
> "In the case of ductile materials the range of temperature over which the molecules could rearrange themselves was very large. With gold, for instance, crystallization might set in at any temperature from 230 deg. Cent. up to the melting-point. This range of some 800 deg. Cent. was so great that no ordinary method of chilling was sufficiently rapid to stop the change from the amorphous to the crystalline form. Hence in such cases the vitreous form could only be produced as the result of mechanical

> flow, but in this way it was possible to obtain all metals in the vitreous state...."

Beilby believed that cold working, including polishing, converted metals into an amorphous state, which caused work hardening of metals. Although this "amorphous metal theory" of work hardening was oversimple as compared to later, more developed theories based on dislocation structures and internal stresses and strains, Beilby's ideas on the formation of the amorphous phase were actually ahead of his time.

As seen in this brief review of history, the study of the formation of amorphous materials is an engaging one. The following two chapters include some contributions of the present author to this exciting field of scientific research.

References

1. J. L. Bournon, Phil. Trans. **91**, 169 (1801).
2. H. Logan, *How Much Do You Know About Glass?* (Dodd, New York, 1951).
3. F. J. T. Maloney, *Glass in the Modern World* (Doubleday, Garden City, 1968).
4. J. Kramer, Annln Phys. **19**, 37 (1934); J. Kramer, Z. Phys. **106**, 675 (1937).
5. A. Brenner, D. E. Couch, and E. K. Williams, J. Res. Natn. Bur. Stand. **44**, 109 (1950).
6. W. Buckel and R. Hilsch, Z. Phys. **138**, 109 (1954).
7. P. Duwez, R. H. Willens, and W. Klement, Jr., J. Appl. Phys. **31**, 1136 (1960).
8. P. L. Liu, R. Yen, N. Bloembergen, and R. T. Hodgson, Appl. Phys. Lett. **34**, 864 (1979); R. Tsu, R. T. Hodgson, T. Y. Tan, and J. E. E. Baglin, Phys. Rev. Lett. **42**, 1256 (1979).
9. W. L. Johnson, Y.-T. Cheng, M. Van Rossum, and M-A. Nicolet, Nucl. Instrum. Methods **7/8**, 657 (1986).
10. G. J. C. Carpenter and E. M. Schulson, J. Nucl. Materials **23**, 180 (1978); G. Thomas, H. Mori, H. Fujita, and R. Sinclair, Scripta Metall. **16**,589 (1982).
11. D. E. Luzzi, H. Mori, H. Fujita, and M. Meshii, Acta Metall. **34**,629 (1986).
12. W. C. Broegger, Salmonsens store illustrerede Konversationslexikon **1**, 742 (1893).
13. A. Pabst, The Amer. Mineral. **37**, 137 (1952); R. S. Mitchell, Mineral. Record **4** 177 (1973), 214 (1973).
14. A. Hamberg, Geol. För. Förh. **36**, 31 (1914).
15. F. Rinne, Ber. Verh. sächs Akad. Wiss. Math.-Phys. Kl. **67**, 303 (1915).
16. L. Vegard, Phil. Mag. **32**, 65 (1916).
17. X. L. Yeh, K. Samwer, and W. L. Johnson, Appl. Phys. Lett. **42**, 242 (1983).
18. R. B. Schwarz and W. L. Johnson, Phys. Rev. Lett. **51**, 415 (1983).

19. A. Y. Yermakov, Y. Yurchikov, and V. A. Barinov, Phys. Met. Metallugr. **52**, 50 (1981); C. C. Koch, O. B. Cavin, C. G. McKamey, and J. O. Scarbrough, Appl. Phys. Lett. **43**, 1017 (1983); R. B. Schwarz, R. R. Petrich, and C. K. Saw, J. Non-Crystal. Sol. **76**, 281 (1985); C. Politis and W. L. Johnson, J. Appl. Phys. **60**, 1147 (1986); C. Politis, Physica **135B**, 286 (1985).
20. M. Atzmon, J. R. Veerhoven, E. R. Gibson, and W. L. Johnson, Appl. Phys. Lett. **45**, 1052 (1984); L. Schultz, in *Proc. 5th Int. Conf. Rap. Quenched Metals*, edited by S. Steeb and H. Warlimont (North Holland, Amsterdam, 1985).
21. R. B. Schwarz (private communications).
22. *Engineering*, May 19, 1911. p. 660.
23. G. T. Beilby, J. Inst. of Metals **6**, 5 (1911).

Chapter 9

AMORPHOUS AND CRYSTALLINE PHASE FORMATION BY ION MIXING OF Ru-Zr AND Ru-Ti

9.1 Introduction

The formation of amorphous phases by ion mixing (IM) has been of considerable interest over the last several years.[1,2] Several attempts have been made to predict the formation of amorphous phases by this technique. Liu and co-workers[3] have formulated a rule, which states that an amorphous binary alloy will be formed by IM of a multilayered sample when the two constituent metals are of different structures. It has also been suggested that IM is likely to produce a crystalline phase at a composition that corresponds to a compound with a simple lattice structure.[4] Recently, Johnson *et al.* have provided some general criteria regarding amorphous and crystalline phase formation by IM of metal-metal systems based on the consideration of thermodynamic free energy diagrams and the restricted growth kinetics of competing phases.[5] In this chapter, we shall examine the existing rules and ideas regarding the formation of amorphous phases by studying the ion mixing of Ru-Zr and Ru-Ti at various compositions and temperatures.

Both systems have relatively simple equilibrium phase diagrams as shown in Figs. 9.1a and 9.1b. Table 9.1 lists some of the relevant structural information. The Goldschmidt atomic radii are 1.34Å for Ru, 1.47Å for Ti, and 1.60Å for Zr.[6,7,8] Both systems have negative heats of mixing.[9] Factors most likely to influence amorphous phase formation, such as the structure of the terminal solutions, complexity of compound phases, equilibrium free energy of the various phases, effect of defects, and

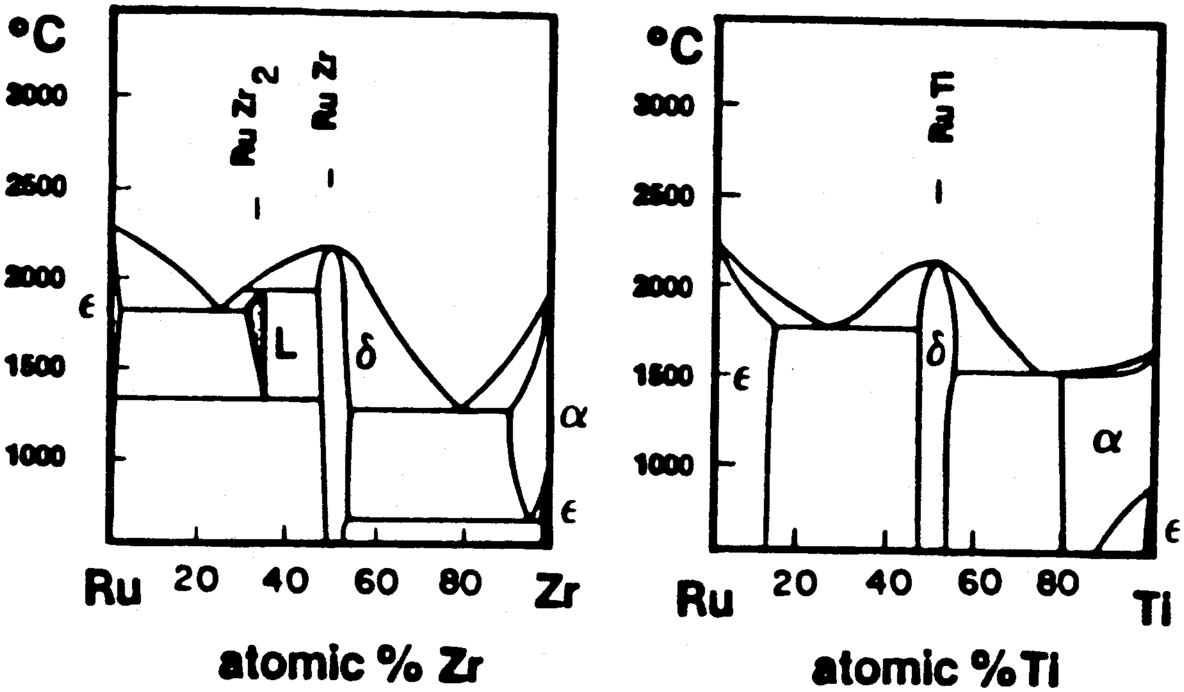

Fig. 9.1 Phase diagrams of Ru-Zr and Ru-Ti. α is a B.C.C. solid solution; ϵ is an H.C.P. solid solution; δ is a Cs-Cl structure intermetallic compound.

Table 9.1 Structural information on Ru-Zr and Ru-Ti systems.

SYSTEM	STRUCTURE	LATTICE PARAMETER (A)		
		a	b	c
Ru	H.C.P.	2.70		4.28
Ti	H.C.P. (T<882.5°C)	2.95		4.68
	B.C.C. (T>882.5°C)	3.3		
Zr	H.C.P. (T<865°C)	3.23		5.13
	B.C.C. (T>865°C)	3.62		
$Ru_{50}Zr_{50}$	B.C.C.*	3.25		
$Ru_{50}Ti_{50}$	Cs-Cl	3.0		

---

* The equilibrium compound $Ru_{50}Zr_{50}$ has a Cs-Cl structure, though the superlattice lines are not observed by x-ray diffraction due to the similar atomic number of Ru and Zr. Thus, we were not able to determine the amount of the atomic site disorder in the $Ru_{50}Zr_{50}$ phase. We shall simply call this phase B.C.C. $Ru_{50}Zr_{50}$.

substrate temperature (T_{sub}) will be considered. Semi-quantitative free energy diagrams are constructed to help in understanding the various observed processes. The thermal stability of amorphous phases against crystallization will also be discussed.

9.2 Ion Mixing of Multilayers of Ru-Ti and Ru-Zr

Multilayered Ru-X (X=Zr,Ti) samples were prepared by electron-gun evaporation onto SiO_2 substrates in an oil-free vacuum system at a pressure in the 10^{-7} Torr range. The average compositions were $Ru_{25}X_{75}$, $Ru_{50}X_{50}$, $Ru_{75}Zr_{25}$, and $Ru_{70}Ti_{30}$ (X=Zr, Ti). The total thickness of each sample was designed to be $R_p + \Delta R_p$ for 300 keV or 600 keV Xe ions (R_p is the projected range and ΔR_p is the range straggling). The thickness ratio between different layers was chosen such that the required homogeneous composition would be obtained after mixing. Layer thicknesses were monitored by a quartz thickness monitor during evaporation.

300 keV Xe^+ or 600 keV Xe^{++} irradiation was performed at substrate temperature T_{sub} ranging from 67 to 570 K. T_{sub} was measured *in situ* by a thermocouple mounted inside the sample holder. The vacuum during the irradiation was maintained below 5×10^{-7} Torr. Implantation doses ranged from 2×10^{15} to $2\times10^{16}/cm^2$ at a flux of about 800 nA/cm^2 for 300 keV Xe^+ and 200 nA/cm^2 for 600 keV Xe^{++} ions. Backscattering spectrometry provided information on the degree of mixing and the compositional ratios (see Fig. 9.2). Structural information was obtained by x-ray diffraction (Read camera, see Fig. 9.3). Isothermal annealings were performed in a vacuum with pressure below 7×10^{-7} Torr for $T > 520$ K and in a flowing He gas gettering furnace for $T < 520$ K. Samples were annealed in sequential temperature steps. The annealing time was 30 minutes at every temperature.

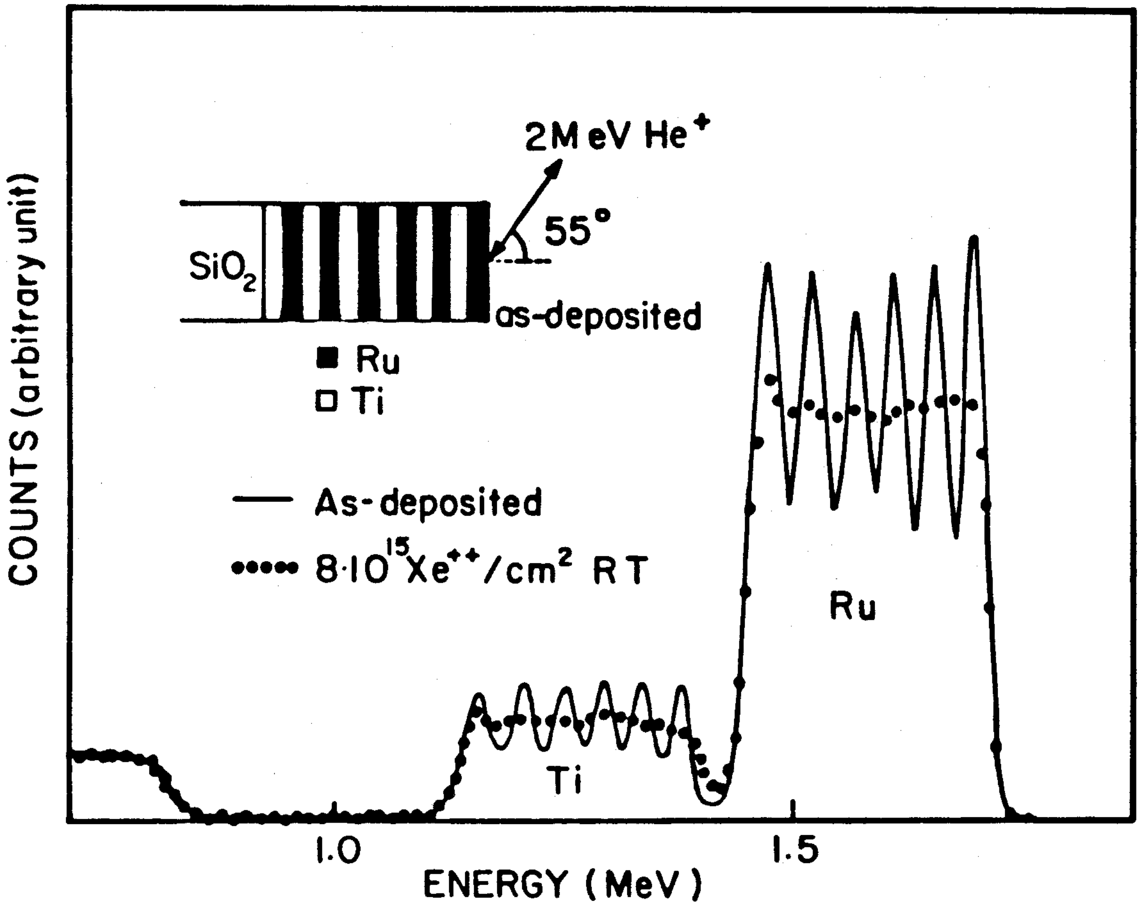

Fig. 9.2 Backscattering spectra of a mutilayer sample at an average composition of $Ru_{50}Ti_{50}$ before and after ion mixing with 600 keV Xe^{++} to a dose of $8 \times 10^{15}/cm^2$ at 300 K.

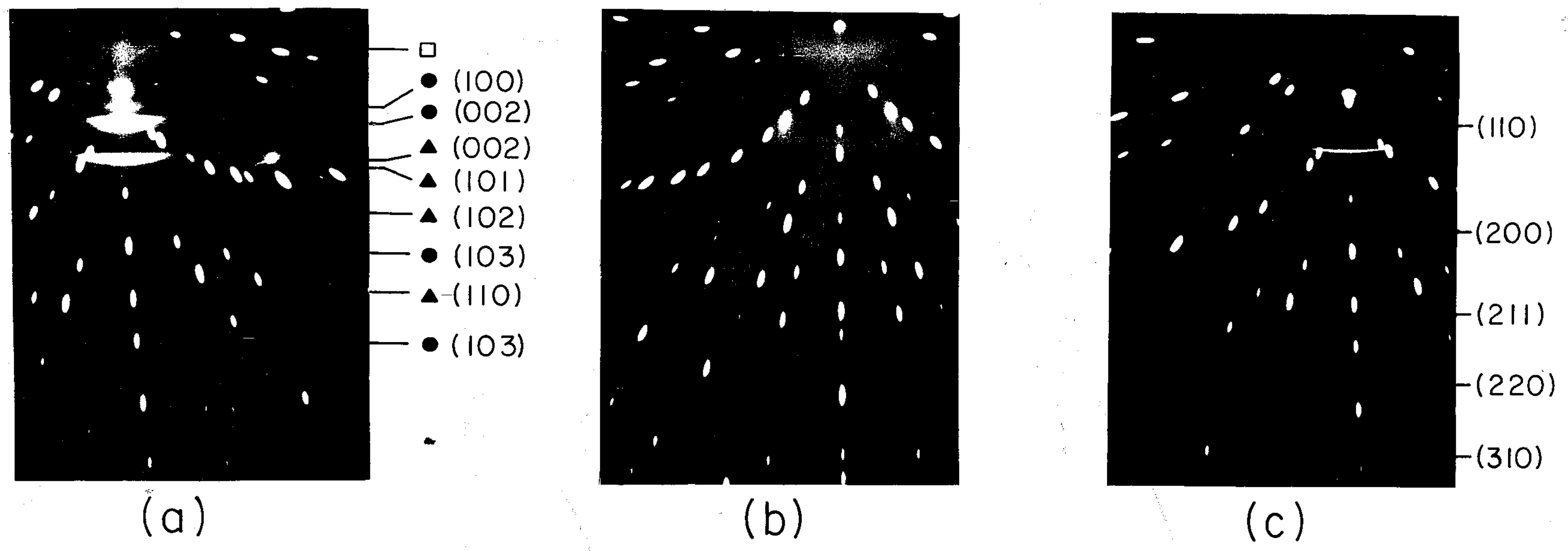

(a) (b) (c)

Fig. 9.3 X-ray diffraction patterns (Read camera) of samples at a composition of $Ru_{50}Zr_{50}$. (a) as-deposited sample (●: Zr and ▲: Ru); (b) amorphous obtained by 300 keV Xe^+ irradiation to a dose of 8×10^{15} /cm^2 at 300 K; (c) B.C.C. phase obtained by 300 keV Xe^+ irradiation to a dose of 8×10^{15}/cm^2 at 433 K. Diffraction spots are from single-crystal Si substrate.

9.3 Experimental Observation of Amorphous and Crystalline Phase Formation by Ion Mixing

Ru-Zr: The general features of IM of Ru-Zr are summarized in Table 9.2a. At 77 K, the 300 keV Xe^+ produced amorphous phases for all three compositions at doses below $5 \times 10^{15}/cm^2$. Further increase of the dose to $2 \times 10^{16}/cm^2$ did not induce other phase changes. The 300 keV Xe^+ IM at a dose 8×10^{15} at different T_{sub} revealed a critical substrate temperature of about $T^c_{sub} = 390$ K for $Ru_{25}Zr_{75}$ and $Ru_{50}Zr_{50}$. Below this temperature, amorphous phases were observed (see Table 9.2a). The lattice-spacing variation reflects the larger Goldschmidt radius of Zr compared with Ru (Tables 9.1 and 9.2a). The crystallization temperatures of amorphous $Ru_{25}Zr_{75}$ and $Ru_{50}Zr_{50}$ produced by 300 keV Xe^+ with a dose of $8 \times 10^{15}/cm^2$ at 77 K are 670 ± 15 K and 510 ± 15 K, respectively.

Ru-Ti: The general features of IM results are summarized in Table 9.2b. To study the effect of T_{sub} on amorphous phase formation, samples with an average composition $Ru_{43}Ti_{57}$ were irradiated at different T_{sub}: 120, 140, 160, 180, and 210 ± 5 K by 300 keV Xe^+ with the dose $8 \times 10^{15}/cm^2$. The critical temperature T^c_{sub} was again observed, and it was found to be around 170 K. Below this temperature, an amorphous phase was formed. Above this temperature and up to 520 K, IM resulted in a B.C.C. phase. The crystallization temperature of amorphous $Ru_{50}Ti_{50}$ produced by 600 keV Xe^{++} with the dose $8 \times 10^{15}/cm^2$ at 77 K was observed to be 450 ± 20 K.

IM at Simple Compound Compositions: The B.C.C. $Ru_{50}Zr_{50}$ phase produced by IM or thermal-annealing was further irradiated by 300 keV Xe^+ to a dose of 8×10^{15} Xe^+/cm^2 at 77 K, and an amorphous phase was obtained. Similarly, the

Table 9.2a 300 keV Xe^+ ion mixing of Ru-Zr with the dose $8 \times 10^{15}/cm^2$ at different substrate temperatures.

T_{sub} (K)	$Ru_{25}Zr_{75}$	$Ru_{50}Zr_{50}$	$Ru_{75}Zr_{25}$
77	AMOR.	AMOR.	AMOR. +H.C.P. Ru
370	AMOR.	AMOR.	AMOR. +H.C.P. Ru
410	H.C.P. Zr (a=3.20, c=5.15) +B.C.C. (a=3.26)	B.C.C (a=3.23)	AMOR. +H.C.P. Ru

Table 9.2b 600 keV Xe^{++} ion mixing of Ru-Ti with the dose $8 \times 10^{15}/cm^2$ at different substrate temperatures.

T_{sub} (K)	$Ru_{25}Ti_{75}$	$Ru_{50}Ti_{50}$	$Ru_{70}Ti_{30}$
77	B.C.C (a=3.17)	AMOR.	H.C.P. (a=2.74, c=4.40)
300	B.C.C. (a=3.16)	B.C.C. (a=3.10)	H.C.P. (a=2.74, c=4.39)

intermetallic compound $Ru_{50}Ti_{50}$ of Cs-Cl structure produced by thermal annealing became amorphous following IM at 77 K.

9.4 Discussion

From the experimental observations, summarized in Table 9.2a and 9.2b, we conclude that T_{sub} is of crucial importance in determining phase formation by IM. By varying T_{sub}, we are able to identify some of the competing phases during IM. For example, at the low T_{sub} of 77 K, the formation of amorphous $Ru_{25}Zr_{75}$ is more favorable than phase separation to H.C.P. Zr plus B.C.C. $Ru_{50}Zr_{50}$ (column 1, Table 9.2a); the formation of an amorphous alloy is more favorable than that of a crystalline compound at $Ru_{50}X_{50}$, where X is either Zr or Ti (column 2, Tables 9.2a and 9.2b). This situation persists up to a critical substrate temperature T^c_{sub}, which is about 170 K for $Ru_{50}Ti_{50}$ and 390 K for $Ru_{50}Zr_{50}$ and $Ru_{25}Zr_{75}$. Above T^c_{sub}, the formation of the competing crystalline phases becomes favorable. At the $Ru_{25}Ti_{75}$ and $Ru_{70}Ti_{30}$ compositions, the formation of single-phase crystalline solutions always wins over the formation of amorphous phases. Since the amorphous phase competes with either one or two crystalline phases, which may or may not depend on the elemental structures, the structural difference rule[3] is of little relevance.

In a previous paper[5] a mechanism was proposed for amorphous phase formation by compositionally induced superheating. The idea is that the local composition is fixed at the end of cascade mixing. Due to the extremely fast effective cooling rate and the absence of radiation-enhanced long-range diffusion, the composition profile does not change further following cascade mixing. If the resulting composition is such that the free energy of an amorphous phase is lower than those of all other crystalline phases, the amorphous phase will form. A similar idea has proven successful in predicting amorphous phase formation by solid-state reaction.[10] To apply the idea of compositionally induced superheating, a knowledge of the free energy of each competing phase is required. Over the past fifteen years, a significant amount of work has been done on studying thermal stability of equilibrium phases in binary alloy systems.[11] Taking data from Refs. 4 and 11, we construct the equilibrium free energy diagrams for Ru-Zr and Ru-Ti systems at specified temperatures in Fig. 9.4. Representing the free energy of the amorphous phase by the supercooled liquid,[12] we see that the free energy of the amorphous phase is higher than that of the solid solutions at all compositions. Thus, the mechanism of amorphous phase formation by compositionally induced superheating does not account for the present observations. However, the equilibrium free energy diagrams of Fig 9.4 do indicate the formation tendency of metastable crystalline phases produced by IM. For example, the diagrams predict that the B.C.C. Ru-Ti solid solution is stable over a large compositional range and the B.C.C. solid solution forms around the $Ru_{50}Zr_{50}$ composition. These predictions are consistent with the experimental observations (see Tables 9.2a and 9.2b). Therefore, we may conclude that the equilibrium free energy diagram is relevant to the ion-beam induced phase transformations. This conclusion is further supported by the fact that thermodynamics can be applied to describe ion-beam induced atomic transport processes as we have demonstrated in previous chapters. But why doesn't the free energy diagram predict amorphous phase formation for Ru-Zr and Ru-Ti? The existence of a critical substrate temperature T^c_{sub} provides a clue; it indicates that a delayed thermally activated process is occurring after cascade mixing. This kind of delayed process is usually associated with migration of defects produced during cascades. Below T^c_{sub}, such defects are trapped in the solid, and one must take into account their contributions to the free energy of crystalline phases.

The influence of point defects has been thought to cause the irradiation-induced crystalline to amorphous phase transformation in Ge and Si.[13] Since the free energy difference between the crystalline and amorphous phases of Ru-Zr and Ru-Ti are about 10 and 20 kJ/mole (see Fig. 9.4), a vacancy concentration of several percent could reverse this energy difference, assuming that the vacancy formation energy is about 1 to 2 eV. Although a vacancy concentration of several percent is much higher than the equilibrium low-temperature value, it has been observed to happen in a field-ion microscopy study of radiation damage.[14] Furthermore, it has been argued that interstitial defects may be crucial in destabilizing crystalline phases.[15] In any case, the presence of quenched-in defects seems to be a necessary condition for the observed amorphous phase formation by IM in Ru-Ti and Ru-Zr systems. Defects should affect the stability of narrow "line" compound phases more drastically, since the narrower the compound homogeneity range, the greater will be the influence of atomic defects and site disorder. Thus, besides the kinetic constraints on forming crystalline phases of narrow compositional range, there may also be an absence of thermodynamic driving forces to form the narrow compounds in a radiation-damaged zone.

It is very desirable to relate the critical temperature for amorphous phase formation observed in this chapter to the critical temperature for the onset of radiation-enhanced diffusion observed in Chapter 7, since both phenomena involve movement of atoms. However, the nucleation of a crystalline phase involves collective motion of atoms locally, whereas radiation-enhanced diffusion is a result of long-range diffusion. As will be discussed in the following chapter, in some cases, the long-range diffusion of atoms can actually induce amorphous alloy formation, even though

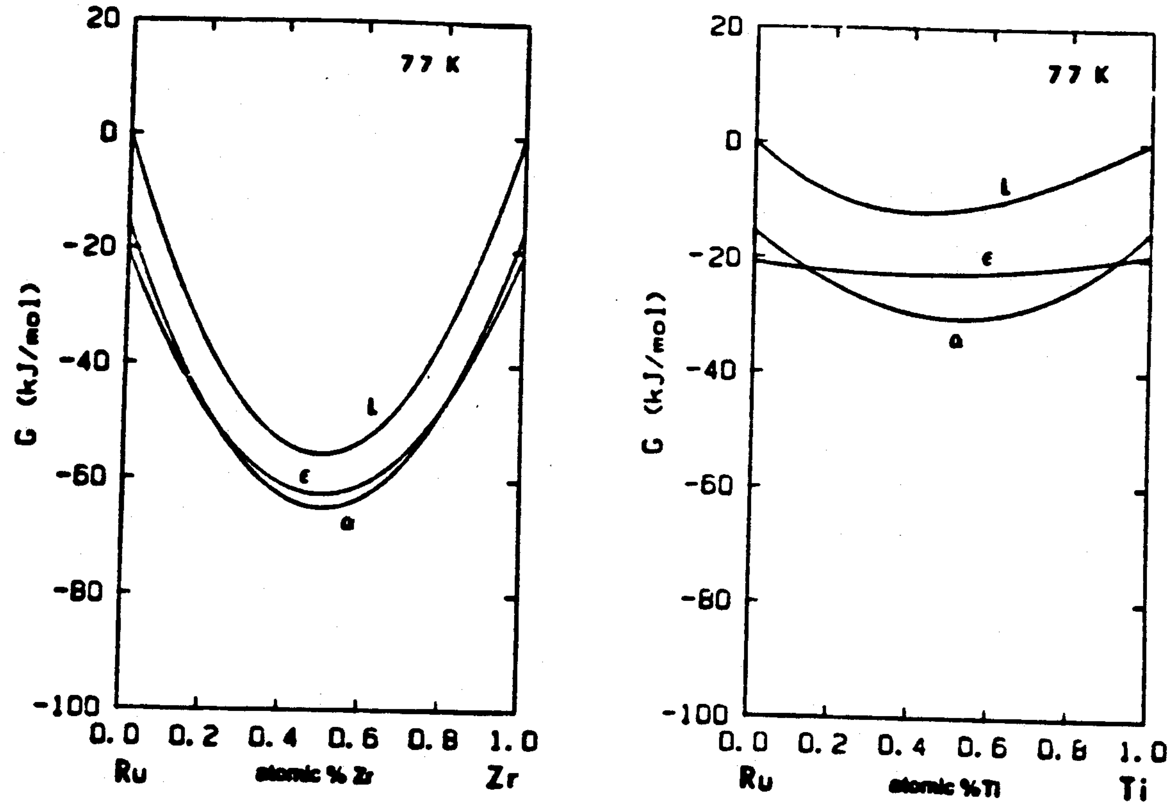

Fig. 9.4 Free-energy diagrams of Ru-Ti and Ru-Zr at 77 K. L represents a liquid (amorphous), α a B.C.C. solid solution, and ϵ an H.C.P. solid solution.

amorphous materials have long been thought to form only in the absence of diffusion. The relationship between the two observed critical temperatures is nontrivial and remains to be clarified.

9.5 Summary

Systematic studies of ion mixing of Ru-Zr and Ru-Ti provide a counter example to the structural difference rule and the compound structural-complexity criteria. The present experiments demonstrate the importance of ambient temperature in amorphous phase formation by ion mixing. It also shows that in order to predict the formation of an amorphous phase, one must understand the free energy of each competing phase, including the influence of defects. Furthermore, an improved understanding of the formation of amorphous phase by ion mixing requires further studies on the kinetic constraints on nucleation and growth of various metastable and stable phases.

9.6 References

1. S. Matteson and M-A. Nicolet, Am. Rev. Mater. Sci. **18**, 339 (1983).
2. J. W. Mayer, B. Y. Tsaur, S. S. Lau, and L. S. Hung, Nucl. Instru. Methods **182/183**, 1 (1981).
3. B. X. Liu, W. L. Johnson, M-A. Nicolet, and S. S. Lau, Appl. Phys. Lett. **42**, 45 (1983).
4. L. S. Hung, M. Nastasi, J. Gyulai, and J. W. Mayer, Appl. Phys. Lett. **42**, 672 (1983).
5. W. L. Johnson, Y.-T. Cheng, M. Van Rossum, and M-A. Nicolet, Nucl. Instru. Methods **B7/8**, 657 (1985).
6. M. Hanson and K. Anderko, *Constitution of Binary Alloys* (McGraw-Hill, New York, 1958).
7. R. J. Shunk, *Constitution of Binary Alloys*, Second Supplement (McGraw-Hill, New York, 1969).
8. J. L. Murray, Bulletin of Alloy Phase Diagrams, **3**, 216 (1982).
9. A. R. Miedema, Philips Tech. Rev. **36**, 217 (1976).
10. R. B. Schwarz and W. L. Johnson, Phys. Rev. Lett. **51**, 415(1983).
11. L. Kaufman and H. Bernstein, *Computer Calculation of Phase Diagrams* (Academic Press, New York, 1970).
12. J. Hafner, Phys. Rev. **B21**, 406 (1980).
13. M. L. Swanson, J. R. Parsons, and C. W. Hoelke, Radiat. Eff. **9**, 249 (1971).
14. D. Prananik and Seidman, J. Appl. Phys. **54**, 6352 (1983).
15. Y. Limoge and A. Barbu, Phys. Rev. **B 30**, 2212 (1984).

Chapter 10

DOMINANT MOVING SPECIES IN THE FORMATION OF AMORPHOUS METALLIC ALLOYS BY SOLID-STATE REACTION

10.1 Introduction

Amorphous metallic alloys have been traditionally produced by rapid quenching from the melt or by sputtering.[1] Recently, however, it has been demonstrated that the amorphous metallic phase can also be produced by solid-state reaction.[2–8] The energetic and kinetic requirements for such a reaction to occur seem to be a compromise between a lowering of the free energy and a mode of growth that favors the amorphous phase over the crystalline ones.[6] In this chapter, we attempt to identify the dominant moving species during such a reaction in the Ni-Zr system. The amorphization of Ni/Zr bilayers by solid-state reaction has previously been reported by several research groups.[4,7]

In their original diffusion experiments, Smigelskas and Kirkendall used Mo wires ($\sim 10\,\mu$m in diameter) as markers between two bulk metals to determine which of the latter had the greater intrinsic diffusion coefficient.[9] In thin-film diffusion studies, with film thicknesses on the order of 1000 Å, inert markers that fulfill an equivalent function must be very thin (< 10 Å). They can be produced by either evaporation or ion implantation. The positional change of the marker as well as the thickness of the growing amorphous layer may be monitored by MeV backscattering spectrometry (BS).[10] Thus, the dominant moving species is determined by studying a small scale Kirkendall effect. Details of this kind of marker experiment may be found in literature relating to silicide formation.[11-16]

10.2 Marker Experiments and the Dominant Moving Species

The sample configuration is shown in Fig. 10.1 (insert). Tungsten (W) and hafnium (Hf) were selected as markers because their heavy atomic mass allows their BS signal to be separated from those of Zr and Ni. Furthermore, W may be considered an "inert" marker, whereas Hf is an "isotope" of Zr (detailed discussion below). About 4 to 10 Å of marker material were deposited. The top Zr layer thickness was optimized to allow a substantial amount of Zr to react while avoiding an overlap of the 2 MeV $^4He^+$ backscattering signals from Zr and from the marker. A thickness of 500 to 1000 Å for the Zr layer was found appropriate. The Ni layer thickness was about 1600 Å. The thin layers of Ni and Zr (~ 25 Å) on either side of the marker were used in some cases in order to position the marker within the amorphous NiZr after an initial short thermal annealing step. This configuration is advantageous for minimizing the possible influence of interfaces on the movement of the marker ("interfacial drag").[15] For some samples, a thin layer of Zr was also deposited between the Ni film and the SiO_2 substrate to improve adhesion.

Samples were prepared by electron-gun evaporation from metallic targets onto oxidized silicon substrates. The vacuum in the evaporation chamber was in the 10^{-8} Torr range prior to deposition and below 2×10^{-7} Torr during evaporation. The layer thicknesses were measured *in situ* by a quartz-crystal thickness monitor, and subsequently by BS. The films were thermally treated at $300 \pm 1°$ C after being removed from the evaporation chamber.* The vacuum in the annealing furnace was

---

* Amorphous NiZr forms in the range of 250 to 350°C by solid-state reaction.[7]

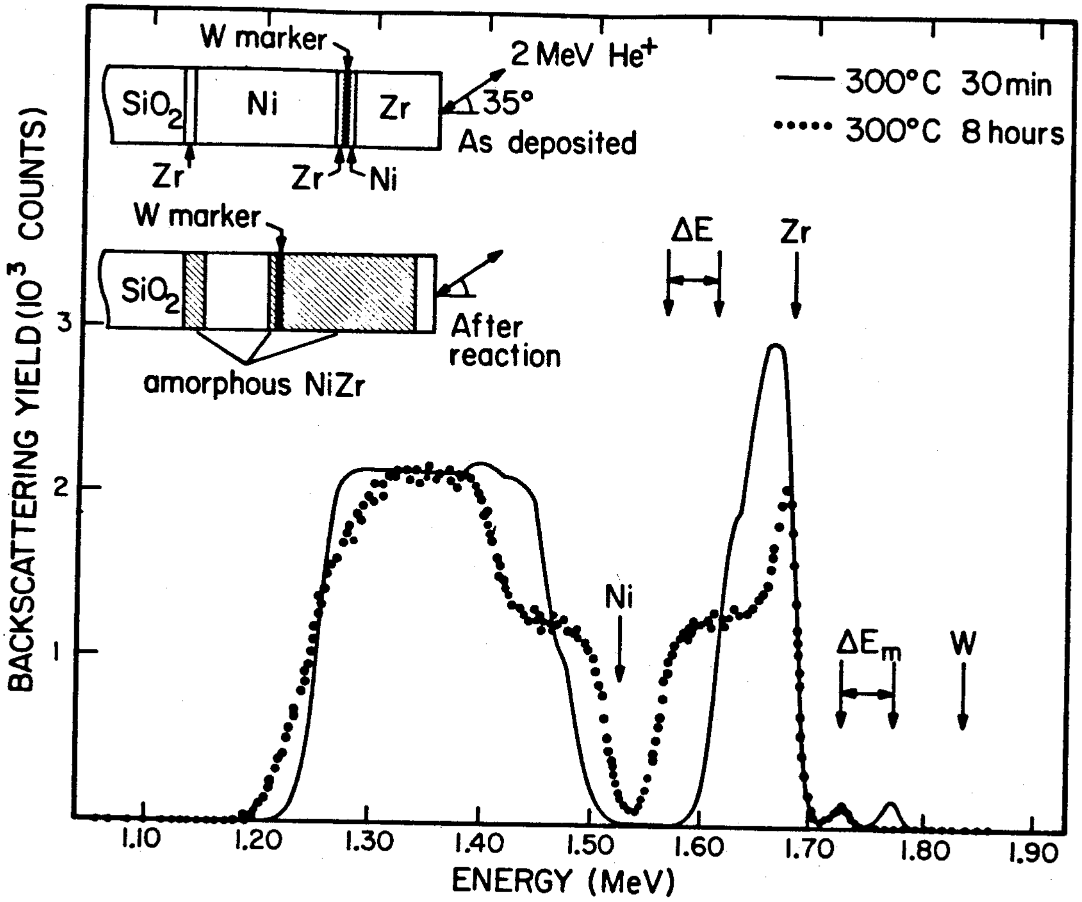

Fig. 10.1 2.0-MeV 35° $^4He^+$ backscattering spectra of a Ni-W(~ 4Å marker)-Zr sample (see insert) annealed for 30 minutes and for 8 hours at 300° C. The displacement of the marker peak position and of the half-height position of the interface between crystalline Ni and amorphous NiZr are shown by ΔE_m and ΔE, respectively. The spectra were taken with 1.66 keV/channel.

kept below 8×10^{-7} Torr. The depth profile of the films was recorded at different stages of thermal annealing by BS using 2 MeV $^4He^+$ ions. Care was taken to keep the intensity of the analyzing beam sufficiently low so as not to cause substantial heating of the samples. Selected samples were checked by x-ray diffraction using Read camera and Philips θ-2θ vertical diffractometer and using Cu K_α radiation. The as-deposited Ni and Zr were both polycrystalline materials with texture and preferred growth normal to close-packed planes; i.e., $< 111 >$ for Ni and $< 200 >$ for Zr. The average diameters of grains, measured from the Ni$< 111 >$ diffraction line width and from the Zr$< 200 >$ diffraction line width, were about 280 Å and 190 Å for Ni and Zr, respectively. Amorphous halos were observed after thermal treatment, as expected.

Backscattering spectra of a Ni-Zr sample with a W ($\sim$ 4 Å) marker annealed for 30 min and for 8 hours at 300°C are shown in Fig. 10.1. The reaction reached completion after the 8 hours of annealing. The residual unreacted Zr near the surface (see Fig. 10.1) is probably caused by oxidation during the thermal annealing.[5] The movement of the W marker signal towards decreasing energy is apparent. The movement of the W marker signal is determined by measuring the energy displacement of the W peak ΔE_m (see Fig. 10.1); the movement of the interface between Ni and amorphous NiZr is determined by measuring the position of the half-height of the low-energy edge of the Zr signal ΔE (see Fig. 10.1). Both ΔE_m and ΔE are measured relative to those of the sample annealed for 30 min at 300°C. During the initial 30 minute annealing, the thin layers ($\sim$ 25 Å) of Ni and Zr on either side of W react; the marker is then positioned within the amorphous NiZr. After this pre-annealing step, the energy displacement of the W marker signal ΔE_m is about equal to the energy displacement of the interface between Ni and amorphous

NiZr ΔE (see Fig. 10.2), within the experimental uncertainty. To first order, the equal amount of downward shift in energy of ΔE_m and ΔE indicates that the energy shifts are due to Ni's diffusing through the W marker and into the amorphous NiZr. Therefore, Ni is the dominant moving species in amorphous NiZr formation by solid-state reaction. We have also established that the outcome of the experiment (i.e., Fig. 10.2) does not change if the amount of W used as the marker is doubled.

After the first 30 min pre-annealing and before the reaction nears completion, the shift of the marker was observed to be roughly proportional to $t^{1/2}$. This $t^{1/2}$ growth behavior is in accordance with an earlier x-ray study of the amorphous phase growth kinetics by solid-state reaction for the Ni-Zr system.[7]

W has also been used as a marker to determine the dominant moving species in Ni silicide formation.[16] The results of these experiments agree with marker experiments using a chemically inert marker such as Xe.[11] In fact, W has a heat of mixing close to zero with both Ni and Zr.[17] Therefore, W is quite likely an inert marker for Ni-Zr diffusion studies.

In a second set of experiments, we selected Hf as the marker instead of W. Many physical and chemical properties of Hf are very similar to those of Zr. Hf and Zr are both from the IV B group of the periodic table of the elements. As pure metals, they have the same HCP crystal structure in the temperature-range considered as well as nearly identical Goldschmidt radii. Moreover, they form a continuous solid solution across the entire compositional range.[18] Like Ni/Zr, Ni/Hf bilayers form amorphous alloys by solid-state reaction at temperatures between 290 and 380°C.[5] Therefore, Hf may be considered as a nearly ideal isoelectronic substitute of Zr in

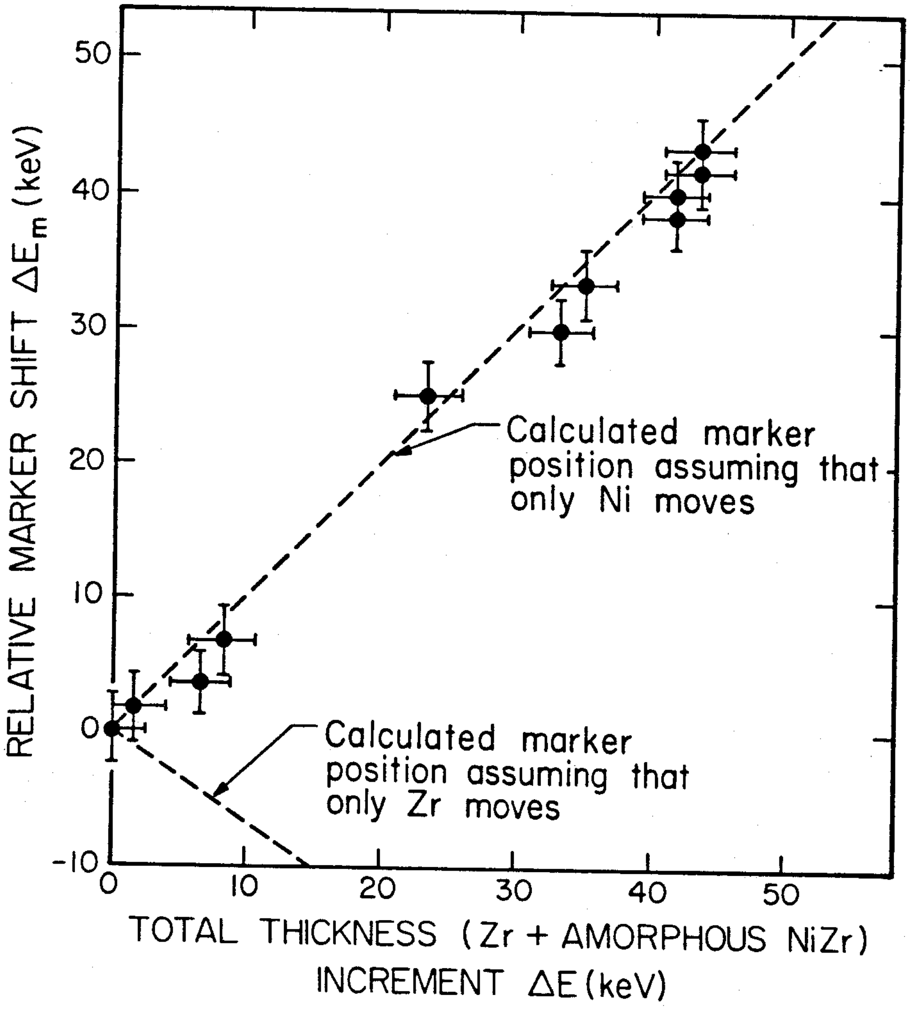

Fig. 10.2. The amount of the energy shift ΔE_m of the backscattering signal of the W marker versus the amount of the energy shift of the Zr signal ΔE from the interface between crystalline Ni and amorphous NiZr. Both quantities are measured with respect to the sample annealed for 30 minutes at 300° C (see Fig. 10.1). The two dashed lines correspond to the energy shift of the W marker signal under the assumption that either Ni or Zr is the the only diffusing species.

the context of this diffusion study. Assuming that this is so, if Ni is the only moving species in amorphous NiZr formation and if there is no movement of Zr with respect to itself, there should also be no movement of Hf with respect to Zr, either. As a result, the position of the Hf marker relative to the growing amorphous layer should be the same as that of the W marker (Figs. 10.1 and 10.2). Furthermore, the BS signal of the Hf marker should remain as sharp as the W signal, except for some small spreading of the marker signal due to the increase of energy straggling as more Ni accumulates above the marker.[10] All of these expected features have been observed experimentally. The shift of the marker was observed to increase linearly with $t^{1/2}$ beyond the first 1 hour of annealing.

10.3 Summary

The "inert" and "isotopic" marker experiments show that Ni is the moving element in the amorphous NiZr formation by solid-state reaction.

Subsequent to the present work[19], the conclusion that Ni is the dominant moving species in the amorphous NiZr formation by solid-state reaction has been confirmed by additional backscattering studies performed by Barbour *et al.*[20] and by Hahn *et al.*[21] The same conclusion has also been confirmed by a transmission electron microscopy experiment of Newcomb and Tu.[22] The present author has also determined that Ni is the dominant moving species in the amorphous NiHf formation by solid-state reaction using the backscattering technique.[23]

10.4 References

1. R. Zallen, *The Physics of Amorphous Solids* (Wiley, New York, 1983), p. 5.
2. R. B. Schwarz and W. L. Johnson, Phys. Rev. Lett. **51**, 415 (1983).
3. R. B. Schwarz, K. L. Wang, W. L. Johnson, and B. M. Clemens, J. Non-Cryst. Solids **61&62**, 129 (1984).
4. B. M. Clemens, W. L. Johnson, and R. B. Schwarz, J. Non-Cryst. Solids **61&62**, 817 (1984).
5. M. Van Rossum, M-A. Nicolet, and W. L. Johnson, Phys. Rev. **B 29**, 5498 (1984).
6. W. L. Johnson, B. P. Dolgin, M. Van Rossum, in *Glass... Current Issues*, edited by A. F. Wright and J. Dupuy (NATO ASI Series, Martinus Nijhoff, Dordrecht, Boston, Lancaster, 1984), p. 172.
7. K. M. Unruh, W. J. Meng, and W. L. Johnson, Mat. Res. Soc. Symp. Proc. Vol. 37, 551 (1985).
8. P. Guilmin, P. Guyot, and G. Marchal, Phys. Lett. **A 109**, 174 (1985).
9. A. D. Smigelskas and E. D. Kirkendall, Trans. Am. Inst. Min. Engrs. **171**, 130 (1947).
10. W. K. Chu, J. W. Mayer, and M-A. Nicolet, *Backscattering Spectrometry* (Academic, New York, 1978).
11. W. K. Chu, H. Krautle, J. W. Mayer, M-A. Nicolet, and K. N. Tu, Appl. Phys. Lett. **25**, 454 (1974).
12. G. J. van Gurp, D. Sigurd, and W. F. van der Weg, Appl. Phys. Lett, **29**, 159 (1976).
13. R. Pretorius, L. L. Ramiller, S. S. Lau, and M-A. Nicolet, Appl. Phys. Lett. **30**, 501 (1977).
14. J. Baglin, F. d'Heurle, and S. Peterson, Appl. Phys. Lett. **33**, 289 (1978).

15. K. N. Tu and J. W. Mayer, in *Thin Films, Interaction and Reactions*, edited by J. M. Poate, K. N. Tu, and J. W. Mayer (Wiley, New York, 1978), Ch 10.
16. K. Affolter, X. A. Zhao, and M-A. Nicolet, J. Appl. Phys. **58**, 3087 (1985).
17. A. R. Miedema, Philips Tech. Rew. **36**, 217 (1976).
18. M. Hanson and K. Anderko, *Constitution of Binary Alloys* (McGraw-Hill, New York, 1958), p. 815.
19. Y.-T. Cheng, W. L. Johnson, and M-A. Nicolet, Appl. Phys. Lett. **47**, 800 (1985).
20. J. C. Barbour, M. Nastasi, and J. W. Mayer, Appl. Phys. Lett. **48**, 517 (1986).
21. H. Hahn, R. S. Averback, and S. J. Rothman, Phys. Rev. **B 33**, 8825 (1986).
22. S. B. Newcomb and K. N. Tu, Appl. Phys. Lett. **48**, 1436 (1986).
23. Y.-T. Cheng, M-A. Nicolet, and W. L. Johnson, Mat. Res. Soc. Symp. Proc. Vol. 54, 175 (1986).

APPENDIX 1

NUMERICAL ANALYSIS OF BACKSCATTERING SPECTRA

The following computer program listing is a FORTRAN program, which converts a backscattering spectrum of counts versus channel to a concentration versus depth profile. This program was originally designed by the author to study ion mixing of bilayers. Lately, T. Workman has improved this program. The program listed below is one of his latest versions. Theoretical background of the equations used in this program can be found in the book, *Backscattering Spectrometry*, by W. K. Chu, J. W. Mayer, and M-A. Nicolet (Academic Press, New York, 1978). This book is referred to as BS in the following discussions.

Program Summary

Necessary Information

1. Three point channel-energy calibration for the spectrum.
2. Atomic number (Z), atomic density (ρ), kinematic factor (K), and stopping cross-section factors for the top and bottom layers of the bilayer.
3. The region of channels containing the bottom layer signal, including a subregion in which the concentration is assumed to be one.
4. Incident beam energy (E_0) and scattering geometry, including backscattering angle (θ_D) and sample tilt angle (θ_1).
5. Background level in counts per channel.

Procedure

1. Subtract background counts from each channel.

2. Convert from counts versus channel to counts versus energy using a least-squares fit to the channel-energy calibration.
3. Given the incident beam energy E_0 and the detected energy E_1, calculate the energy E of the same beam before scattering from the bottom layer element B, using Eq.(3.21) of BS:
$$E = \frac{E_1 + \alpha E_0}{K_B + \alpha}, \tag{A1.1}$$
where $\alpha = (1/\cos\theta_D)(\epsilon^B(K_B E_0)/\epsilon^B(E_0))$ and K_B is the kinematic factor of the bottom layer and $\epsilon^B(K_B E_0)$ and $\epsilon^B(E_0)$ are the stopping cross-sections for the bottom layer material, at energies $K_B E_0$ and E_0, respectively. Notice that α does not change by more than 5% for metals such as Ni, Pt, Au, and Ag when the beam energy is on the order of a few MeV.
4. Correct the counts H for increasing cross sections as the energy decreases. The cross section is proportional to $(1/E)^2$. Thus, a correction of H can be made by dividing this factor.
5. Convert counts to concentration. Using the "interface energy approximation," i.e., assuming a constant incident beam energy E_{int} across the interfacial region of A-B bilayer, then after step 4, we can express Eq. (3.76) of BS as:
$$C_i = \frac{H_i}{X_{norm}}(C_i\epsilon^B(E_{int}) + [1 - C_i]\epsilon^A(E_{int}))\cos\theta_1 \tag{A1.2}$$
where C_i and H_i are the corresponding concentration and counts of B, and X_{norm} is approximately a constant and can be determined from the concentration $C_i = 1$ region. Then the concentration C can be calculated from counts H.
6. Convert energy to depth, using Eq. (3.53) of BS with the assumption that the atomic density of the mixed region is a linear combination of the densities of the pure elements.

```
C      *********************************************************
C      *                                                       *
C      *                          RBS                          *
C      *   CONVERSION OF BACKSCATTERING SPECTRA OF BILAYERS    *
C      *          TO CONCENTRATION VS DEPTH PROFILES           *
C      *                                                       *
C      *  Required file structures to use this program:        *
C      *   1. File of spectrum in RT11 format - You must know  *
C      *      the Digital Offset used for the spectrum.        *
C      *   2. Material info (St Cr-Sec, At. Density, K factor) *
C      *      must be stored in INFO.DAT on DY0:               *
C      *   3. Calibration info (Energy per Channel and Offset) *
C      *      can be stored in a datafile and recalled here -  *
C      *      Use the program ENTCAL to write the datafile.    *
C      *                                                       *
C      *  Necessary Spectrum Info to use this program:         *
C      *   1. Chan. Numbers of the peak boundaries             *
C      *   2. Calibration info (Cali. Datafile optional)       *
C      *   3. Background level (in counts per channel)         *
C      *   4. Chan. Number of the front edge of the back peak  *
C      *      (to determine the interface energy)              *
C      *   5. Chan.  #'s  of regions of the front and/or back  *
C      *      peak(s) where the Atomic Concentration is 1.0    *
C      *                                                       *
C      *  Program Output:                                      *
C      *   Output is two datafiles (one for each layer) that   *
C      *   contain X,Y values of depth and concentration.  A   *
C      *   printout is also available on request.              *
C      *                                                       *
C      *********************************************************
      PROGRAM RBS
      DIMENSION X1(400),X2(400),H1(400),H2(400),SCS(85,6),D(85),
     1 AD(50),B(50),DELX1(400),DELX2(400),CC(5),ECH(5),CNTS(520),
     1 XKF(85)
      P=3.1415926/180.
      BYTE TITLE(12),CALI(12)
      CALI(12)= .FALSE.
C
C     **********  GET MATERIAL AND CALIBRATION INFO  **********
C
      OPEN(UNIT=1,TYPE='OLD',NAME='DY0:INFO.DAT')
      DO 5 I=1,85
        READ(1,10) IZ,SCS(I,1),SCS(I,2),SCS(I,3),SCS(I,4),
     1  SCS(I,5),SCS(I,6),D(I),XKF(I)
5     CONTINUE
10    FORMAT(1X,I3,1X,F9.4,1X,F9.4,1X,F9.4,1X,F9.4,
     1      1X,F9.4,1X,F9.5,1X,F6.3,1X,F7.5)
      CLOSE(UNIT=1)
15    TYPE 20
20    FORMAT('0Enter Calibration Filename [<Return> for none]: ',$)
      ACCEPT 750, CALI
      IF (CALI(1) .EQ. '') GO TO 50
      OPEN(UNIT=1,TYPE='OLD',NAME=CALI,ERR=25)
      GO TO 30
25    TYPE*,'Error in opening datafile, Please try again.'
      GO TO 15
30    CONTINUE
      DO 40 I=1,50
        READ(1,45) J,AD(I),B(I)
40    CONTINUE
45    FORMAT(1X,I3,1X,F10.5,1X,F10.5)
      CLOSE(UNIT=1)
C
C     ********************  GET DATAFILE  ********************
C
50    TYPE 55
```

```
55          FORMAT('0Enter the spectrum filename: ',$)
            ACCEPT 750,TITLE
            OPEN(UNIT=1,TYPE='OLD',NAME=TITLE,ERR=60)
            GO TO 65
60          TYPE*,'Error in opening datafile, Please try again.'
            GO TO 50
65          CONTINUE
            TYPE 70
70          FORMAT(' Enter the digital offset:    ',$)
            ACCEPT*,IDIG
            I=1
75          CONTINUE
              READ(1,95,END=90,ERR=80) CH,CNTS(I)
              I=I+1
            GO TO 75
80          CONTINUE
            TYPE 85,I
85          FORMAT(' Error in datafile at line ',I5,/)
            GO TO 75
90          CONTINUE
            CLOSE(UNIT=1)
95          FORMAT(1X,F5.1,2X,F6.1)
C
C           **************  DEFINE BOUNDARIES OF PEAKS **************
C
            TYPE 100
100         FORMAT(' Enter the boundaries of the back peak:  ',$)
            ACCEPT*,IB1,IB2
            DO 110 I=IB1,IB2
              H1(I-IB1+1)=CNTS(I-IDIG+1)
              X1(I-IB1+1)=FLOAT(I)
110         CONTINUE
            NPTS1=IB2-IB1+1
            TYPE 120
120         FORMAT(' Enter the boundaries of the front peak: ',$)
            ACCEPT *,IT1,IT2
            DO 130 I=IT1,IT2
              H2(I-IT1+1)=CNTS(I-IDIG+1)
              X2(I-IT1+1)=FLOAT(I)
130         CONTINUE
            NPTS2=IT2-IT1+1
C
C           ******  CALIBRATION FOR CHAN TO ENERGY CONVERTION  ******
C
            TYPE 150
150         FORMAT(' Enter Calibration # (0 for new calibration): ',$)
            ACCEPT*,ICAL
            IF (ICAL .GT. 100 .OR. ICAL .LT. 1) ICAL=0
            IF (ICAL .GT. 0) GO TO 200
            TYPE 160
160         FORMAT(' Calibration information: How many calibration
        1 points? ',$)
            ACCEPT*,NC
            TYPE*,'  Input Channel, Energy (in MeV)'
            DO 165 I=1,NC
              ACCEPT*,CC(I),ECH(I)
165         CONTINUE
C                            LEAST SQUARE FIT TO CALIBRATION
            CC2=0.
            EC=0.
            CC1=0.
            CEC=0.
            DO 170 I=1,NC
              CC2=CC2+CC(I)**2
              EC=EC+ECH(I)
              CC1=CC1+CC(I)
```

```
          CEC=CEC+CC(I)*ECH(I)
170     CONTINUE
        DEL=NC*CC2-CC1**2
        AD(ICAL)=(CC2*EC-CC1*CEC)/DEL
        B(ICAL)=(NC*CEC-CC1*EC)/DEL
C
C       ***************  GET MATERIAL PROPERTIES  ***************
C
200     CONTINUE
        TYPE 205
205     FORMAT('0Enter top layer Atomic Number:    ',$)
        ACCEPT*,IT
        IF (IT .LT. 1 .OR. IT .GT. 85) GO TO 200
240     TYPE 245
245     FORMAT(' Enter bottom layer Atomic Number: ',$)
        ACCEPT*,IB
        IF (IB .LT. 1 .OR. IB .GT. 85) GO TO 240
C
C       **************  BEAM AND TARGET PARAMETERS **************
C
300     CONTINUE
        TYPE 310
310     FORMAT('0Enter the Beam Energy (in MeV):               ',$)
        ACCEPT*,E0
        TYPE 320
320     FORMAT(' Enter the Backscattering Angle (in degrees): ',$)
        ACCEPT*,BTETA
        COS1=COS(P*BTETA)
        COSD=COS(P*10.)
        COS2=COS1*COSD
        BETA=1/COSD
C
C       ***************  SUBTRACT THE BACKGROUND  ***************
C
        TYPE 350
350     FORMAT(' Enter the Background Level:                  ',$)
        ACCEPT*,BGD
        DO 360 I=1,NPTS1
          HTEMP=H1(I)-BGD
          IF(HTEMP.LT.0.) HTEMP=0.
360     H1(I)=HTEMP
        DO 370 I=1,NPTS2
          HTEMP=H2(I)-BGD
          IF(HTEMP.LT.0.) HTEMP=0.
370     H2(I)=HTEMP
C
C       ******  DEFINE INTERFACE ENERGY FOR BOTTOM LAYER  *******
C
        TYPE 400
400     FORMAT(' Enter the Channel of the front edge of the back
    1 peak: ',$)
        ACCEPT*,CH
        EINT1=AD(ICAL)+B(ICAL)*CH
C                       POLYNOMIAL FIT TO THE STOPPING CROSS SECTION
        EPSI(A,B,C,D,F,G,EE)=A+B*EE+C*EE**2+D*EE**3+F*EE**4+G*EE**5
        EPSIA=EPSI(SCS(IB,1),SCS(IB,2),SCS(IB,3),SCS(IB,4),
    1        SCS(IB,5),SCS(IB,6),XKF(IB)*E0)
        EPSIB=EPSI(SCS(IB,1),SCS(IB,2),SCS(IB,3),SCS(IB,4),
    1        SCS(IB,5),SCS(IB,6),E0)
        ALPH2=(EPSIA/EPSIB)*BETA
        EINT=(EINT1+ALPH2*E0)/(XKF(IB)+ALPH2)
C
C       ******  CONVERT FROM CHANNEL SPACE TO ENERGY SPACE  *****
C
        DO 450 I=1,NPTS1
          X1(I)=AD(ICAL)+B(ICAL)*X1(I)
```

```
450     CONTINUE
        DO 460 I=1,NPTS2
          X2(I)=AD(ICAL)+B(ICAL)*X2(I)
460     CONTINUE
C
C       *****  CORRECT COUNTS FOR INCREASING CROSS SECTION  *****
C
C                         CALCULATE STOPPING CROSS SECTIONS FOR B
        EPSI1=EPSI(SCS(IB,1),SCS(IB,2),SCS(IB,3),SCS(IB,4),
     1       SCS(IB,5),SCS(IB,6),XKF(IB)*EINT)
        EPSI2=EPSI(SCS(IB,1),SCS(IB,2),SCS(IB,3),SCS(IB,4),
     1       SCS(IB,5),SCS(IB,6),EINT)
        EPSI3=EPSI(SCS(IT,1),SCS(IT,2),SCS(IT,3),SCS(IT,4),
     1       SCS(IT,5),SCS(IT,6),XKF(IB)*EINT)
        EPSI4=EPSI(SCS(IT,1),SCS(IT,2),SCS(IT,3),SCS(IT,4),
     1       SCS(IT,5),SCS(IT,6),EINT)
        ALPH=(EPSI1/EPSI2)*BETA
C                         REF:PAGE 65 BACKSCATTERING SPEC
C                         CORRECT LAYER B FOR INCREASING CROSS SECTION
        DO 500 I=1,NPTS1
          EE1=(X1(I)+ALPH*EINT)/(XKF(IB)+ALPH)
          H1(I)=H1(I)*((EE1/EINT)**2)
          EPSIT1=EPSI(SCS(IB,1),SCS(IB,2),SCS(IB,3),SCS(IB,4),
     1          SCS(IB,5),SCS(IB,6),XKF(IB)*EE1)
          EPSIT2=EPSI(SCS(IB,1),SCS(IB,2),SCS(IB,3),SCS(IB,4),
     1          SCS(IB,5),SCS(IB,6),EE1)
          ALPH=(EPSIT1/EPSIT2)*BETA
500     CONTINUE
        F1=XKF(IB)*(EPSI2-EPSI4)/COS1+(EPSI1-EPSI3)/COS2
        F2=XKF(IB)*EPSI4/COS1+EPSI3/COS2
C                         CALCULATE STOPPING CROSS SECTIONS FOR A
        EPSI5=EPSI(SCS(IT,1),SCS(IT,2),SCS(IT,3),SCS(IT,4),
     1       SCS(IT,5),SCS(IT,6),XKF(IT)*E0)
        EPSI6=EPSI(SCS(IT,1),SCS(IT,2),SCS(IT,3),SCS(IT,4),
     1       SCS(IT,5),SCS(IT,6),E0)
        EPSI7=EPSI(SCS(IB,1),SCS(IB,2),SCS(IB,3),SCS(IB,4),
     1       SCS(IB,5),SCS(IB,6),XKF(IT)*E0)
        EPSI8=EPSI(SCS(IB,1),SCS(IB,2),SCS(IB,3),SCS(IB,4),
     1       SCS(IB,5),SCS(IB,6),E0)
        ALPH=(EPSI5/EPSI6)*BETA
C                         REF:PAGE 65 BACKSCATTERING SPEC
C                         CORRECT LAYER A FOR INCREASING CROSS SECTION
        DO 510 I=1,NPTS2
          EE1=(X2(I)+ALPH*E0)/(XKF(IT)+ALPH)
          H2(I)=H2(I)*((EE1/E0)**2)
          EPSIT1=EPSI(SCS(IT,1),SCS(IT,2),SCS(IT,3),SCS(IT,4),
     1          SCS(IT,5),SCS(IT,6),XKF(IT)*EE1)
          EPSIT2=EPSI(SCS(IT,1),SCS(IT,2),SCS(IT,3),SCS(IT,4),
     1          SCS(IT,5),SCS(IT,6),EE1)
          ALPH=(EPSIT1/EPSIT2)*BETA
510     CONTINUE
        F3=XKF(IT)*(EPSI6-EPSI8)/COS1+(EPSI5-EPSI7)/COS2
        F4=XKF(IT)*EPSI8/COS1+EPSI7/COS2
C
C       ***********  DEFINE CONCENTRATION=1 REGIONS  ***********
C
        TYPE*,
        TYPE*,'Select to define the concentration = 1 region for -'
        TYPE 545
545     FORMAT(' [1] top layer   [2] bottom layer   [3] both layers: ',$)
        ACCEPT*,IMODE
        TYPE*,
        IF (IMODE .EQ. 2) GO TO 560
        TYPE 550
550     FORMAT(' Enter Conc=1 Region for top layer:    ',$)
        ACCEPT*,IL,IR
```

```
        HA=0.
        DO 555 I=IL,IR
          HA=HA+H2(I-IT1+1)
555     CONTINUE
        XNORM2=HA*(F3+F4)/FLOAT(IR-IL+1)
C                       REF:EQU(3.76) BACKSCATTERING SPEC
560     IF (IMODE .EQ. 1) GO TO 575
        TYPE 565
565     FORMAT(' Enter Conc=1 Region for bottom layer: ',$)
        ACCEPT*,IL,IR
        HA=0
        DO 570,I=IL,IR
          HA=HA+H1(I-IB1+1)
570     CONTINUE
        XNORM1=HA*(F1+F2)/FLOAT(IR-IL+1)
575     CONTINUE
        ZT=FLOAT(IT)
        ZB=FLOAT(IB)
        IF (IMODE .EQ. 1) XNORM1=XNORM2*(((ZB/ZT)*(E0/EINT))**2)
        IF (IMODE .EQ. 2) XNORM2=XNORM1*(((ZT/ZB)*(EINT/E0))**2)
        TYPE*,' XNORM1 = ',XNORM1
        TYPE*,' XNORM2 = ',XNORM2
C
C       *********  FINAL CONVERSION TO CONC. VS DEPTH  **********
C
C                       HEIGHT TO CONCENTRATION CONVERSION LAYER B
        DO 655 I=1,NPTS1
          IF(H1(I).EQ.0.0) GO TO 650
          H1(I)=F2/(XNORM1/H1(I)-F1)
          GO TO 655
650       H1(I)=0.0
655     CONTINUE
C                       ENERGY TO DISTANCE CONVERSION LAYER B
        DIS=0.
        DO 660 I=1,NPTS1
          DELX1(I)=DIS
          DLX=(X1(I+1)-X1(I))/(F1*H1(I)+F2)/(H1(I)*D(IB)+
    >     (1.-H1(I))*D(IT))*1000.
          DIS=DIS+DLX
660     CONTINUE
C                       HEIGHT TO CONCENTRATION CONVERSION LAYER A
        DO 670 I=1,NPTS2
          IF(H2(I) .EQ. 0.) GO TO 665
          H2(I)=F4/(XNORM2/H2(I)-F3)
          GO TO 670
665       H2(I)=0.0
670     CONTINUE
C                       ENERGY TO DISTANCE CONVERSION LAYER A
        DIS=0.
        DO 675 I=1,NPTS2
          DELX2(I)=DIS
          DLX=(X2(I+1)-X2(I))/(F3*H2(I)+F4)/(H2(I)*D(IT)+
    >    (1.-H2(I))*D(IB))*1000.
          DIS=DIS+DLX
675     CONTINUE
C       ************************************
C       **   PRINT AND SAVE OUTPUT FILES   **
C       ************************************
        TYPE 700, TITLE
700     FORMAT('0Input filename = ',12A1)
        TYPE 705
705     FORMAT(' Enter filename for Front-Peak Output File: ',$)
        ACCEPT 750,TITLE
        OPEN(UNIT=1,TYPE='NEW',NAME=TITLE)
        DO 715 I=1,NPTS2
          WRITE(1,710) DELX2(I),H2(I)
```

```
710       FORMAT(1X,F10.6,2X,F10.6)
715     CONTINUE
        CLOSE(UNIT=1)
        TYPE 720
720     FORMAT(' Enter filename for Back-Peak Output File:  ',$)
        ACCEPT 750,TITLE
        OPEN(UNIT=1,TYPE='NEW',NAME=TITLE)
        DO 725 I=1,NPTS1
          WRITE(1,710) DELX1(I),H1(I)
725     CONTINUE
        CLOSE(UNIT=1)
        TYPE 730
730     FORMAT(' Want a hard copy? 1=Yes, 0=No: ',$)
        ACCEPT*,I
        IF(I.LE.0) GO TO 800
        WRITE(6,10) TITLE
        PRINT*,
        PRINT*,'       BOTTOM LAYER MATERIAL'
        PRINT*,
        PRINT*,'  CHAN  ','  COUNTS  ','  DEPTH  ','  CONCEN  '
        DO 735 I=1,NPTS1
          PRINT*,X1(I),H1(I),DELX1(I),H1(I)
735     CONTINUE
        DO 740 I=1,4
          PRINT*,
740     CONTINUE
        PRINT*,'       TOP LAYER MATERIAL'
        PRINT*,
        PRINT*,'  CHAN  ','  COUNTS  ','  DEPTH  ','  CONCEN  '
        DO 745 I=1,NPTS2
          PRINT*,X2(I),H2(I),DELX2(I),H2(I)
745     CONTINUE
750     FORMAT(12A1)
C
C       ***************  RECYCLE FOR NEW SPECTRUM  ***************
C
800     CONTINUE
        TYPE 810
810     FORMAT('0 Analyze another spectrum? 1=Yes, 0=No: ',$)
        ACCEPT*,I
        IF (I .GT. 0) GO TO 50
        END
```

APPENDIX 2

THE FRACTAL NATURE OF COLLISIONAL CASCADES

In Chapter 6, the fractal nature of collisional cascades was shown by using a model of "idealized" collisional cascade. It was shown that a fractal dimension is associated with cascades governed by the inverse-power potential. It was then possible to provide a quantitative criteria for the condition of a spike based on the concept of "space-filling" fractals. It was concluded that the fractal dimensionality increases as an actual collisional cascade evolves due to the change of the effective interaction potentials and that the characteristic kinetic energy per particle in a spike is on the order of a few eV. In this appendix, we point out that the notion of a fractal dimensionality $D = 1/(2m)$ (Eq. (6.8)) for collisional cascades determined by inverse-power potential $V(r) \propto r^{-1/m}$ with $0 < m \leq 1/2$ is inherent in the Winterbon-Sigmund-Sanders (WSS) theory of collisional cascades.[1] This new observation further supports the conclusions drawn in Chapter 6.

From the WSS theory (which is formulated in 3-dimensional physical space), the characteristic length scale (e.g., ion range) R of a collisional cascade scales with the incident ion energy E_0 and is given by[1]

$$R = \frac{E_0^{2m}}{NC_m}, \tag{A2.1}$$

where C_m is a constant for fixed m and N is the atomic density. The number of displaced atoms N_c is obtained from a Kinchin-Pease type of argument,[2,3]

$$N_c = \xi \frac{E_0}{E_d}, \tag{A2.2}$$

where ξ is a constant of values between 0.40 to 0.65, which depends on the details of different models, and E_d is the threshold displacement energy. From Eqs. ($A2.1$)

and ($A2.2$), we obtain

$$N_c \propto R^{\frac{1}{2m}}. \tag{A2.3}$$

From the equivalent definitions of fractal dimension,[4,5] we recognize that Eq. ($A2.3$) is just another manifestation of the fractal nature of the underlying collisional cascade with the same fractal dimension $D = 1/(2m)$ obtained from the idealized cascade approach (Eq. (6.8)).

The "space-filling" condition, or the condition for a spike, can also be examined. We consider the ratio η between the displaced atoms to the lattice atoms

$$\eta \propto \lim_{R\to\infty} R^{D-3} = \begin{cases} \infty, & \text{if } D \geq 3; \\ 0, & \text{if } D < 3. \end{cases} \tag{A2.4}$$

Thus, $D = 3$ is shown to be the critical dimension of a "space-filling" collisional cascade in 3-dimensional space.

We have demonstrated the fractal nature of collisional cascade by studying the idealized collisional cascade (Chapter 6) and the WSS theory. Either approach enables us to establish a fractal dimension for cascades governed by the inverse-power potential. The idealized collisional cascade approach shows, at the level of binary collision events, the scaling property of the mean free path (Eq. (6.7)) from which the fractal dimensionality results. The approach based on the WSS theory has the advantage of not relying on assumptions such as the hard-sphere collision approximation, though the underlying feature which gives rise to the fractal dimension is obscured. The fact that both approaches give the same result suggests that the two methods are complementary to each other and the conclusions drawn from either approach are of general nature.

References

1. K. B. Winterbon, P. Sigmund, and J. B. Sanders, Mat. Fys. Medd. Dan. Vid. Selsk. **37**, 1 (1970).
2. G. H. Kinchin and R. S. Pease, Rep. Prog. Phys. **18**, 1 (1955).
3. P. Sigmund, Appl. Phys. Lett. **14**, 114 (1969).
4. B. B. Mandelbrot, *The Fractal Geometry of Nature* (W. H. Freeman and Company, New York, 1983).
5. S. H. Liu, Solid State Physics, Vol. 39, 207 (1986).